

Effect of capillarity on the breakup of liquid jets, interfacial wave and motion of droplets in immiscible liquids

Zur Erlangung des akademischen Grades
Doktor der Ingenieurwissenschaften
der Fakultät für Maschinenbau
Karlsruher Institut für Technologie (KIT)

genehmigte

Dissertation

von

M.Sc. Fei Wang

Tag der mündlichen Prüfung: April 27, 2017

Hauptreferent: Prof. Dr. rer. nat. Britta Nestler

Korreferent 1: Prof. Dr.-Ing. Martin Heilmaier

Korreferent 2: Prof. Dr.-Ing. Christian Karcher



This document is licensed under a Creative Commons Attribution-Non Commercial 4.0 International License (CC BY-NC 4.0): <https://creativecommons.org/licenses/by-nc/4.0/deed.en>

Abstract

A spontaneous breakup of a liquid jet into a chain of droplets is a common phenomenon observed in daily life. Typical examples are the formation of droplets from a falling jet under water-faucet and in the process of raining. This phenomenon has also been used for technical applications, such as fabrications of nanoparticles from nanowires and inkjet printing. The morphological stability of a liquid jet, which describes whether the jet remains a uniform radius cylinder or transforms into a sequence of droplets, has been addressed by the classical Plateau-Rayleigh criterion according to the condition that which state has the lower surface energy/area.

In the first part of the present thesis, I aim to derive a generalized morphological stability criterion, regarding the limitations of the Plateau-Rayleigh theory, such as non-conservation of mass and non-consistency with experimental observations. The current stability criterion is achieved by applying the non-increasing surface energy principle as well as by analyzing the distribution of the mean curvature, which corresponds to the capillary force that causes the stabilization or spheroidization of jets. In contrast to the classic Plateau-Rayleigh theory as well as other existing criteria, the present criterion has following benefits: (i) It can be applied for perturbations of all possible amplitudes $a \in [0, R_0]$, where R_0 is the radius of the jet. (ii) It obeys the non-increasing free energy principle. (iii) It is in good agreement with simulation results based on the-state-of-the-art phase-field models. (iv) It agrees with existing criteria in their corresponding validity range.

As shown in the Plateau-Rayleigh criterion, perturbations at a fluid-fluid interface may dissipate or grow with time. With the aim of understanding the dissipation behavior and the interaction of the resulted droplets, the corresponding numerical simulations and analyses are carried out in the second part of the current thesis. In the former case, it has been found that there is a critical capillary force above which perturbations dissipate in a under-damped manner, which gives rise to a capillary wave. In the latter case, the studies reveal that the migration speed of droplets is significantly enhanced with the consideration of capillary flow. As a further extension, the effect of capillary flow on the size distribution of droplets in the spinodal decomposition process where multi-droplets occur is discussed in comparison with the conventional LSW theory.

Zusammenfassung

Ein spontanes Aufbrechen eines Flüssigkeitsstrahls in eine Kette von Tröpfchen ist ein allgemeines Phänomen, das im täglichen Leben beobachtet wird. Typische Beispiele sind die Bildung von Tröpfchen aus einem fallenden Strahl unter einem Wasserhahn und beim Regnen. Dieses Phänomen wurde auch für technische Anwendungen, wie die Herstellung von Nanopartikeln aus Nanodrähten und für das Tintenstrahldrucken, eingesetzt. Die morphologische Stabilität eines Flüssigkeitsstrahls, die beschreibt, ob der Strahl ein einheitlicher Radiuszylinder bleibt oder in eine Sequenz von Tropfen umgewandelt wird, wurde durch das klassische Plateau-Rayleigh-Kriterium unter der Bedingung angesprochen, dass der Zustand die niedrigere Oberflächenenergie oder die kleinere Fläche aufweist.

Im ersten Teil der vorliegenden Arbeit möchte ich ein verallgemeinertes morphologisches Stabilitätskriterium mit Bezug auf die Einschränkungen der Plateau-Rayleigh-Theorie, wie die Nicht-Konservierung von Masse und die Nicht-Konsistenz mit experimentellen Beobachtungen, ableiten. Das aktuelle Stabilitätskriterium wird durch Anwendung des nicht steigenden Flächenenergieprinzips sowie durch Analyse der Verteilung der mittleren Krümmung erreicht, die der Kapillarkraft entspricht, die die Stabilisierung oder Sphäroidisierung von Strahlen bewirkt. Im Gegensatz zu der klassischen Plateau-Rayleigh-Theorie sowie anderen bestehenden Kriterien hat das vorliegende Kriterium folgende Vorteile: (i) Es kann für Störungen aller möglichen Amplituden $a \in [0, R_0]$ angewendet werden, wobei R_0 der Radius des Strahls ist. (ii) Es gehorcht dem nicht wachsenden Prinzip der freien Energie. (iii) Es stimmt gut mit Simulationsergebnissen auf Basis modernster Phasenfeldmodelle überein. (iv) Es stimmt mit den bestehenden Kriterien in ihrem entsprechenden Gültigkeitsbereich überein.

Wie in dem Plateau-Rayleigh-Kriterium gezeigt, können Störungen an einer Fluid-Fluid-Grenzfläche mit der Zeit dissipieren oder wachsen. Mit dem Ziel, das Dissipationsverhalten und die Wechselwirkung der resultierenden Tröpfchen zu verstehen, werden die entsprechenden numerischen Simulationen und Analysen im zweiten Teil der vorliegenden Arbeit durchgeführt. Im ersten Fall wurde festgestellt, dass es eine kritische Kapillarkraft gibt, oberhalb derer Störungen in einer unterdämpften Weise dissipieren, was zu einer Kapillarwelle führt. Im zweiten Fall zeigen die Studien, dass die Wanderungsgeschwindigkeit der Tröpfchen bei der Berücksichtigung der Kapillarströmung signifikant erhöht wird. Als zusätzliche Erweiterung wird der Einfluss der Kapillarströmung auf die Größenverteilung von Tröpfchen im spinodalen Zersetzungsprozess, bei dem Mehrfachtröpfchen auftreten, im Vergleich zur herkömmlichen LSW-Theorie diskutiert.

Preface

We often observe the breakup of a liquid jet into a chain of droplets. Daily examples are the formation of droplets from a falling jet under water-faucet and in the process of raining. It was believed that the breakup is due to the gravitational force before the work of Rayleigh (Nobel prize winner in physics, 1904). Based on a former work of Plateau, Rayleigh found that this process is actually driven by the capillary force rather than gravity. Their results are known as the Plateau-Rayleigh criterion, which has been collected in many textbooks of materials science and regularly serves as a useful reference in industrial applications.

The present thesis revisits the work of Rayleigh and discusses the effect of capillary force on the related topics. The background of Rayleigh's work as well as the relevant applications are reviewed in chapter 2. In chapter 3, I present two state-of-the-art numerical modeling techniques, which are employed to numerically corroborate the renowned Plateau-Rayleigh criterion. The results of the corroboration are shown in chapter 4. Inspired by the flaws of the Plateau-Rayleigh criterion, such as, non-conservation of mass and contradiction with experimental observations, I aim to derive an alternative morphological stability criterion, which is expected to be a generalization of Rayleigh's work. In chapters 5 and 6, I present the simulation results for the formation of capillary wave and the motion of droplets, which both are driven by the capillary force. The numerical models as well as the corresponding simulation results haven been published in the following peer-reviewed articles

- **Article 1:** F. Wang*, A. Choudhury, M. Selzer, R. Mukherjee, B. Nestler, *Phys. Rev. E* **86**, 066318 (2012).
- **Article 2:** F. Wang*, R. Mukherjee, M. Selzer, and B. Nestler, *Phys. Fluids* **26**, 124102 (2014).
- **Article 3:** F. Wang*, M. Selzer, and B. Nestler, *Physica D* **307**, 82 (2015).
- **Article 4:** F. Wang* and B. Nestler, *Scripta Mater.* **113**, 167 (2016).
- **Article 5:** F. Wang*, M. Ben Said, M. Selzer, and B. Nestler, *J. Mater. Sci.* **51**, 1820 (2016).

In the final chapter, I conclude the thesis and discuss other possible applications of the phase-field models, which have been published in the following article

*Corresponding author

- **Article 6:** F. Wang* and B. Nestler, *Acta Mater.* **95**, 65 (2015).

I have obtained the permission from all the co-authors and publishers to partially or entirely use the published results (including texts, equations, tables and figures) in current thesis. The corresponding contributions of the co-authors to the articles have been stated by the relevant footnotes in each chapter. Apart from these stated contributions, other scientific achievements are mine, unless otherwise declared. Figures 2.1, 2.6, 2.7, 2.8 are taken from literatures and the permission to use these four figures has been granted by the corresponding publishers. The license for usage of copyrighted figures is limited to the present thesis.

No Objection Certificate

As a coauthor, I hereby claim no objection if the first author (Mr. Fei Wang) uses the attached article(s) entirely or in-parts, for his doctoral thesis submitted to the Faculty of Mechanical Engineering, Karlsruhe Institute of Technology. Further I do not object to the description of my contributions as laid in Fei Wang's thesis.

This specific no objection certificate is being issued on the specific request by the first author.

-Signed by all the coauthors

October 10, 2016

Declaration of Originality

Respondents' contribution to the articles

Article 1: As the first author, the respondent (Fei Wang abbreviated as F.W.) did the analysis, performed all the phase-field simulations, and wrote the entire article with inputs from A. Choudhury (A.C.), M. Selzer (M.S.), R. Mukherjee (R.M.), and B. Nestler (B.N.).

Article 2: As the first author, the respondent performed all the phase-field simulations and wrote the entire article with inputs from R. Mukherjee (R.M.), M. Selzer (M.S.), and B. Nestler (B.N.).

Article 3: As the first author, the respondent did the analysis in the bipolar coordinate, performed all the phase-field simulations, and wrote the entire article with inputs from M. Selzer (M.S.) and B. Nestler (B.N.).

Article 4: As the first author, the respondent did the analysis for the mean curvature, performed all the phase-field simulations, and wrote the entire article with inputs from B. Nestler (B.N.).

Article 5: As the first author, the respondent performed all the phase-field simulations and wrote the entire article with inputs from M. Ben Said (M.B.S.), M. Selzer (M.S.), and B. Nestler (B.N.).

Article 6: As the first author, the respondent performed all the phase-field simulations and wrote the entire article with inputs from B. Nestler (B.N.).

The scientific inputs from the co-authors are indicated by footnotes in the corresponding chapter. Apart from these declared scientific inputs, other contributions in the present dissertation are mine, unless otherwise stated.

Acknowledgements

I would like to express my deepest gratitude towards my supervisor Prof. Britta Nestler. Without her constantly support and periodic supervision, I could imagine how hard I would be able to complete the present thesis. I wish to acknowledge Profs. M. Heilmaier and C. Karcher to be the referees of the present thesis. Many thanks to Prof. M. Heilmaier (IAM, KIT), Dr. K. von Klinski (IAM, KIT), and Dr. R. Mukherjee for their creative collaborations. I am indebted to Dr. J. Brillo (DLR, Köln) and Dr. H. Kobatake (DLR, Köln) for their valuable discussions on the Al-Au system. I will not forget the email communications with Prof. W. C. Carter (MIT, Massachusetts) whom is greatly acknowledged.

I especially acknowledge the fundings provided by the following agencies: (i) Center for Materials Science and Engineering (CCMSE), Baden-Württemberg, (ii) Helmholtz program EMR, (iii) European Fond for Regional Development (EFRE), and (iv) Mittelbauprogramm provided by the state of Baden-Württemberg.

I have to thank Dr. Abhik Choudhury and Dr. Michael Selzer for helping me to get started in the group and for all their guidance and support. I am grateful to Dr. M. Berghoff for his generous help of using latex and to Mr. O. Tschukin for his active and valuable discussions.

Finally, I thank my wife and my parents who continually support me.

Contents

1	Introduction: Synopsis	1
1.1	Morphological stability of liquid jets	2
1.2	Under-damped capillary wave	3
1.3	Effect of capillary flow on motion, coarsening and coalescence of droplets .	3
2	Literature review	5
2.1	Effect of surface tension	5
2.2	The Plateau-Rayleigh theory	7
2.2.1	Surface energy minimization concept	9
2.2.1.1	The work of Rayleigh in 1878	9
2.2.1.2	The work of Rayleigh in 1879	9
2.2.1.3	The work of Carter and Glaeser in 1987	10
2.2.2	The wavelength corresponding to the maximum speed of breakup .	12
2.2.3	Stability analysis	13
2.2.3.1	Linear stability analysis: the work of Nichols and Mullins	13
2.2.3.2	Nonlinear stability analysis	15
2.2.4	Applications of the Plateau-Rayleigh theory	15
2.2.5	Capillary bridge	17
2.3	Motion of droplets due to capillarity	17
3	Methods: The Cahn-Hilliard-Navier-Stokes and the Allen-Cahn models	21
3.1	The free energy functional for non-uniform systems	23
3.2	A mathematical definition of the chemical potential and the Cahn-Hilliard model	24
3.2.1	Definition of the chemical potential in a tangent functional space .	24
3.2.2	The Cahn-Hilliard model	25
3.3	Capillary tensor and the Cahn-Hilliard-Navier-Stokes model	26
3.3.1	The stress balance at a fluid-fluid interface and the capillary tensor	26
3.3.2	The Cahn-Hilliard-Navier-Stokes equation	27
3.3.3	Non-dimensionalization of the Cahn-Hilliard-Navier-Stokes equation	28
3.3.4	Discretization and staggered mesh	29
3.4	Simulation system	33
3.5	The multi-phase Allen-Cahn model	35
3.5.1	The Allen-Cahn model	35
3.5.2	Volume preservation technique	36

3.6	In accordance with the thermodynamical law	36
4	Corroboration of the Plateau-Rayleigh criterion	39
4.1	Simulation setup	39
4.2	Validation of the classic Plateau-Rayleigh criterion for tiny perturbations	40
4.3	Significant deviations of the simulation results from the Plateau-Rayleigh criterion	42
4.4	The problems for the stability criterion in literature	43
5	A generalized morphological stability criterion for liquid jets	45
5.1	A general surface energy minimization concept	45
5.2	Physical mechanisms for spheroidization	47
5.3	Derivation for the generalized morphological stability criterion	48
5.4	Comparison of the present stability criterion with existing criteria and with the simulation results	50
5.5	An application to the detachment of nanowires	53
6	Underdamped capillary wave	57
6.1	Simulation setup	57
6.2	Results and discussion	59
7	Effect of capillary flow on motion, coarsening and coalescence of droplets	67
7.1	Analytical study	69
7.1.1	Bipolar coordinate	69
7.1.2	Solution of the Laplace equation in the bipolar coordinate	71
7.1.3	Stream function	72
7.1.4	Interpretation of the analysis	81
7.2	Numerical investigation on the motion of the droplets driven by capillary flow	84
7.2.1	Motion	84
7.2.2	Transition from motion to coalescence	86
7.2.3	Coalescence	87
7.2.4	Coarsening	89
7.2.5	Phase separation affected by capillary flow in Fe-50 at% Sn alloy .	90
7.2.6	Phase separation influenced by capillary flow in Fe-40 at% Sn alloy	92
8	Conclusion and outlook	97
8.1	Conclusion and remarks	97
8.2	Future directions	98
8.2.1	Irregular perturbation	98
8.2.2	Satellite mini droplets	99
8.2.3	Other applications of the numerical models	100
A	Capillary tensor	103
B	Surface Laplacian evaluation	105

C	Coefficients	107
D	Velocity and stream function	109
E	Expansions	111
F	Matrices	113
G	Recursion	115
H	List of Symbols	117
I	List of Abbreviations	119
	Bibliography	121

Chapter 1

Introduction: Synopsis

When a flat fluid-fluid interface/surface is perturbed, the mean curvature of the interface/surface is inhomogeneous and the capillary flow is subsequently induced. In the present thesis, I investigate the effect of capillary flow at a fluid-fluid interface/surface using the phase-field models, namely, the Cahn-Hilliard-Navier-Stokes and the Allen-Cahn models. Both methods are in accordance with the fundamental law of thermodynamics that the free energy of the system is non-increasing with time. In particular, the research contents are classified into three categories:

- Morphological stability of liquid jets due to capillarity
- Capillary wave at a fluid-fluid interface
- Effect of capillary flow on the motion of droplets

The first topic is motivated by the experimental observation that a continuous fluid jet may break up into a chain of droplets after perturbations. A daily example is shown in



Figure 1.1: Illustration for a falling jet under water faucet. This figure is from the website: www.flickr.com.

Fig. 1.1, where the falling jet under water-faucet sometimes is a continuous cylinder and occasionally breaks up into a chain of droplets. The question arising is that when the liquid jet is stable and when it is unstable. This topic was investigated by Lord Rayleigh (Nobel prize winner in physics, 1904) based on a former work of Joseph Plateau. The derived criterion is known as the Plateau-Rayleigh criterion, which has been collected in many textbooks. However, I shall point out the limitations of this criterion and propose an alternative one, which seems to be more general.

In the second topic, I focus on the dissipation behavior of the perturbation at a fluid-fluid interface. I shall figure out when the dissipation of perturbations is over-damped and when it is under-damped. In the lateral case, the perturbation oscillates sinusoidally and the amplitude exponentially decreases with time, which results in a capillary wave. The present study on this topic is to advance our understandings on the formation of capillary wave. In the third topic, I investigate the effect of capillary flow on the motion of the droplets. In the following sections, I present a brief overview of the work.

1.1 Morphological stability of liquid jets

This portion of the thesis deals with the morphological stability of a liquid jet which is perturbed by a cosine/sinusoidal function in the radial direction. As shown by Rayleigh [1], the final state of the perturbed jet is a chain of droplets if the wavelength of the perturbation is greater than the circumference of the jet. Otherwise, the end-state is a uniform-radius cylinder. In chapter 4, I corroborate Rayleigh's criterion using the Cahn-Hilliard-Navier-Stokes (CHNS) model. However, Rayleigh's work is based on the consideration of tiny perturbations. For perturbations of larger amplitudes, I observe that the simulation results of the CHNS model significantly deviate from the classical Plateau-Rayleigh criterion.

Motivated by the above observation, I aim to derive a generalized criterion in chapter 5. In the first part of chapter 5, I propose a novel surface energy minimization concept. In contrast to the assumption that the initial cosine/sinusoidal perturbation remains harmonic all the time in literature, the temporal perturbation is expressed in a more general form. The objective is to obtain the critical setup which obeys the non-increasing free energy principle. In the second part of chapter 5, the corresponding dynamic equations is examined to derive the critical setup for the breakup of liquid jets. The present criterion is compared with the work of Rayleigh [1, 2], Nichols and Mullins [3], Carter and Glaeser [4], and Nayfeh [5]. Which criterion obeys the non-increasing free energy principle and which not are further discussed.

1.2 Under-damped capillary wave

This part discusses the dissipation behavior of perturbations at a fluid-fluid interface and is presented in chapter 6. The diffusion potential correlates to the mean curvature of the interface and after the perturbation, a surface diffusion/convection is induced due to the inhomogeneity of the mean curvature. In two dimensions, the mean curvature at the convex position is greater than the one at the concave place and the surface flux of the surface diffusion/convection is from the convex to the concave positions, resulting in the dissipation of the perturbation.

The objective of this chapter is to investigate when the perturbation dissipates in an under-damped manner and when it does not. In the former case, the amplitude of the perturbation exponentially decreases but oscillates sinusoidally with time, giving rise to a capillary wave. The critical condition for the occurrence of the capillary wave is obtained by using the Fourier analysis.

1.3 Effect of capillary flow on motion, coarsening and coalescence of droplets

This part of the thesis is presented in chapter 7. In the first part, I analytically explore the motion of two droplets in a bipolar coordinate. The Laplace equation for the concentration and the stream function for the convection are solved analytically with appropriate boundary conditions. The Laplace equation is coupled with the stream function through the balance between the capillary force and the viscosity force.

In the second part of this chapter, I study the motion of two droplets using the CHNS model. Depending on the distance between the droplets and the size ratio, I investigate the effect of capillary flow on the motion, coarsening and coalescence of the droplets. Moreover, the effect of capillary flow on the motion speed of droplets is explored. As a further extension, I study the role of capillary flow in the spinodal decomposition process where multi-droplets occur.

Chapter 2

Literature review

Surface tension is an important property of materials. At a static fluid-fluid interface, the effect of surface tension is quantified by the renowned Young-Laplace equation, which states that the pressure difference across the interface equals the surface tension multiplying the curvature. When the mean curvature or surface tension is inhomogeneous, a fluid flow is induced and the treated problem is in the context of fluid dynamics rather than fluid statics. The induced flow is named as capillary flow and gives rise to distinct morphological patterns in natural science.

One typical example for the pattern formation due to capillary flow is that a liquid jet can simultaneously break up into a chain of droplets. This topic was addressed by the classical Plateau-Rayleigh criterion, which will be overviewed in the current chapter. Achievements from other scientists as well as the corresponding technical applications of this topic are also briefly reviewed.

2.1 Effect of surface tension

Surface tension is due to the asymmetry of molecules forces, such as cohesion and adhesion. It plays a significant role in materials science, physics, chemistry, biology, etc. At constant temperature T and pressure P , surface tension equals Gibbs free energy G per surface area \mathcal{A} and it is defined as

$$\sigma = \left(\frac{\partial G}{\partial \mathcal{A}} \right)_{T,P}.$$

Fig. 2.1 shows an example for a natural observation of the effect of surface tension [6]. Water-walking insects usually climb water menisci and seek land to lay their eggs or avoid predators. This climbing ability is a necessary adaptation for their ancestors as they evolved from terrestrials to live on the water surface. During the climbing process, the

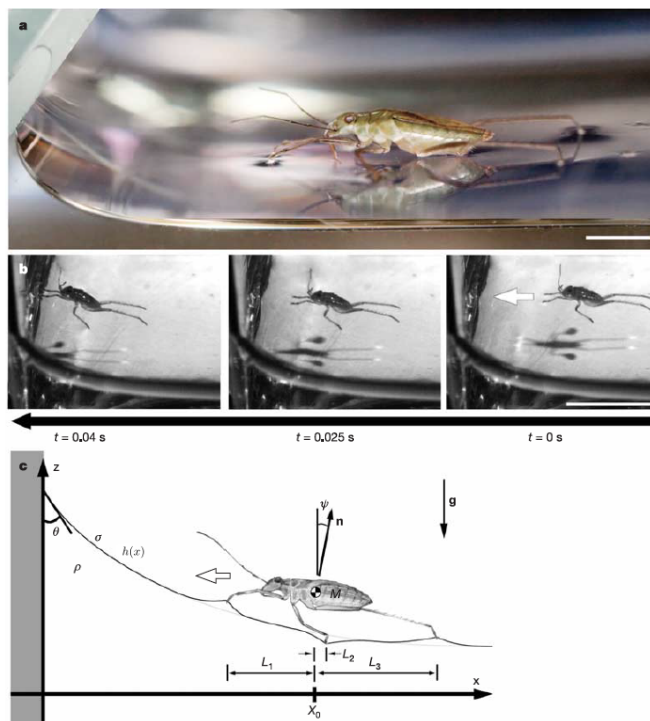


Figure 2.1: Meniscus climbing by the water treader *Mesovelia* [6]: (a) *Mesovelia* approaches the menisci from right to left. (b) Climbing process captured by a high speed video. (c) Schematic illustration of the meniscus-climbing of *Mesovelia*. Reprinted with permission from Nature Publishing Group © 2005.

weight of the water-walking insect is balanced with the surface tension force

$$\rho g h = \sigma \kappa,$$

where ρ is the density of the insect, g is the gravitational acceleration, $h(x)$ and κ are the analytical expression and mean curvature of the menisci, respectively.

At static, the pressure difference across the fluid interface equals the capillary force: $\Delta p = \sigma \kappa$. When the curvature κ is non-uniform, a pressure gradient occurs and drives the motion of the fluid. For solid phases, the diffusion potential changes with the mean curvature and the evolution of the system is caused by the surface diffusion. Either the convection or the surface diffusion tries to minimize the surface energy, or to reduce the surface area for isotropic surface tension.

A typical example for the surface area minimization is coalescence. When two droplets are in contact, the non-uniform curvature around the neck causes the motion of the droplets to join each other, as shown in Fig. 2.2 (a). The convergence state is a droplet which has less surface area than before coalescence. The role of coalescence is crucial in the formation of rain. As droplets are carried by the updrafts and downdrafts in a cloud, they collide and coalesce to form larger droplets. Another example is that, when we mix the salad, the suspended oil-drops coalesce in the vinegar.

Contrary to coalescence, a perturbed fluid-column can simultaneously break up into separate droplets, as illustrated in Fig. 2.2 (b). This process is also to minimize the surface area, as in the case of coalescence, and is observed in many physical systems with applications to such fields as circuit technology, annealing, and sintering. The question arising is when the jet decomposes into a chain of droplets and when it is morphologically stable.

The well-known classic pinch-off condition of liquid jets is according to Plateau [7] and Rayleigh [1]. The analyzed setup consists of a R_0 -radius jet, which is axisymmetrically perturbed by a wave function with amplitude a , wavelength λ or wavenumber k , so that the surface of the jet is represented by $r = R_0 + a \cos kz$. With a variation of the wavelength λ , two distinct convergence behaviors appear [8–20]. In the first case, the perturbation decreases in amplitude and the final state is a jet of uniform radius. In the second case, the jet decomposes into a chain of spherical particles and we describe this process as spheroidization.

According to the classic PR criterion, the jet simultaneously decomposes into a sequence of droplets when the wavelength of the perturbation is greater than the circumference of the cylinder $\lambda > 2\pi R_0$. Otherwise, the jet is morphologically stable.

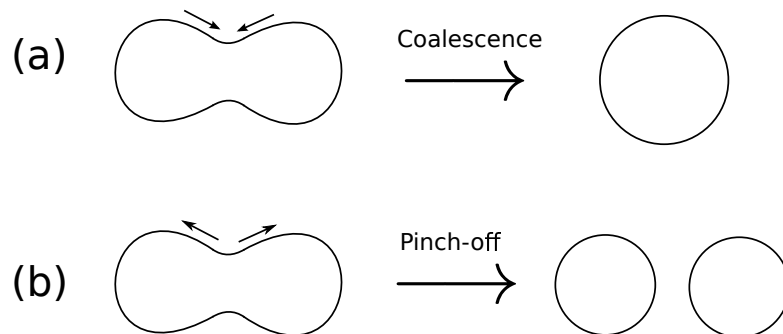


Figure 2.2: Illustration for coalescence and pinch-off.

2.2 The Plateau-Rayleigh theory

In literature, there are two types of theories to derive the morphological stability criterion of jets. The first type is based on the non-increasing free energy principle, in accordance with the basic thermodynamic law. Typical works of this kind are, for example, Rayleigh in 1878 [1] and 1879 [2], as well as Carter and Glaeser [4]. The second type is based on the linear [3] or non-linear stability analysis [5] focusing on the evolution equation. In all of the works, the following form of axisymmetrical perturbation

$$r = R_0 + a \cos kz, \quad (2.1)$$

is considered except of Rayleigh's theory in 1879 where he considers a perturbation of the form

$$r = R_0 + a_n \cos n\theta \cos kz, \quad (2.2)$$

where n is an integer, a_n is the perturbation amplitude, and θ is the angle in the polar coordinate of the perpendicular plane.

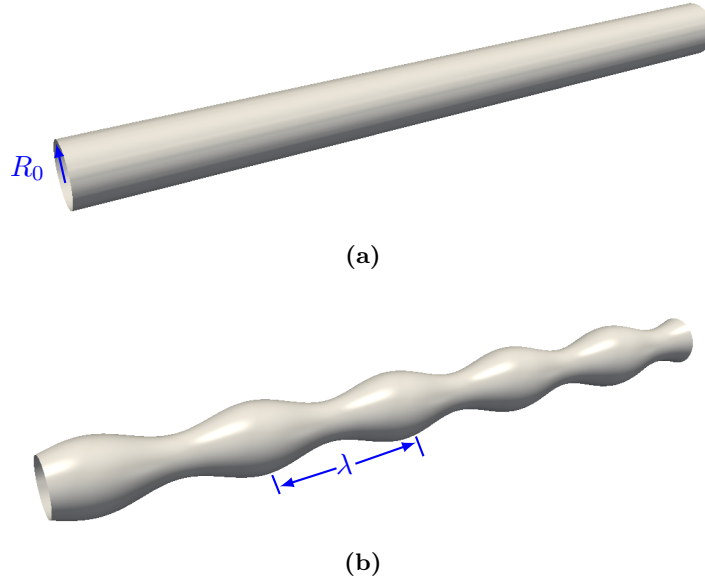


Figure 2.3: Schematic figure: (a) Illustration of a liquid cylinder with radius R_0 . (b) Description of a cylinder perturbed by a sinusoidal function $R_0 + a \cos(2\pi z/\lambda)$ in the radial direction, where λ and a are the wavelength and amplitude of the perturbation, respectively.

The perturbation of Eq. (2.1) is sketched in Fig. 2.3 and is a special case of Eq. (2.2) for $n = 0$. We denote the radius of the jet, which has the same volume as the perturbed state, as R_u . The relation between R_0 , R_u and a is obtained by the constraint of constant-volume, which gives rise to different results for the two sorts of perturbations. For the perturbation of Eq. (2.1), the relationship between R_0 , R_u and a is obtained by matching the volumes, $\pi R_u^2 \lambda = \int_0^\lambda \pi [R_0 + a \cos(kz)]^2 dz$, which yields that

$$R_u^2 = R_0^2 + a^2/2.$$

For the perturbation of Eq. (2.2), the equivalent of the volumes $\pi R_u^2 \lambda = \int_0^\lambda \int_0^{2\pi} \frac{1}{2} [R_0 + a \cos n\theta \cos kz]^2 d\theta dz$ yields two different results:

$$R_u^2 = \begin{cases} R_0^2 + a^2/2 & \text{for } n = 0, \\ R_0^2 + a^2/4 & \text{for } n = 1, 2, 3, \dots \end{cases} \quad (2.3)$$

These two distinct results are due to the fact that the integration $\int_0^{2\pi} \cos^2(n\theta) d\theta$ is 2π for $n = 0$ and is π for $n \neq 0$.

2.2.1 Surface energy minimization concept

2.2.1.1 The work of Rayleigh in 1878

Assuming isotropic surface tension σ , Rayleigh derived an expression for the difference of the surface energies before (E_u) and after (E_p) perturbations as [1]

$$E_p - E_u = \frac{\pi a^2 \sigma}{2R_0} \left[\left(\frac{2\pi R_0}{\lambda} \right)^2 - 1 \right].$$

According to the energy concept that lower free energy state is favored, the perturbed cylinder detaches into a string of spherical particles if the wavelength λ is greater than the circumference of the cylinder $2\pi R_0$. The jet is morphologically stabilized otherwise. Accordingly, Rayleigh obtained a critical perturbation wavelength for the morphological stabilization

$$\lambda_1^{\text{crit}} = 2\pi R_0. \quad (2.4)$$

The problem of this criterion is that the volumes of the initial and perturbed states are not equivalent, namely,

$$\int_0^\lambda \pi r^2 dz \neq \pi R_0^2 \lambda.$$

2.2.1.2 The work of Rayleigh in 1879

The careless consideration of the non-consistency of volume/mass at the compared states is subsequently amended by Rayleigh himself in 1879 [2]. The corrected form of the Plateau-Rayleigh criterion reads

$$\lambda_2^{\text{crit}} = 2\pi R_u, \quad (2.5)$$

where R_u is related to the radius R_0 and amplitude a , as shown in Eq. (2.3). The second form of the Plateau-Rayleigh criterion is also obtained from the energy minimization concept:

$$E_p - E_u = \frac{\pi a_n^2 \sigma}{4R_u} [(2\pi R_u/\lambda)^2 - 1], \quad (2.6)$$

where $E_u = (2\pi R_u \lambda) \sigma$ is the surface energy of a jet with uniform radius R_u . The acquisition of the term $(2\pi R_u \lambda) \sigma$ benefits from the binomial approximation for the radius R_0 [2]

$$R_0 = R_u - \frac{a^2}{8R_u}. \quad (2.7)$$

A comparison of Eq. (2.7) with Eq. (2.3) results in a residual term $\frac{a^4}{64R_u^2}$, which is negligible only if the amplitude is much less than the radius R_u . Hence, the second form of the Plateau-Rayleigh criterion merely holds for tiny perturbations. For the general case of finite amplitude, the Plateau-Rayleigh stability criterion fails to predict the morphological stabilization of jets, as pointed out by Carter and Glaeser [4].

2.2.1.3 The work of Carter and Glaeser in 1987

Carter and Glaeser [4] reexamined the Rayleigh stability criterion and found that the critical wavelength shifts away from that predicted by Rayleigh. The energy minimization concept which was used by Rayleigh is employed again by Carter and Glaeser. Assuming uniform surface tension, the calculation of the surface energy turns to the evaluation of the surface area and is expressed as

$$\begin{aligned} E_p &= \sigma \int_0^\lambda 2\pi r \sqrt{1 + \left(\frac{dr}{dz}\right)^2} dz \\ &= \frac{8\sigma\pi R_0 a}{\beta} E(\beta), \end{aligned} \quad (2.8)$$

where $\beta^2 = a^2 k^2 / (1 + a^2 k^2)$ and $E(\beta)$ is the complete integral of the second kind of modulus β . It is noteworthy that the evaluation of the surface energy has to be subject to the constraint of constant-volume.

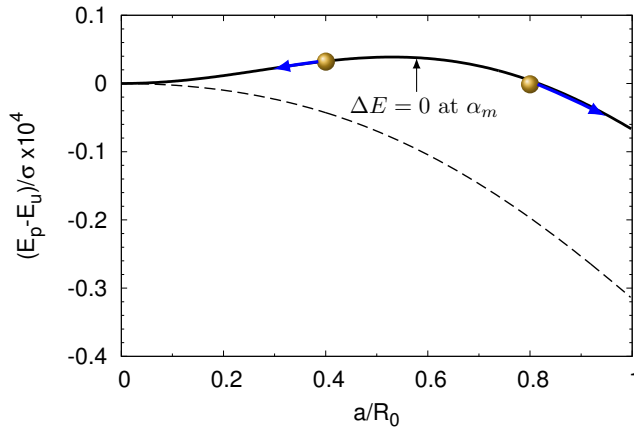


Figure 2.4: Illustration for the results of Carter and Glaeser [4]: the difference of the surface energy as a function of the ratio a/R_0 .

The work of Carter-Glaeser is summarized as two parts:

- (i) For $\lambda > 2\pi R_u$, the difference of the surface energy $\Delta E := E_p - E_u$ monotonically decreases with the scaled amplitude a/R_0 , as shown by the dashed line in Fig. 2.4. In this case, any perturbations increase in amplitude to decrease the surface energy, resulting in the spheroidization.
- (ii) For some wavelengths $\lambda < 2\pi R_u$, the surface energy passes through a maximum value at $a/R_0 = (a/R_0)_m =: \alpha_m$, as illustrated by the solid line in Fig. 2.4. To reduce the surface energy, the perturbations decrease in amplitude for $0 < a/R_0 < \alpha_m$ and increase in amplitude for $\alpha_m < a/R_0 < 1$, as sketched by the blue lines with arrows. Therefore, Carter and Glaeser proposed the following condition for

the critical configuration

$$\frac{dE_p}{da}. \quad (2.9)$$

The result (ii) indicates that for $\lambda < 2\pi R_u$, the perturbed jet is capable to transform into separated spheres as long as the amplitude is sufficiently large, in contrast to the PR criterion. However, the stability criterion of Carter and Glaeser is not given in a closed form. With the linear relativity as high as 0.99, Ma et al. [22] approximated the result of Carter and Glaeser as

$$\lambda_3^{\text{crit}} = 2\pi R_u(1 - 0.34a^2/R_u^2). \quad (2.10)$$

Another energy minimization concept for the spheroidization of jets is based on a comparison of the surface energy of the perturbed jet with the sphere which has the same volume. For a jet with mean radius R_u , the corresponding radius of the sphere is $R_s = (3R_u^2\lambda/4)^{1/3}$. For isotropic surface energy, the comparison of the surface energies turns to the evaluation of the surface areas, which yields that

$$\lambda_s^{\text{crit}} = 4.5R_u. \quad (2.11)$$

This stability criterion occasionally appears in some textbooks [23] and is obviously not accurate according to the work of Carter et al [4]. In Fig. 2.5 (a), I plot the normalized critical wavelength as a function of the scaled amplitude and compare the stability criterion of Eq. (2.11) (the horizontal solid line) with the one from Carter-Glaeser (the dashed line with triangles). According to the surface energy minimization concept of Carter and Glaeser, above the dashed line, the end-state of the jet is a row of droplets, and below the dashed line, the final state is a uniform radius cylinder. The

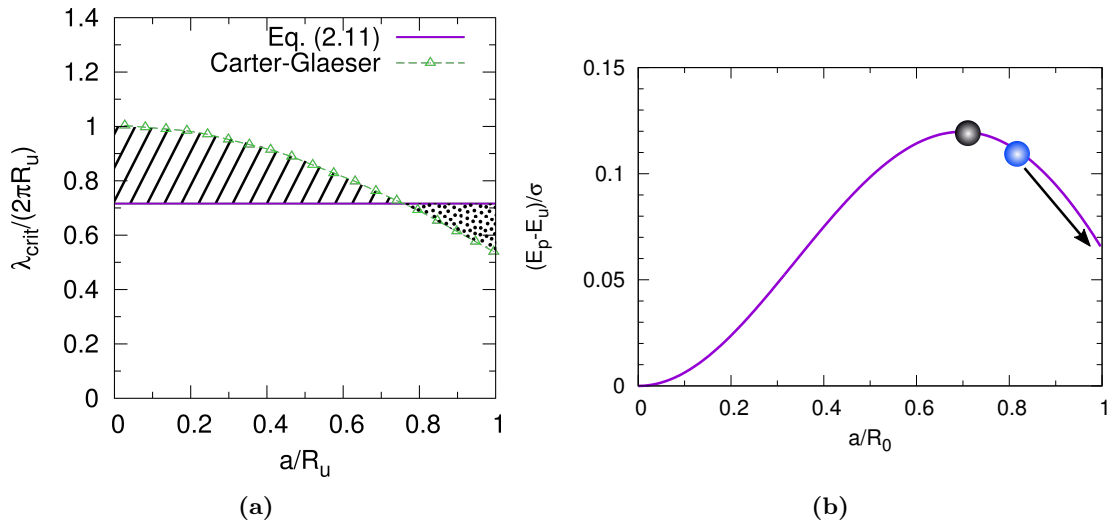


Figure 2.5: Illustration for the limitation of the criterion, Eq. (2.11).

stability criterion of Eq. (2.11) crosses with the result of Carter and Glaeser at around $a/R_u \approx 0.7$. According to the criterion of Eq. (2.11), there is a new morphologically unstable region (the hatched line filled area) and a new morphologically stable region (circle filled area). Herein, I highlight that these two regions are actually in conflict with the surface energy minimization concept and the corresponding explanation is shown in Fig. 2.5 (b), where I plot the difference of the surface energy $(E_p - E_u)/\sigma$ as a function of the scaled amplitude a/R_0 . As can be seen from the figure, the surface energy of the state of $a/R_0 = 1$, which corresponds to a droplet-structure, is higher than the state of $a/R_0 = 0$, which depicts a uniform radius cylinder. According to the criterion of Eq. (2.11), the final state has to be a uniform radius cylinder. However, if the initial state (the blue circle) locates at the right hand side of the energy barrier (black circle), the jet cannot converge to a uniform radius jet because of the existence of the energy barrier.

2.2.2 The wavelength corresponding to the maximum speed of breakup

Apart from the critical wavelength, Rayleigh has also derived a prevailing wavelength which corresponds to the fastest breakup. The derivation is based on the Lagrange equation with the estimated potential and kinetic energies.

According to the work of Rayleigh [2], the potential energy per unit length is expressed as

$$E' := E - 2\pi R_u \sigma = \frac{1}{4}\pi R_u^{-1} a_n^2 \sigma (k^2 R_u^2 + n^2 - 1),$$

where $2\pi R_u \sigma$ is the surface energy per unit length for a jet of uniform radius R_u and E is the surface energy per unit length for the perturbed jet. If n is unity or any greater integer, the difference of the surface energy E' is positive, indicating that the jet is morphologically stable. For $n = 0$, the jet is stable or unstable according as kR_u is greater or less than unity, which yields a critical perturbation wavelength, as shown in Eq. (2.5).

The kinetic energy per unit length is obtained by solving the Stokes equation in the cylindrical coordinate

$$K = \frac{1}{4}\pi \rho R_u^2 \frac{I_n(ikR_u)}{ikR_u I_n'(ikR_u)} \left(\frac{da_n}{dt} \right)^2, \quad (2.12)$$

where ρ is the density and I_n is the modified Bessel function of the n -th order. Knowing the kinetic as well as the potential energies, the motion of the fluid follows the Lagrange equation $\frac{d}{dt} \frac{\partial(E+K)}{\partial(\dot{a}_n)} = \frac{\partial(E+K)}{\partial a_n}$, yielding

$$\frac{d^2 a_n}{dt^2} + \frac{\sigma}{\rho R_u^3} \frac{ikR_u I_n}{I_n'(ikR_u)} (n^2 + k^2 R_u^2 - 1) a_n = 0.$$

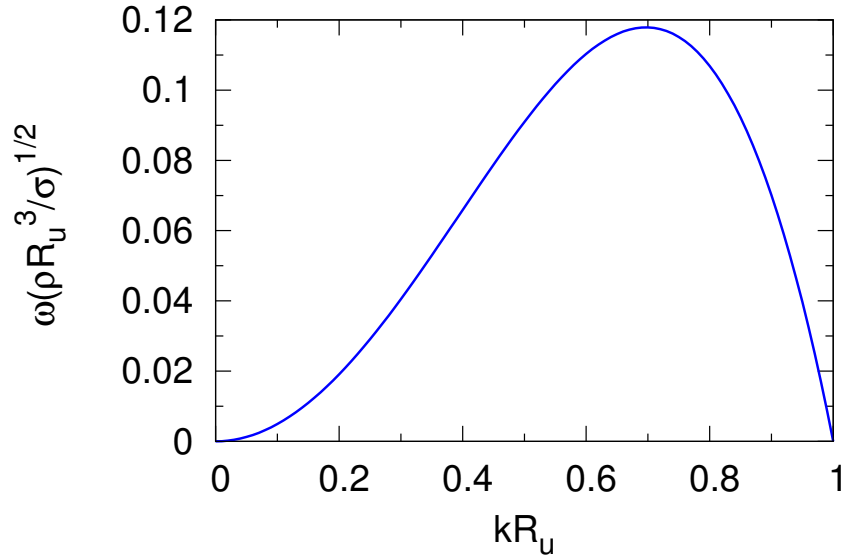


Figure 2.6: Dispersion relation for the morphological stability of rods according to Eq. (2.13).

If we assume $a_n \propto e^{\omega t}$, we obtain the following dispersion relation

$$\omega^2 = \frac{\sigma}{\rho R_u^3} \frac{ikR_u I_n'(ikR_u)}{I_n(ikR_u)} (n^2 + k^2 R_u^2 - 1). \quad (2.13)$$

The dispersion relation for $kR_u < 1$ and $n = 0$ is shown in Fig. 2.6, where the growth rate is scaled by $\sqrt{\rho R_u^3 / \sigma}$. We observe that the maximum growth rate occurs at $kR_u \approx 0.697$, which yields a wavelength corresponding to the maximum speed of the breakup

$$\lambda_m \approx \sqrt{2} \lambda_{\text{crit}} = 2\sqrt{2} \pi R_u.$$

2.2.3 Stability analysis

2.2.3.1 Linear stability analysis: the work of Nichols and Mullins

According to the derivation of Mullins [3], the normal velocity v_n at any point of a surface caused by the surface diffusion is expressed as

$$v_n = B_s \nabla_s^2 \kappa, \quad (2.14)$$

where the mobility B_s is related to the surface diffusivity D_s . For small-amplitude perturbations, the mean curvature is approximated as [3]

$$\kappa = \frac{1}{r} + \frac{d^2 r}{dz^2} = \frac{1}{R_0 + a \sin(2\pi z / \lambda)} + a(2\pi / \lambda)^2 \sin(2\pi z / \lambda). \quad (2.15)$$

Using the binomial expansion and only keeping the first order terms in a , we have

$$\frac{1}{R_0 + a \sin(2\pi z/\lambda)} \approx \frac{1}{R_0} - \frac{a \sin(2\pi z/\lambda)}{R_0^2}. \quad (2.16)$$

Substituting Eq. (2.15) and Eq. (2.16) into Eq. (2.14) yields that

$$v_n = B_s a (2\pi/\lambda)^2 \left[\frac{1}{R_0^2} - (2\pi/\lambda)^2 \right] \sin(2\pi z/\lambda). \quad (2.17)$$

The normal velocity of the interface can also be calculated as the derivative of the displacement with respect to time

$$v_n = \frac{dr}{dt} = \frac{dR_0}{dt} + \frac{da}{dt} \sin(2\pi z/\lambda). \quad (2.18)$$

Comparing Eq. (2.17) and Eq. (2.18), we have the following equalities

$$\frac{dR_0}{dt} = 0, \quad \frac{1}{a} \frac{da}{dt} = B_s (2\pi/\lambda)^2 \left[\frac{1}{R_0^2} - (2\pi/\lambda)^2 \right].$$

The critical geometrical configuration is given by the condition of $\frac{da}{dt} = 0$, which gives rise to a cutoff wavelength

$$\lambda_1^{\text{crit}} = 2\pi R_0, \quad (2.19)$$

as the result of Rayleigh in 1878.

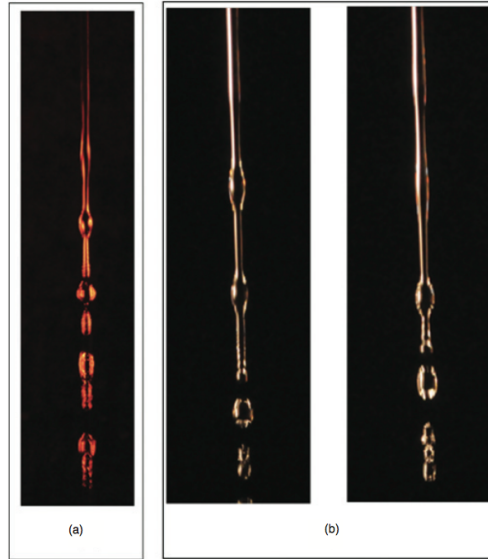


Figure 2.7: Formation of droplets viewed with a stroboscope light source and long exposure photograph (a) and a continuous light source and fast-shutter-speed photography (b). The figures are taken from Ref. [24].

2.2.3.2 Nonlinear stability analysis

Expanding the wave in terms of the ratio $\varepsilon := a/R_u$ till the third order

$$r = R_0 + \sum_{n=1}^3 \varepsilon^n R_u + \mathcal{O}(\varepsilon^4), \quad (2.20)$$

Nayfeh [5] performed a nonlinear stability analysis in the scope of fluid dynamics and obtained another critical wavelength

$$\lambda_4^{\text{crit}} = 2\pi R_u / [1 + 3a^2/4R_u^2]. \quad (2.21)$$

Herein, the initial wave does not remain in harmonic with time and this fact indicates the incompleteness of the result of Carter and Glaeser.

2.2.4 Applications of the Plateau-Rayleigh theory

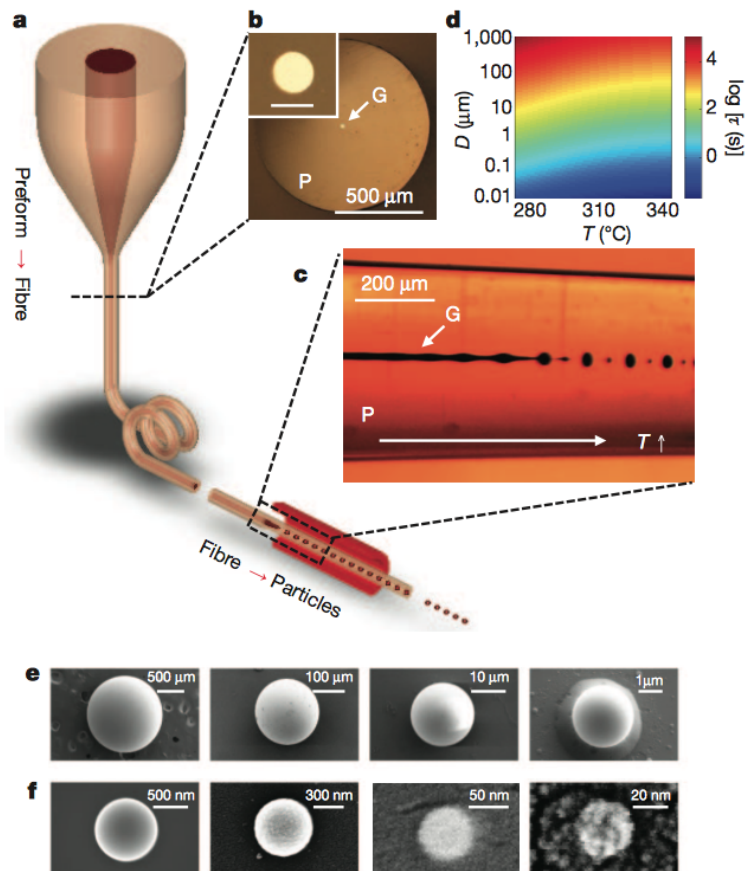


Figure 2.8: Fabrication of nanoparticles from nanofiber [26]: (a) A microscopic preform is thermally drawn into a fiber. (b) A magnification of the nanofiber. (c) Occurrence of the Plateau-Rayleigh instability. (d) The instability time as a function of temperature. (e) and (f) SEM images of the obtained nanoparticles. Reprinted with permission from Nature Publishing Group © 2012.

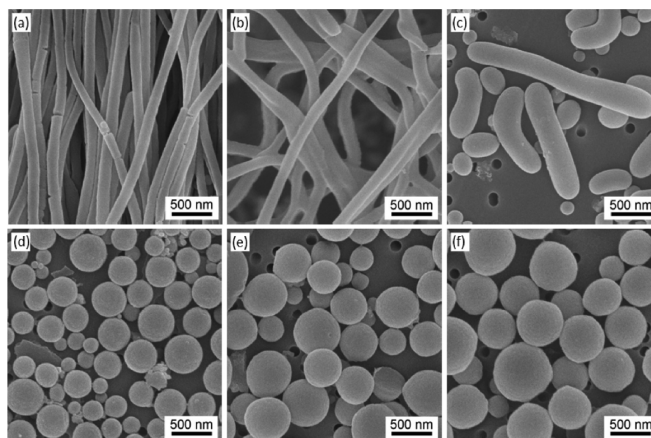


Figure 2.9: SEM images of Polymethyl methacrylate (PMMA) nanostructures by annealing PMMA nanofibers in ethylene glycol for 3 h at different temperatures: (a) room temperature, (b) 80, (c) 90, (d) 100, (e) 120, and (f) 140 °C. This figure is from Ref. [27].

The classic Plateau-Rayleigh stability criterion is used to understand lots of natural phenomena and has broad applications. Fig. 2.7 illustrates the formation of droplets under a water faucet [24]. When the water-column is falling down, it is stretched by the gravitational force. With distances far away from the faucet, we observe a chain of droplets. When the water-column is thin enough, the gravitational force is negligible in comparison with the surface tension force. Thus, the detachment of the water-column into a series of droplets can be understood using the Plateau-Rayleigh theory. Another daily example of Plateau-Rayleigh instability occurs in urination. The stream of urine experiences instability after about 15 cm, breaking into droplets, which causes significant splash-back on impacting a surface [25].

In engineering applications, the Plateau-Rayleigh instability is often used for the fabrication of uniformly sized, structured spherical particles spanning an exceptionally wide range of sizes. Fig. 2.8 shows a fabrication process of nanoparticles from nanofiber from a recent literature [26]. At the beginning, a microscopic preform is thermally drawn into a fiber. Subsequent thermal processing induces the Plateau-Rayleigh instability, which results in the detachment of the fiber. A magnification of the fiber is illustrated in Fig. 2.8 (b). Fig. 2.8 (c) shows the occurrence of the Plateau-Rayleigh instability when a temperature gradient is imposed along the fiber. The calculated instability time for different temperatures and diameters is given in Fig. 2.8 (d). Fig. 2.8 (e) and (f) show the SEM images of the obtained nanoparticles with diameters ranging from 20 nm to 500 μm .

In Fig. 2.9, I show another example which depicts the transformation of PMMA nanofibers to nanoparticles [27]. The PMMA nanofibers are annealed in ethylene glycol at different temperatures for 3 h. When the temperature is less than the glass transition temperature of PMMA, the fiber structure of the polymer is retained, as shown in Fig. 2.9

(a), (b) and (c). When the temperature is higher than the glass transition temperature, transformation from nanofiber to nanoparticles is observed, as illustrated in Fig. 2.9 (d), (e) and (f). The mechanism for the morphological change of the nanofiber is the Plateau-Rayleigh instability. The fabrication of nanospheres, which is based on the Plateau-Rayleigh theory, has been widely reported in many other references [28–33].

2.2.5 Capillary bridge

Fig. 2.10 illustrates a liquid jet with a length of λ . At the positions of $z = 0$ and $z = \lambda$, the liquid jet is in contact with two rigid bodies with an arbitrary shape, such as two planar surfaces shown in Fig. 2.10. This kind of setup is usually named as capillary bridge, which occurs, for instance, in the process of soldering [34], in atomic force microscopy [35] and in living nature [36]. Thermodynamically, the liquid jet takes the shape which has the lowest surface area. According to Rayleigh's criterion, if the length λ exceeds a critical value, the liquid bridge may be unstable and breaks up into two droplets, as illustrated in Fig. 2.10.

One significant difference of the capillary bridge from Rayleigh's consideration is that the liquid jet in the longitudinal dimension does not have free boundaries. At the contact boundaries, as highlighted by the black circles, the following force balance condition

$$\sigma_1 = \sigma_2 \cos \theta + \sigma_3 \quad (2.22)$$

has to be fulfilled. It is noted that Eq. (2.22) also holds, if the capillary bridge breaks up into two droplets. At static, the shape of the capillary bridge is obtained by using the Young-Laplace equation with a constraint of Eq. (2.22) at the contact [37].

2.3 Motion of droplets due to capillarity

After the breakup of the jet, the concentration along the surface of the resulted droplets may be non-uniform, if there is a mass transfer between the droplet-phase and the surrounding phase. Also, the shape of the droplet may slightly deviate from a sphere and the mean curvature along the surface of the droplet is inhomogeneous. According to the Gibbs-Thomson effect, the interfacial concentration along the surface of the droplet is inhomogeneous as well. Consequently, the concentration gradients at the surface of the droplet induce a flow, as sketched in Fig. 2.11. This kind of phenomenon occurs in daily lives, e.g., when we mix the salad, we see the motion and coarsening of oil droplets suspended in vinegar. This sort of motion has also been *in situ* captured in the Al-Bi alloy [38]. This phenomenon was primarily explained by Brownian motion [39]. However, it has been recently demonstrated that the motion of the droplets is caused by the gradient of the concentration or surface tension [40].

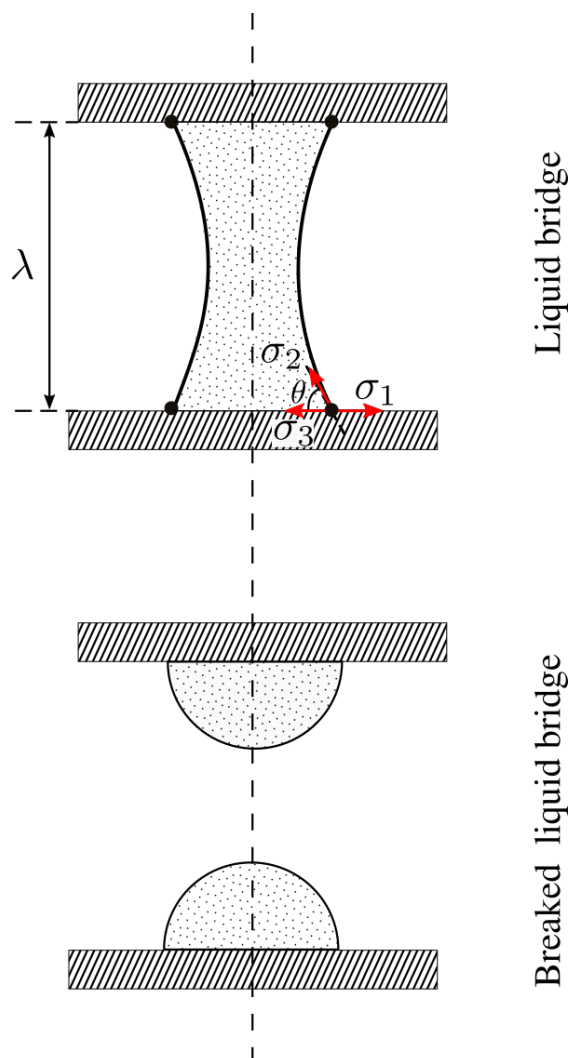


Figure 2.10: Illustration for a capillary bridge and its breakup state.

For a small capillary number, the droplet stays in the form of a sphere or nearly a sphere. A natural choice to address the motion of the droplet is to solve the system equations in the polar or bipolar coordinate. In the motion process, the mass transport follows the convective diffusion equation, which transfers into the Laplace equation when the Péclet number of the system is much less than unity. For an incompressible flow, the convection profile is obtained by solving the biharmonic equation for the stream function. The general solutions of the Laplace equation and the biharmonic equation have been derived by Stimson and Jeffery [41, 42]. The Laplace equation and the biharmonic equation are coupled by the condition of force balance between the capillary force and the viscosity force.

The effect of capillarity on the motion of droplets has been widely studied. Golovin et al. [43] theoretically calculated the motion speed of the droplets when two droplets approach each other. The analysis of Golovin et al. is carried out in the bipolar coordinate based on the general solutions found by Stimson and Jeffery. The similar strategy

has been employed by, for example, Haber et al. [44], Meyyappan et al. [45] and Keh et al. [46], to study the motion of two droplets due to thermal gradients. Those mentioned theoretical studies have been partially confirmed by the recent numerical experiments. For instance, Shimizu and Tanaka [40] studied the motion of droplets in the process of phase separation by employing the Cahn-Hilliard-Navier-Stokes equation, which is sometimes known as model H according to the notation of Hohenberg and Halperin [47]. They found that in the process of phase separation, the barycenter of the droplets moves in a particular direction, in contrast to the stochastic motion. This kind of motion behavior provides an evidence that the motion is driven by the capillary force rather than due to Brownian motion. Although Shimizu and Tanaka in their publication stated that the directional motion is a novel mechanism, the motion, coalescence and coarsening due to surface tension have been realized at least 30 years ago (see Ref. [43]).

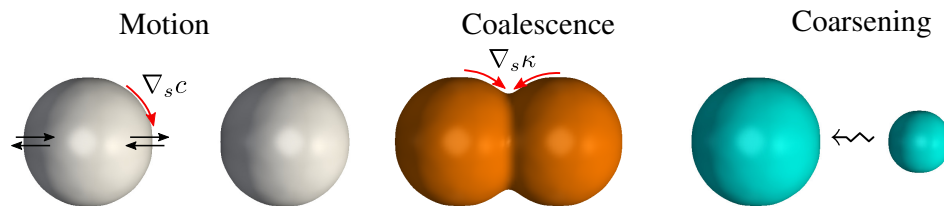


Figure 2.11: Illustration for the effect of capillarity on the motion, coalescence and coarsening of droplets.

Chapter 3

Methods: The Cahn-Hilliard-Navier-Stokes and the Allen-Cahn models

In this chapter, I present two phase-field models that are used for the numerical experiments. The first one is the Cahn-Hilliard-Navier-Stokes model, which has been published in Ref. [48]. This model is a combination of the Cahn-Hilliard model with the Navier-Stokes equation, where the former one is for the mass conservation and the latter one concerns the momentum conservation. In the convective Cahn-Hilliard equation, the flux contains two contributions: one from diffusion, which is caused by the gradient of chemical potential, and the other from the capillary flow, which is induced by the gradient of curvature. The capillary flow is modeled by the capillary tensor, which is derived either from the Cahn-Hoffman- ξ vector [49] or with the aid of Noether's theorem [50]. In the second part, I briefly overview the volumed-preserved Allen-Cahn model, which was introduced by Nestler al. [51]. In contrast to the conserved order parameter of concentration in the Cahn-Hilliard model, the order parameter ϕ in the Allen-Cahn model is not a conserved variable. The fundamental concept of both models is to minimize the free energy or to maximize the entropy functional of the system, in accordance with the second law of thermodynamics.

Model I: The Cahn-Hilliard-Navier-Stokes model

3.1 The free energy functional for non-uniform systems

I consider a two-phase system composed of two components. The two phases are separated by a diffuse interface in the length scale of d_0 , where d_0 is the capillary length. The free energy functional for the non-uniform system is obtained by integrating the free energy density over the domain V

$$\mathcal{F}(c) = \int_V g(c, \nabla c, \nabla^2 c, \dots) dx,$$

where the free energy density g depends on the mole fraction c and the derivatives ∇c , $\nabla^2 c$, \dots . A Taylor expansion of the free energy density with respect to the uniform state yields

$$\begin{aligned} g(c, \nabla c, \nabla^2 c, \dots) = & g_0(c) + \sum_i \frac{\partial g}{\partial \frac{\partial c}{\partial x_i}} \Big|_0 \left(\frac{\partial c}{\partial x_i} - 0 \right) + \sum_{i,j} \frac{\partial g}{\partial \frac{\partial^2 c}{\partial x_i \partial x_j}} \Big|_0 \left(\frac{\partial^2 c}{\partial x_i \partial x_j} - 0 \right) \\ & + \frac{1}{2!} \sum_{i,j} \frac{\partial^2 g}{\partial \frac{\partial c}{\partial x_i} \partial \frac{\partial c}{\partial x_j}} \Big|_0 \left(\frac{\partial c}{\partial x_i} - 0 \right) \left(\frac{\partial c}{\partial x_j} - 0 \right) + \dots, \end{aligned} \quad (3.1)$$

where the subscript $|_0$ denotes the value evaluated at the uniform state. The free energy density of an isotropic system is a scalar value, which is invariant to the symmetric operations: reflection and rotation. Hence, we have the following equalities

$$\frac{\partial g}{\partial \frac{\partial c}{\partial x_i}} \Big|_0 = 0, \quad \forall i, \quad \frac{\partial g}{\partial \frac{\partial^2 c}{\partial x_i \partial x_j}} \Big|_0 = 0, \quad i \neq j, \quad \frac{\partial^2 g}{\partial \frac{\partial c}{\partial x_i} \partial \frac{\partial c}{\partial x_j}} \Big|_0 = 0, \quad i \neq j.$$

With the definition

$$\kappa_1 := \frac{\partial g}{\partial \frac{\partial^2 c}{\partial x_i^2}}, \quad \kappa_2 := \frac{1}{2} \frac{\partial^2 g}{\partial \frac{\partial c}{\partial x_i} \partial \frac{\partial c}{\partial x_i}},$$

Eq. (3.1) is reduced to

$$g(c, \nabla c, \nabla^2 c, \dots) = g_0(c) + \kappa_1 \nabla^2 c + \kappa_2 (\nabla c)^2.$$

The free energy functional is thus rewritten as

$$\mathcal{F}(c) = \int_V [g_0(c) + \kappa_1 \nabla^2 c + \kappa_2 (\nabla c)^2] dx.$$

The Laplace term $\kappa_1 \nabla^2 c$ is equivalent to $\nabla \cdot (\kappa_1 \nabla c) - d\kappa_1/dc(\nabla c)^2$. Utilizing the divergence theorem and the homogeneous Neumann boundary condition

$$\int_V \nabla \cdot (\kappa_1 \nabla c) = \int_{\partial V} \kappa_1 \nabla c \cdot \mathbf{n} d\ell, \quad \nabla c \cdot \mathbf{n} = 0 \text{ at } \partial V,$$

we obtain the final expression for the free energy functional

$$\mathcal{F}(c) = \int_V [f(c) + \kappa_c(\nabla c)^2] dx, \quad (3.2)$$

where the following definitions: $f := g_0$ and $\kappa_c := \kappa_2 - d\kappa_1/dc$ have been made. According to the definition, it is evident that $f(c)$ is the free energy density of the bulk phase. The modeling parameter κ_c is often called the gradient energy coefficient, which is related to the width of the diffuse interface and the interfacial energy.

3.2 A mathematical definition of the chemical potential and the Cahn-Hilliard model

3.2.1 Definition of the chemical potential in a tangent functional space

Let us define the following notations:

- $\mathcal{F} \in H^1$, where H^1 is the Sobolev space
- Functional $\mathcal{F} : H^1(V) \rightarrow \mathbb{R}$
- The Gâteaux derivative $\mathcal{F}'(c) : H^1 \rightarrow T_c H^1$, where $T_c H^1$ is the tangent space at c in H^1
- $h(c, \nabla c) := f(c) + \kappa_c(\nabla c)^2$

Similar to the Fréchet derivative, the Gâteaux derivative for a functional \mathcal{F} is defined as

$$\mathcal{F}'(c)[\psi] = \left. \frac{d}{d\epsilon} \mathcal{F}(c + \epsilon\psi) \right|_{\epsilon=0}, \quad (3.3)$$

where ψ is a test function in the tangent space $T_c H^1$. I look for the representation of the Gâteaux derivative $\mathcal{F}'(c)[\psi]$

$$\mathcal{F}'(c)[\psi] = \langle \mu, \psi \rangle, \forall \psi \in T_c H^1, \quad (3.4)$$

where μ is a function in the tangent space $T_c H$ and is defined as the chemical potential. Substituting Eq. (3.2) into Eq. (3.3) yields

$$\begin{aligned} \mathcal{F}'(c)[\psi] &= \left[\frac{d}{d\epsilon} \int_V h(c + \epsilon\psi, \nabla c + \epsilon\nabla\psi) \right] \Big|_{\epsilon=0} \\ &= \int_V \partial_1 h(c, \nabla c) \psi + \partial_2 h(c, \nabla c) \cdot \nabla \psi \\ &= \int_V \partial_1 h(c, \nabla c) \psi + \nabla \cdot [\partial_2 h(c, \nabla c) \psi] - [\nabla \cdot \partial_2 h(c, \nabla c)] \psi. \end{aligned} \quad (3.5)$$

With the divergence theorem

$$\int_V \nabla \cdot [\partial_2 h(c, \nabla c)] = \int_{\partial V} \partial_2 h(c, \nabla c) \cdot \mathbf{n}$$

and the boundary condition $\partial_2 h(c, \nabla c) \cdot \mathbf{n} = 0$, Eq. (3.5) is rearranged as

$$\begin{aligned} \mathcal{F}'(c)[\psi] &= \int_V [\partial_1 h(c, \nabla c) - \nabla \cdot \partial_2 h(c, \nabla c)] \psi \\ &= \langle \partial_1 h(c, \nabla c) - \nabla \cdot \partial_2 h(c, \nabla c), \psi \rangle, \quad \forall \psi \in T_c H^1. \end{aligned} \quad (3.6)$$

A comparison between Eq. (3.4) and Eq. (3.6), we obtain the expression for the chemical potential μ

$$\mu = \partial_1 h(c, \nabla c) - \nabla \cdot \partial_2 h(c, \nabla c).$$

For $h(c, \nabla c) = f(c) + \kappa_c (\nabla c)^2$, the chemical potential is further expressed as

$$\mu = f_{,c} - 2\kappa_c \nabla^2 c.$$

3.2.2 The Cahn-Hilliard model

When the chemical potential is uniformly distributed, the system is in the thermodynamic equilibrium. When the distribution of the chemical potential is inhomogeneous, there is a diffusion mass flux \mathbf{J} , which drives the system to reach the thermodynamic equilibrium. It is postulated that the mass flux is proportional to the gradient of the chemical potential

$$\mathbf{J} = -\Lambda \nabla \mu,$$

where Λ is the mobility. In comparison with the mass flux given by Fick's law $\mathbf{J} = -D \nabla c$ (D —the diffusion coefficient) and with the relation $\nabla \mu = \mu_{,c} \nabla c$, the mobility is calculated by $\Lambda = D/\mu_{,c}$. For an ideal solution model, we obtain $\mu_{,c} = R_g T/[v_m(1-c)c]$, where R_g is the universal gas constant and v_m is the molar volume. Hence, the mobility is computed as follows

$$\Lambda = D \frac{v_m}{R_g T} c(1-c).$$

The temporal evolution of the mole fraction c follows the mass conservation equation

$$\partial_t c = -\nabla \cdot \mathbf{J}. \quad (3.7)$$

Substituting the expressions for the mass flux, chemical potential and the mobility into Eq. (3.7), we obtain the Cahn-Hilliard model

$$\partial_t c = \nabla \cdot \left[D \frac{v_m}{R_g T} c(1-c) \nabla (f_{,c} - 2\kappa_c \nabla^2 c) \right].$$

3.3 Capillary tensor and the Cahn-Hilliard-Navier-Stokes model

Apart from diffusion, convection is another mass transport mechanism for liquid phases. For a liquid phase with a local velocity of \mathbf{u} , the mass flux is formulated as

$$\mathbf{J} = -\Lambda \nabla \mu + \mathbf{u}c, \quad (3.8)$$

where the first term is the mass flux due to diffusion because of the gradient of chemical potential and the second term is the mass flux as a result of convection. In the present work, we particularly focus on the convection \mathbf{u} that is induced by the capillary force.

3.3.1 The stress balance at a fluid-fluid interface and the capillary tensor

Considering a fluid-fluid interface shown in Fig. 3.1, the force balance between the inertial force, body force \mathbf{f} , viscosity force and surface force is expressed as

$$\int_V \rho \frac{D\mathbf{u}}{dt} dV = \int_V \mathbf{f} dV + \int_C \sigma s dl + \int_S (\mathbf{n} \cdot \underline{\underline{\mathbf{T}}}^{L_1} - \mathbf{n} \cdot \underline{\underline{\mathbf{T}}}^{L_2}) dS,$$

where $\underline{\underline{\mathbf{T}}}^i := -p^i \mathbf{I} + \eta^i (\nabla \mathbf{u} + \nabla \mathbf{u}^T)$, $i = L_1, L_2$ is the viscosity stress tensor, \mathbf{I} is the identity tensor, η is the dynamic viscosity, V represents the volume, S denotes the surface area, C is the arc-length, and \mathbf{n} is the normal vector. For a fluid-fluid interface

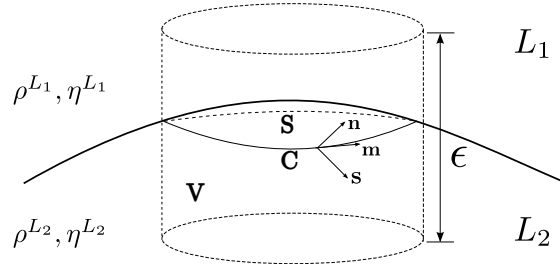


Figure 3.1: Schematic illustration for the stress balance at a fluid-fluid interface.

with a length of ϵ , the body force and the inertial force both are scaled by ϵ^3 , but the surface force is scaled by ϵ^2 . With Stokes theorem and considering the force in the order of ϵ^2 , the stress balance condition for the surface force at a fluid fluid interface, in the limit $\epsilon \rightarrow 0$, yields [52]

$$\sigma(\nabla \cdot \mathbf{n})\mathbf{n} - (\mathbf{I} - \mathbf{n} \otimes \mathbf{n}) \cdot \nabla \sigma = \mathbf{n} \cdot \underline{\underline{\mathbf{T}}}^{L_1} - \mathbf{n} \cdot \underline{\underline{\mathbf{T}}}^{L_2}, \quad (3.9)$$

where the left hand side is the general expression for the surface force acting on the liquid-liquid interface. The first term $\sigma(\nabla \cdot \mathbf{n})\mathbf{n}$ is the curvature force and the second

term which is simply equivalent to $\nabla_s \sigma$ is the Marangoni force due to non-uniform interfacial tension.

From the stress balance condition Eq. (3.9), the interfacial force

$$\mathbf{F}_s = \sigma \kappa \mathbf{n} - \nabla_s \sigma$$

has to be included for the temporal evolution of the liquid-liquid interface. In the Cahn-Hilliard model, we formulate the interfacial force in a conservative manner

$$\mathbf{F}_d = -\nabla \cdot \underline{\underline{\Theta}}, \quad (3.10)$$

where $\underline{\underline{\Theta}}$ is a potential energy tensor. According to Noether's theorem as well as the derivation (see Appendix A), we use the following form for the potential tensor

$$\underline{\underline{\Theta}} = 2\kappa_c \nabla c \otimes \nabla c - \kappa_c (\nabla c)^2 \mathbf{I}.$$

The equivalence between the sharp and diffuse interface descriptions (\mathbf{F}_s and \mathbf{F}_d) can be demonstrated in the following way. We distribute the sharp interface description $\mathbf{F}_s = \sigma \kappa \mathbf{n} - \nabla_s \sigma$ into the diffuse interface by multiplying a Delta function: $(\sigma \kappa \mathbf{n} - \nabla_s \sigma) \delta_\Sigma$, where the Delta function δ_Σ satisfies $\int_{-\infty}^{\infty} \delta_\Sigma = 1$. Tedious mathematical manipulations show that the conservative formulation $\mathbf{F}_d = -\nabla \cdot \underline{\underline{\Theta}}$ is equivalent to $(\sigma \kappa \mathbf{n} - \nabla_s \sigma) \delta_\Sigma$ [53]. The benefit of using the diffuse description is that the interfacial force in Eq. (3.9) is simultaneously incorporated and the explicit-tracking of the fluid-fluid interface is avoided.

3.3.2 The Cahn-Hilliard-Navier-Stokes equation

The convective Cahn-Hilliard equation is obtained by substituting the mass flux Eq. (3.8) into the mass conservation equation Eq. (3.7), yielding

$$\partial_t c + \nabla \cdot (\mathbf{u}c) = \nabla \cdot \left[D \frac{v_m}{R_g T} c(1-c) \nabla (f_{,c} - 2\kappa_c \nabla^2 c) \right], \quad (3.11)$$

where the convective term is equivalent to $\nabla \cdot (\mathbf{u}c) = \mathbf{u} \cdot \nabla c + c \nabla \cdot \mathbf{u}$. With the incompressibility condition

$$\nabla \cdot \mathbf{u} = 0, \quad (3.12)$$

Eq. (3.11) is rearranged as

$$\partial_t c + \mathbf{u} \cdot \nabla c = \nabla \cdot \left[D \frac{v_m}{R_g T} c(1-c) \nabla (f_{,c} - 2\kappa_c \nabla^2 c) \right]. \quad (3.13)$$

With the interfacial force in Eq. (3.10), the generalized Navier-Stokes equation reads

$$\rho(\partial_t \mathbf{u} + \mathbf{u} \cdot \nabla \mathbf{u}) = \nabla \cdot (-p \mathbf{I} - \underline{\underline{\Theta}} + \underline{\underline{\mathbf{T}}}). \quad (3.14)$$

Substituting the formulations for the capillary tensor $\underline{\underline{\Theta}}$ and the viscosity tensor $\underline{\underline{\mathbf{T}}}$ into Eq. (3.14), we obtain the final expression for the Navier-Stokes equation

$$\rho(\partial_t \mathbf{u} + \mathbf{u} \cdot \nabla \mathbf{u}) = -\nabla p + \nabla \cdot [\kappa_c (\nabla c)^2 \mathbf{I} - 2\kappa_c \nabla c \otimes \nabla c] + \nabla \cdot [\eta (\nabla \mathbf{u} + \nabla \mathbf{u}^T)]. \quad (3.15)$$

In summary, Eqs. (3.12), (3.13), and (3.15) consist of the system equations in the present work. The evolution of the mole fraction c follows the convective Cahn-Hilliard equation Eq. (3.13) and the convection field of the fluids is given by the Navier-Stokes equation with the capillary tensor Eq. (3.15). The pressure in the Navier-Stokes equation is obtained by solving the Poisson equation Eq. (3.12).

3.3.3 Non-dimensionalization of the Cahn-Hilliard-Navier-Stokes equation

The capillary length for a chemical model is expressed as [54]

$$d_0 = \frac{\sigma}{(\Delta c)^2 \mu_c}, \quad (3.16)$$

where Δc is the difference of the equilibrium mole fraction of species c in the two immiscible liquids. For immiscible liquids in alloys, the interfacial tension ranges from 0.01 N/m to 0.1 N/m. Tab. 3.1 tabulates the interfacial tensions for the immiscible liquids in several alloy systems with a miscibility gap. For an ideal solution model, we obtain $\mu_c = R_g T / (v_m c(1 - c))$. With $\Delta c \sim 0.1$, the capillary length d_0 ranges from 10^{-8} m to 10^{-10} m.

Parameters	σ
Cu-Pb	0.02
Al-In	0.04
Al-Bi	0.06
Al-Pb	0.14
Zn-Bi	0.06
Cd-Ga	0.03
Fe-Sn	0.09

Table 3.1: Interfacial tension for immiscible liquids [55].

The width of the diffuse interface between the two immiscible liquids is characterized by the capillary length. We thus choose d_0 , d_0^2/D and $R_g T_m / v_m$ as dimensionless factors

for the spatial length, time and free energy density, respectively. Moreover, the velocity \mathbf{u} , pressure p , gradient energy coefficient κ_c are non-dimensionalized as follows

$$\mathbf{u} = (D/d_0)\tilde{\mathbf{u}}, \quad p = (d_0^2/\rho D^2)\tilde{p}, \quad \kappa_c = (d_0^2 R_g T_m / v_m)\tilde{\kappa}_c.$$

Here, the tilt symbols stand for the corresponding physical parameters in the dimensionless form. With these dimensionless parameters, the system equations Eqs. (3.12), (3.13), and (3.15) are rearranged as

$$\partial_t c + \mathbf{u} \cdot \nabla c = \nabla \cdot \left[T_m / T c (1 - c) \nabla (f_{,c} - 2\kappa_c \nabla^2 c) \right], \quad (3.17)$$

$$\partial_t \mathbf{u} + \mathbf{u} \cdot \nabla \mathbf{u} = -\nabla p + M \nabla \cdot [(\nabla c)^2 \mathbf{I} - 2\nabla c \otimes \nabla c] + (1/Re) \nabla \cdot [(\nabla \mathbf{u} + \nabla \mathbf{u}^T)], \quad (3.18)$$

where the dimensionless parameters M and Re are expressed as $M = \kappa_c / (\rho D^2)$ and $Re = \rho D / \eta$, respectively.

3.3.4 Discretization and staggered mesh

The system equations are discretized on a staggered mesh [56], as sketched in Fig. 3.2¹. For a rectangle mesh with a size of $L \times W \times H$, we divide the mesh into a discretized domain $N_x \Delta x \times N_y \Delta y \times N_z \Delta z$, where $L = N_x \Delta x$, $W = N_y \Delta y$, and $H = N_z \Delta z$. The scalar data, e.g., the mole fraction c , is located in the center of each cell, as denoted by $c_{i,j}$ in Fig. 3.2 (a). The velocity components u and v are set at the border of the cell, as illustrated in Fig. 3.2 (a) for a two-dimensional case and in Fig. 3.2 (b) for a three-dimensional situation.

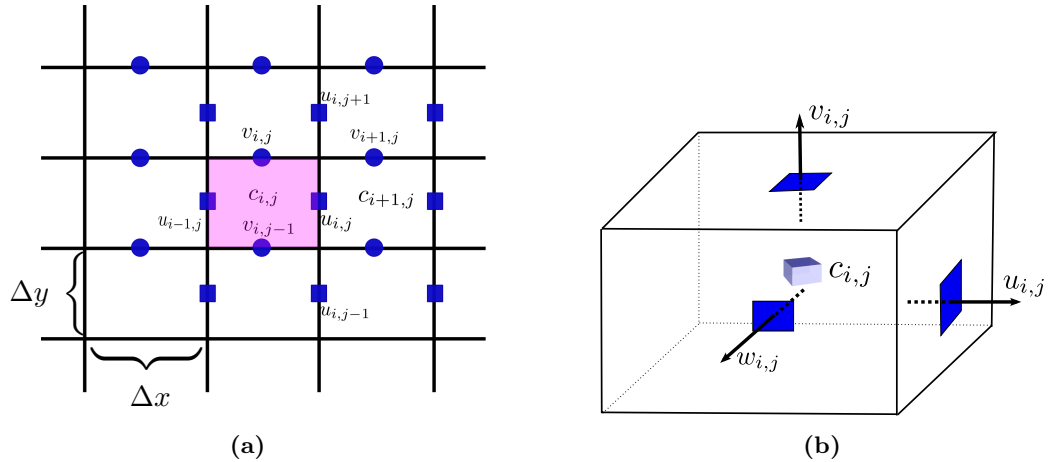


Figure 3.2: Schematic figure for the staggered grid.

¹A.C. and M.S. contributed to the implementation of the Cahn-Hilliard-Navier-Stokes model. The discretization is based on a former work of M.S. in his master thesis. The difference is that M.S. did the implementation for the AC model for the parameter ϕ , whereas I extend the implementation for the CHNS model for the parameter c .

The time derivative is approximated by the explicit Euler scheme

$$\partial_t c_i = (c_i^{n+1} - c_i^n)/\Delta t + \mathcal{O}(\Delta t).$$

The spatial derivative is computed as follows

$$\begin{aligned}\partial_x c^n &= (c_{i+1,j,k}^n - c_{i,j,k}^n)/\Delta x + \mathcal{O}(\Delta x), \\ \partial_y c^n &= (c_{i,j+1,k}^n - c_{i,j,k}^n)/\Delta y + \mathcal{O}(\Delta y), \\ \partial_z c^n &= (c_{i,j,k+1}^n - c_{i,j,k}^n)/\Delta z + \mathcal{O}(\Delta z).\end{aligned}$$

The higher order derivative is discretized by the central difference scheme

$$\begin{aligned}\nabla^2 c^n &= (c_{i+1,j,k}^n - 2c_{i,j,k}^n + c_{i-1,j,k}^n)/\Delta x^2 + (c_{i,j+1,k}^n - 2c_{i,j,k}^n + c_{i,j-1,k}^n)/\Delta y^2 \\ &\quad + (c_{i,j,k+1}^n - 2c_{i,j,k}^n + c_{i,j,k-1}^n)/\Delta z^2 + \mathcal{O}(\Delta x^2) + \mathcal{O}(\Delta y^2) + \mathcal{O}(\Delta z^2)\end{aligned}$$

and

$$\begin{aligned}\nabla^4 c^n &= (c_{i+2,j,k}^n - 4c_{i+1,j,k}^n + 6c_{i,j,k}^n - 4c_{i-1,j,k}^n + c_{i-2,j,k}^n)/\Delta x^4 + \mathcal{O}(\Delta x^4) \\ &\quad + (c_{i,j+2,k}^n - 4c_{i,j+1,k}^n + 6c_{i,j,k}^n - 4c_{i,j-1,k}^n + c_{i,j-2,k}^n)/\Delta y^4 + \mathcal{O}(\Delta y^4) \\ &\quad + (c_{i,j,k+2}^n - 4c_{i,j,k+1}^n + 6c_{i,j,k}^n - 4c_{i,j,k-1}^n + c_{i,j,k-2}^n)/\Delta z^4 + \mathcal{O}(\Delta z^4).\end{aligned}$$

The convective term $\mathbf{u} \cdot \nabla c$ is discretized by the upwind scheme.

The capillary stress tensor $\underline{\underline{\Theta}}$ and the viscosity stress tensor $\underline{\underline{\mathbf{T}}}$ can be written as

$$\underline{\underline{\Theta}} = \begin{pmatrix} \theta^{xx} & \theta^{xy} & \theta^{xz} \\ \theta^{yx} & \theta^{yy} & \theta^{yz} \\ \theta^{zx} & \theta^{zy} & \theta^{zz} \end{pmatrix} \quad \text{and} \quad \underline{\underline{\mathbf{T}}} = \begin{pmatrix} \tau^{xx} & \tau^{xy} & \tau^{xz} \\ \tau^{yx} & \tau^{yy} & \tau^{yz} \\ \tau^{zx} & \tau^{zy} & \tau^{zz} \end{pmatrix},$$

respectively. The divergence of the capillary tensor results in a vector for the interfacial force. The components of the vector are denoted by $\nabla \cdot \underline{\underline{\Theta}}|_x$, $\nabla \cdot \underline{\underline{\Theta}}|_y$, and $\nabla \cdot \underline{\underline{\Theta}}|_z$, which is responsible for the temporal evolution of the velocity in the x , y , and z directions, respectively. The divergence of the capillary stress tensor is discretized as follows

$$\begin{aligned}\nabla \cdot \underline{\underline{\Theta}}|_x &= \frac{\theta_{i+\frac{1}{2},j,k}^{xx} - \theta_{i-\frac{1}{2},j,k}^{xx}}{\Delta x} + \frac{\theta_{i,j+\frac{1}{2},k}^{yx} - \theta_{i,j-\frac{1}{2},k}^{yx}}{\Delta y} + \frac{\theta_{i,j,k+\frac{1}{2}}^{zx} - \theta_{i,j,k-\frac{1}{2}}^{zx}}{\Delta z}, \\ \nabla \cdot \underline{\underline{\Theta}}|_y &= \frac{\theta_{i+\frac{1}{2},j,k}^{xy} - \theta_{i-\frac{1}{2},j,k}^{xy}}{\Delta x} + \frac{\theta_{i,j+\frac{1}{2},k}^{yy} - \theta_{i,j-\frac{1}{2},k}^{yy}}{\Delta y} + \frac{\theta_{i,j,k+\frac{1}{2}}^{zy} - \theta_{i,j,k-\frac{1}{2}}^{zy}}{\Delta z}, \\ \nabla \cdot \underline{\underline{\Theta}}|_z &= \frac{\theta_{i+\frac{1}{2},j,k}^{xz} - \theta_{i-\frac{1}{2},j,k}^{xz}}{\Delta x} + \frac{\theta_{i,j+\frac{1}{2},k}^{yz} - \theta_{i,j-\frac{1}{2},k}^{yz}}{\Delta y} + \frac{\theta_{i,j,k+\frac{1}{2}}^{zz} - \theta_{i,j,k-\frac{1}{2}}^{zz}}{\Delta z},\end{aligned}$$

where the discretizations in the x and y dimensions are schematically illustrated in

Fig. 3.3 and the calculations for the components of the stress tensor at each point are listed in Tab. 3.2.

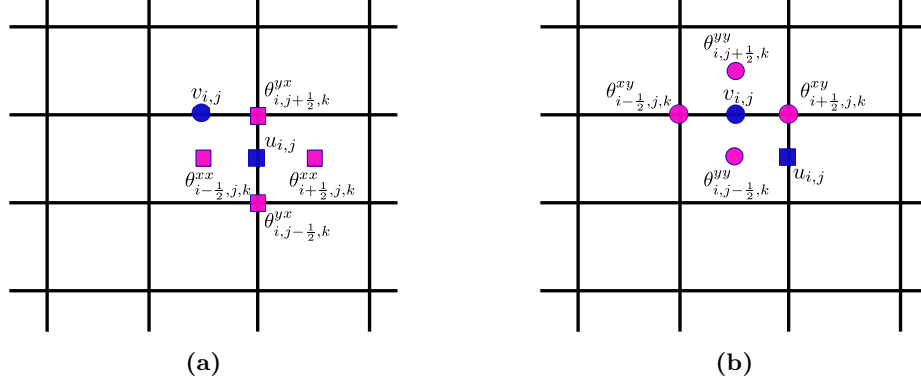


Figure 3.3: Discretization for the divergence of the capillary stress tensor.

Defining

$$\begin{aligned}
 F^n &= \Delta t[-M\nabla \cdot \underline{\underline{\Theta}}_x^n + (1/Re)\nabla \cdot \underline{\underline{\mathbf{T}}}_x^n - \partial_{xx}u^2 - \partial_{yy}(uv)^n - \partial_{zz}(uw)^n], \\
 G^n &= \Delta t[-M\nabla \cdot \underline{\underline{\Theta}}_y^n + (1/Re)\nabla \cdot \underline{\underline{\mathbf{T}}}_y^n - \partial_{xx}(uv)^n - \partial_{yy}v^2 - \partial_{zz}(vw)^n], \\
 H^n &= \Delta t[-M\nabla \cdot \underline{\underline{\Theta}}_z^n + (1/Re)\nabla \cdot \underline{\underline{\mathbf{T}}}_z^n - \partial_{xx}(uw)^n - \partial_{yy}(vw)^n - \partial_{zz}w^2].
 \end{aligned}$$

For an incompressible flow, the velocity satisfies the following condition

$$\begin{aligned}
 0 &= \partial_x u^n + \partial_y v^n + \partial_z w^n \\
 &= \partial_x F^n - \Delta t \partial_{xx} p^n - \partial_y G^n - \Delta t \partial_{yy} p^n - \partial_z H^n - \Delta t \partial_{zz} p^n.
 \end{aligned} \tag{3.19}$$

Eq. (3.19) is equivalent to

$$\partial_{xx} p^n + \partial_{yy} p^n + \partial_{zz} p^n = (\partial_x F^n + \partial_y G^n + \partial_z H^n) / \Delta t. \tag{3.20}$$

Successive over-relaxation (SOR) iteration method [57], which is a variant of the Gauss–Seidel method for solving a linear system of equations, is used to solve the Poisson equation Eq. (3.20). The convergence rate of the SOR iteration is significantly affected by the acceleration parameter, which is chosen to be 1.7 in this work [57]. The stopping tolerance for the pressure iteration is set to be 1×10^{-6} .

Thereafter, the components of the velocity u , v and w are updated as follows

$$\begin{aligned}
 u_{i,j,k}^{n+1} &= F^n - \Delta t \partial_x p, \\
 v_{i,j,k}^{n+1} &= G^n - \Delta t \partial_y p, \\
 w_{i,j,k}^{n+1} &= H^n - \Delta t \partial_z p.
 \end{aligned}$$

Components of the stress tensor for calculating $u_{i,j,k}$

$$\begin{aligned}\theta_{i+\frac{1}{2},j,k}^{xx} &= -\left(\frac{c_{i+2,j,k}-c_{i,j,k}}{2\Delta x}\right)^2 + \left(\frac{c_{i+1,j+1,k}-c_{i+1,j-1,k}}{2\Delta y}\right)^2 + \left(\frac{c_{i+1,j,k+1}-c_{i+1,j,k-1}}{2\Delta z}\right)^2 \\ \theta_{i-\frac{1}{2},j,k}^{xx} &= -\left(\frac{c_{i+1,j,k}-c_{i-1,j,k}}{2\Delta x}\right)^2 + \left(\frac{c_{i,j+1,k}-c_{i,j-1,k}}{2\Delta y}\right)^2 + \left(\frac{c_{i,j,k+1}-c_{i,j,k-1}}{2\Delta z}\right)^2 \\ \theta_{i,j+\frac{1}{2},k}^{yx} &= -2\left[\frac{(c_{i,j+1,k}+c_{i+1,j+1,k})-(c_{i+1,j,k}+c_{i,j,k})}{2\Delta y}\right]\left[\frac{(c_{i+1,j,k}+c_{i+1,j+1,k})-(c_{i,j,k}+c_{i,j+1,k})}{2\Delta x}\right] \\ \theta_{i,j-\frac{1}{2},k}^{yx} &= -2\left[\frac{(c_{i+1,j,k}+c_{i,j,k})-(c_{i+1,j-1,k}+c_{i,j-1,k})}{2\Delta y}\right]\left[\frac{(c_{i+1,j,k}+c_{i+1,j-1,k})-(c_{i,j,k}+c_{i,j-1,k})}{2\Delta x}\right] \\ \theta_{i,j,k+\frac{1}{2}}^{zx} &= -2\left[\frac{(c_{i,j,k+1}+c_{i+1,j,k+1})-(c_{i,j,k}+c_{i+1,j,k})}{2\Delta z}\right]\left[\frac{(c_{i+1,j,k}+c_{i+1,j,k+1})-(c_{i,j,k}+c_{i,j,k+1})}{2\Delta x}\right] \\ \theta_{i,j,k-\frac{1}{2}}^{zx} &= -2\left[\frac{(c_{i,j,k}+c_{i+1,j,k})-(c_{i,j,k-1}+c_{i+1,j,k-1})}{2\Delta z}\right]\left[\frac{(c_{i+1,j,k}+c_{i+1,j,k-1})-(c_{i,j,k}+c_{i,j,k-1})}{2\Delta x}\right]\end{aligned}$$

Components of the stress tensor for calculating $v_{i,j,k}$

$$\begin{aligned}\theta_{i+\frac{1}{2},j,k}^{xy} &= -2\left[\frac{(c_{i+1,j,k}+c_{i+1,j+1,k})-(c_{i,j,k}+c_{i,j+1,k})}{2\Delta x}\right]\left[\frac{(c_{i,j+1,k}+c_{i+1,j+1,k})-(c_{i,j,k}+c_{i+1,j,k})}{2\Delta y}\right] \\ \theta_{i-\frac{1}{2},j,k}^{xy} &= -2\left[\frac{(c_{i,j+1,k}+c_{i,j,k})-(c_{i-1,j+1,k}+c_{i-1,j,k})}{2\Delta x}\right]\left[\frac{(c_{i,j+1,k}+c_{i-1,j+1,k})-(c_{i,j,k}+c_{i-1,j,k})}{2\Delta y}\right] \\ \theta_{i,j+\frac{1}{2},k}^{yy} &= \left(\frac{c_{i+1,j+1,k}-c_{i-1,j+1,k}}{2\Delta x}\right)^2 - \left(\frac{c_{i,j+2,k}-c_{i,j,k}}{2\Delta y}\right)^2 + \left(\frac{c_{i,j+1,k+1}-c_{i,j+1,k-1}}{2\Delta z}\right)^2 \\ \theta_{i,j-\frac{1}{2},k}^{yy} &= \left(\frac{c_{i+1,j,k}-c_{i-1,j,k}}{2\Delta x}\right)^2 - \left(\frac{c_{i,j+1,k}-c_{i,j-1,k}}{2\Delta y}\right)^2 + \left(\frac{c_{i,j,k+1}-c_{i,j,k-1}}{2\Delta z}\right)^2 \\ \theta_{i,j,k+\frac{1}{2}}^{xy} &= -2\left[\frac{(c_{i,j,k+1}+c_{i,j+1,k+1})-c_{i,j,k}+c_{i,j+1,k}}{2\Delta z}\right]\left[\frac{(c_{i,j+1,k}+c_{i,j+1,k+1})-(c_{i,j,k}+c_{i,j,k+1})}{2\Delta y}\right] \\ \theta_{i,j,k-\frac{1}{2}}^{xy} &= -2\left[\frac{(c_{i,j,k}+c_{i,j+1,k})-(c_{i,j,k-1}+c_{i,j+1,k-1})}{2\Delta z}\right]\left[\frac{(c_{i,j+1,k-1}+c_{i,j+1,k})-(c_{i,j,k-1}+c_{i,j,k})}{2\Delta y}\right]\end{aligned}$$

Components of the stress tensor for calculating $w_{i,j,k}$

$$\begin{aligned}\theta_{i+\frac{1}{2},j,k}^{xz} &= -2\left[\frac{(c_{i+1,j,k}+c_{i+1,j,k+1})-(c_{i,j,k}+c_{i,j,k+1})}{2\Delta x}\right]\left[\frac{(c_{i,j,k+1}+c_{i+1,j,k+1})-(c_{i,j,k}+c_{i+1,j,k})}{2\Delta z}\right] \\ \theta_{i-\frac{1}{2},j,k}^{xz} &= -2\left[\frac{(c_{i,j,k}+c_{i,j,k+1})-(c_{i-1,j,k}+c_{i-1,j,k+1})}{2\Delta x}\right]\left[\frac{(c_{i-1,j,k+1}+c_{i,j,k+1})-(c_{i-1,j,k}+c_{i,j,k})}{2\Delta z}\right] \\ \theta_{i,j+\frac{1}{2},k}^{yz} &= -2\left[\frac{(c_{i,j+1,k}+c_{i,j+1,k+1})-(c_{i,j,k}+c_{i,j,k+1})}{2\Delta y}\right]\left[\frac{(c_{i,j,k+1}+c_{i,j+1,k+1})-(c_{i,j,k}+c_{i,j+1,k})}{2\Delta z}\right] \\ \theta_{i,j-\frac{1}{2},k}^{yz} &= -2\left[\frac{(c_{i,j,k}+c_{i,j,k+1})-(c_{i,j-1,k}+c_{i,j-1,k+1})}{2\Delta y}\right]\left[\frac{(c_{i,j-1,k+1}+c_{i,j,k+1})-(c_{i,j-1,k}+c_{i,j,k})}{2\Delta z}\right] \\ \theta_{i,j,k+\frac{1}{2}}^{zz} &= \left(\frac{c_{i+1,j,k+1}-c_{i-1,j,k+1}}{2\Delta x}\right)^2 + \left(\frac{c_{i,j+1,k+1}-c_{i,j-1,k+1}}{2\Delta y}\right)^2 - \left(\frac{c_{i,j,k+2}-c_{i,j,k}}{2\Delta z}\right)^2 \\ \theta_{i,j,k-\frac{1}{2}}^{zz} &= \left(\frac{c_{i+1,j,k}-c_{i-1,j,k}}{2\Delta x}\right)^2 + \left(\frac{c_{i,j+1,k}-c_{i,j-1,k}}{2\Delta y}\right)^2 - \left(\frac{c_{i,j,k+1}-c_{i,j,k-1}}{2\Delta z}\right)^2\end{aligned}$$

Table 3.2: Discretization for the components of capillary stress tensor.

The numerical stability for solving the Cahn-Hilliard model is ensured by a dynamic restriction for the time step [58]².

$$\Delta t < \Upsilon \min \left\{ \frac{1}{2} Re \left(\frac{1}{\Delta x^2} + \frac{1}{\Delta y^2} + \frac{1}{\Delta z^2} \right), \frac{\Delta x}{|u_{\max}|}, \frac{\Delta y}{|v_{\max}|}, \frac{\Delta z}{|w_{\max}|} \right\}, \quad (3.21)$$

²The stability criterion for the time step is discussed with M.S.

where Υ is a safety factor, and u_{\max} , v_{\max} and w_{\max} are the maximal velocities in the x , y and z directions, respectively.

3.4 Simulation system

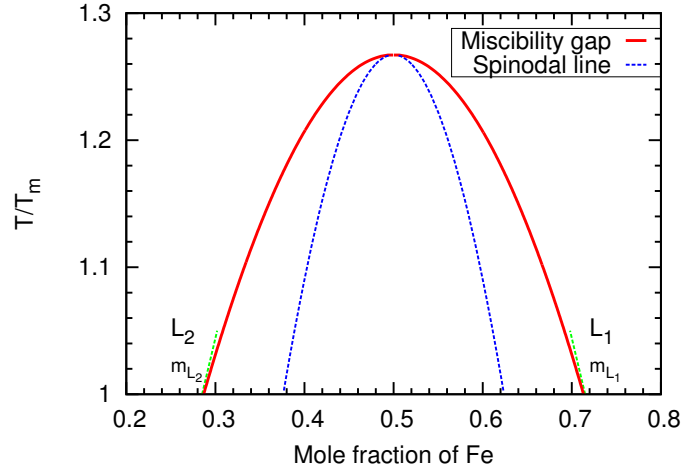


Figure 3.4: Miscibility gap of the Fe-Sn system: the red-solid line illustrates the equilibrium mole fraction of Fe in L_1 and L_2 phases and the blue-dashed line corresponds to the spinodal line.

For the Cahn-Hilliard-Navier-Stokes model, I take the binary alloy Fe-Sn as an exemplary system, since there are two immiscible liquids, namely the Fe-rich L_1 phase and the Sn-rich L_2 phase, in the phase diagram. The Gibbs free energy density of the Fe-Sn system is formulated as³

$$f(c, T) = R_g T / v_m [c \ln c + (1 - c) \ln(1 - c)] + \Omega_1 c(1 - c) + \Omega_2 c^2(1 - c)^2,$$

where Ω_1 and Ω_2 are constants which are used to map the miscibility gap of the Fe-Sn system. The thermodynamic equilibrium condition yields

$$\mu_1 := \partial_c f(c, T)|_{c=c_{L_1}^{eq}} = \partial_c f(c, T)|_{c=c_{L_2}^{eq}} =: \mu_2, \quad (3.22)$$

$$f(c, T)|_{c=c_{L_1}^{eq}} - \mu_1 c_{L_1}^{eq} = f(c, T)|_{c=c_{L_2}^{eq}} - \mu_2 c_{L_2}^{eq}, \quad (3.23)$$

where $c_{L_1}^{eq}$ and $c_{L_2}^{eq}$ denote the equilibrium mole fractions of Fe in L_1 and L_2 phases, respectively. Substituting the free energy density $f(c, T)$ into Eqs. (3.22) and (3.23) and solving the nonlinear system by the Newton method, we obtain the equilibrium mole fractions of Fe in L_1 and L_2 phases at different temperatures, as shown by the red line in Fig. 3.4⁴. The dashed blue line corresponds to the spinodal line which is given by the locus of $\partial_{cc} f = 0$.

³This equation is based on a discussion with A.C.

⁴A.C. helped for the reconstruction of the phase diagram.

Model II: The Allen-Cahn model

3.5 The multi-phase Allen-Cahn model

3.5.1 The Allen-Cahn model

As proposed in Ref. [51], the free energy functional of the system is written as

$$\mathcal{F}(\mathbf{c}, \boldsymbol{\phi}, T) = \int_V \left[\frac{1}{\epsilon} \omega(\boldsymbol{\phi}) + \epsilon a(\boldsymbol{\phi}, \nabla \boldsymbol{\phi}) \right] dx, \quad (3.24)$$

where $\boldsymbol{\phi} = (\phi_1, \phi_2, \dots, \phi_N)$, with N being the number of phases in the considered system. ϵ is a modeling parameter which is related to the interfacial width scaled by the characteristic length.

The first term in Eq. (3.24) is a potential energy, which is formulated as

$$\omega(\boldsymbol{\phi}) = \frac{16}{\pi^2} \sum_{\alpha}^N \sum_{\beta > \alpha} \gamma_{\alpha\beta} \phi_{\alpha} \phi_{\beta} + \frac{96}{\pi^2} \sum_{\alpha}^N \sum_{\beta > \alpha} \sum_{\delta > \beta} \gamma_{\alpha\beta\delta} \phi_{\alpha} \phi_{\beta} \phi_{\delta}, \quad (3.25)$$

where $\gamma_{\alpha\beta}$ are coefficients defining the surface energy of the α - β interface, and $\gamma_{\alpha\beta\delta}$ is a parameter which is used to avoid the appearance of artificial third phase along two phase boundaries.

The second term in Eq. (3.24) represents the gradient energy that is expressed as

$$a(\boldsymbol{\phi}, \nabla \boldsymbol{\phi}) = \sum_{\alpha}^N \sum_{\beta > \alpha} \gamma_{\alpha\beta} |\phi_{\alpha} \nabla \phi_{\beta} - \phi_{\beta} \nabla \phi_{\alpha}|^2.$$

The evolution of the order parameter $\boldsymbol{\phi}$ is to minimize the free energy functional and can be derived by the functional derivative

$$\tau_{\alpha\beta} \epsilon \frac{\partial \phi_{\alpha}}{\partial t} = - \frac{\delta \mathcal{F}}{\delta \phi_{\alpha}} - \chi, \quad \alpha = 1, \dots, N,$$

where $\tau_{\alpha\beta}$ is a relaxation coefficient for the α - β interface and χ is a Lagrange multiplier ensuring the constraint $\sum_{\alpha=1}^N \phi_{\alpha} = 1$.

With

$$\chi = - \frac{1}{N} \sum_{\alpha=1}^N \frac{\delta \mathcal{F}}{\delta \phi_{\alpha}} \text{ as well as } \frac{\delta}{\delta \phi_{\alpha}} = \frac{\partial}{\partial \phi_{\alpha}} - \nabla \cdot \frac{\partial}{\partial \nabla \phi_{\alpha}},$$

we obtain the evolution equation for each component ϕ_{α} of the phase-field order parameter

$$\tau_{\alpha\beta} \epsilon \frac{\partial \phi_{\alpha}}{\partial t} = \epsilon [\nabla \cdot a_{,\nabla \phi_{\alpha}}(\boldsymbol{\phi}, \nabla \boldsymbol{\phi}) - a_{,\phi_{\alpha}}(\boldsymbol{\phi}, \nabla \boldsymbol{\phi})] - \frac{1}{\epsilon} \omega_{,\phi_{\alpha}}(\boldsymbol{\phi}) - \chi.$$

3.5.2 Volume preservation technique

The Allen-Cahn model is used to corroborate the morphological stability criterion of jets. During the evolution of the perturbed jet, the volume of the considered jet is preserved. However, in the Allen-Cahn model, without external force, the volume of a cylinder shrinks with time because of the curvature force $\sigma\kappa$. To illustrate this point in a more clear manner, we show an example. For a curved fluid-fluid interface with mean curvature of κ in the stationary state, the pressure difference across the interface reads $\Delta p = \sigma\kappa$. This equation is known as the Young-Laplace equation, which shows a force balance of the pressure with the curvature force. If the pressure gradient is absent in the Allen-Cahn model, the curved liquid-liquid interface relaxes to be flat; for a sphere, the volume decreases with time till it vanishes. To overcome this shrinking effect, a volume preserved technique has been proposed by Nestler et al. [59].

The concept of the volume preservation technique is to add an additional bulk free energy density into the free energy functional in Eq. (3.24) of the form

$$g(\phi) = \sum_{\alpha=1}^A \chi_{\alpha} h(\phi_{\alpha}), \quad (3.26)$$

where the index A denotes the range of the volume conserved phases from $\alpha = 1, \dots, A$. For the non-conserved phases $\alpha = A + 1, \dots, N$, we set $\chi_{\alpha} = 0$. We note that when an additional bulk free energy density is added, the corresponding Lagrange multiplier

$$\Lambda = -\frac{1}{N} \sum_{\alpha=1}^N \chi_{\alpha} h_{,\phi_{\alpha}}(\phi_{\alpha}) \quad (3.27)$$

has to be added as well. With the straightforward A equations that the volumes of phases $\alpha = 1, \dots, A$ are preserved

$$0 = \int_V \partial_t \phi_{\alpha} dx, \quad (3.28)$$

the coefficients χ_{α} can be determined accordingly. The obtained results for χ_{α} are given in Ref. [59].

3.6 In accordance with the thermodynamical law

In this section, I demonstrate that both models satisfy the non-increasing free energy principle

$$\frac{d\mathcal{F}}{dt} \leq 0.$$

In the Cahn-Hilliard-Navier-Stokes model, the time derivative of the free energy functional can be expressed as

$$\frac{d\mathcal{F}}{dt} = \langle \delta\mathcal{F}/\delta c, d_t c \rangle. \quad (3.29)$$

For a constant mobility Λ , Eq. (3.29) is rewritten as

$$\begin{aligned} \frac{d\mathcal{F}}{dt} &= \langle \delta\mathcal{F}/\delta\phi, \Lambda\nabla^2\mu \rangle \\ &= \langle \mu, \Lambda\nabla^2\mu \rangle \\ &= \int_V \mu(\Lambda\nabla^2\mu)dx \\ &= \mu\mathbf{n} \cdot \Lambda\nabla\mu|_{\partial V} - \Lambda \int_V (\nabla\mu)^2 dx \\ &= -\Lambda \int_V (\nabla\mu)^2 dx \leq 0, \end{aligned}$$

where we have used integration by parts and no-flux boundary condition $\mathbf{n} \cdot \Lambda\nabla\mu|_{\partial V} = 0$. The demonstration for the non-increasing of the free energy functional in the Allen-Cahn model is as following

$$\frac{d\mathcal{F}}{dt} = (\delta\mathcal{F}/\delta\phi)\partial_t\phi = -\tau\epsilon(\delta\mathcal{F}/\delta\phi)^2 \leq 0.$$

Chapter 4

Corroboration of the Plateau-Rayleigh criterion

In this chapter, I validate the classic Plateau-Rayleigh criterion for tiny perturbations $a \ll R_0$ using the Cahn-Hilliard-Navier-Stokes model. I show that the simulated results for perturbations of finite amplitudes $a \in (0, R_0)$ significantly deviate from the Plateau-Rayleigh criterion as well as other existing work. The main part of this chapter was published in Ref. [60].

4.1 Simulation setup

I use a cubic simulation domain with a size of $N_x \times N_y \times N_z$ and with a uniform spatial step. An axisymmetrically perturbed jet, $R_0 + a \cos kz = \sqrt{(x - N_x/2)^2 + (y - N_y/2)^2}$ is initially placed in the middle of the simulation domain, whereat R_0 is fixed for all simulations and the amplitude is $a \in (0, R_0)$. I set $N_x = N_y = H \gg 2(R_0 + a)$ to avoid the boundary effects and use no outside flux boundary conditions in the x and y dimensions. In the longitudinal direction, the cube has a length of $N_z = \lambda$ and the periodic boundary conditions at $z = \pm\lambda/2$ model an infinite domain. The concentrations in the L_1 and L_2 phases are set to be the equilibrium values at the temperature of $T/T_m = 1$ given by the phase diagram shown in Fig. 3.4. The evolution of the interface follows the Cahn-Hilliard-Navier-Stokes equation. The parameters used for simulations are tabulated in Tab. 4.1.

Parameters	Descriptions	Value
κ_c (J/m)	Gradient energy coefficient	5×10^{-9}
$\Delta x = \Delta y = \Delta z$ (3D)	Discretization space step	d_0
Re	Reynolds number	0.01
$\Omega_1/(R_g T_m/v_m)$	Interaction coefficient	0.345
$\Omega_2/(R_g T_m/v_m)$	Interaction coefficient	4.379
d_0 (nm)	Capillary length	1
η (Pas)	Dynamic viscosity	1×10^{-3}
ρ (kg/m ³)	Density	1×10^4
D (m ² /s)	Diffusion coefficient	1×10^{-9}
$R_g T_m/v_m$ (J/m ³)	Scaling factor of free energy	1×10^9
T_m (K)	Monotectic temperature	1403
c_{l1}^0	Monotectic mole fraction of L_1	0.7132
c_{l2}^0	Monotectic mole fraction of L_2	0.2868

Table 4.1: Parameters used for simulations. This table is from Ref. [60].

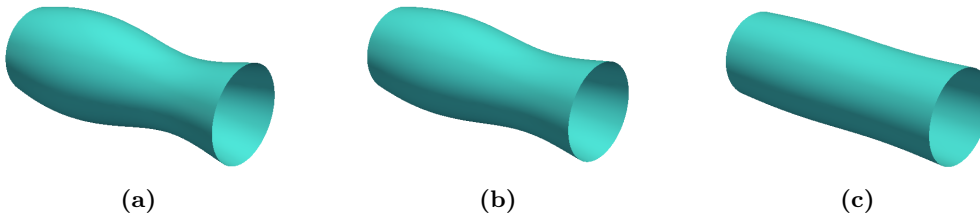


Figure 4.1: “Isosurface plots showing the morphological stabilization of the rod: (a) $tD/d_0^2 = 8.4$, (b) $tD/d_0^2 = 20.4$, and (c) $tD/d_0^2 = 68.4$. The geometric parameters are $\lambda/R_0 = 5.6$, $a/R_0 = 0.2$ and $H/R_0 = 8$.” [60]

4.2 Validation of the classic Plateau-Rayleigh criterion for tiny perturbations

“Fig. 4.1 (a)-(c)⁵ show the temporal evolution of the $L_1 - L_2$ interface, starting from a sinusoidal perturbation. Corresponding geometric parameters for the simulation are $\lambda/R_0 = 5.6$, $a/R_0 = 0.2$ and $H/R_0 = 8$. The difference in curvature along the interface gives rise to a concentration gradient along the interface due to the Gibbs-Thomson effect. The inhomogeneous interfacial concentration consequently induces the surface flow which is driven by the capillary force $\nabla \cdot [\kappa_c(\nabla c)^2 \mathbf{I} - 2\kappa_c \nabla c \otimes \nabla c]$. With time, the convex interface contracts towards the center of the cylinder and the concave interface bulges out, resulting in flattening of the interface.” [60]

⁵The figure is visualized by using the post-processing tool, which is developed by M.S.

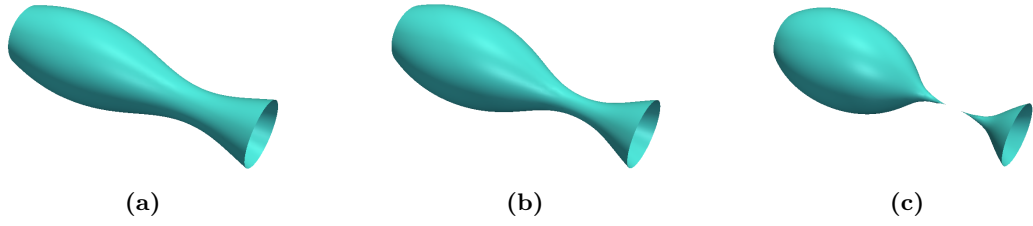


Figure 4.2: “Isosurface plots showing Marangoni instability for $\lambda/R_0 = 8$ at different times: (a) $tD/d_0^2 = 10$, (b) $tD/d_0^2 = 17$, and (c) $tD/d_0^2 = 20.8$.” [60]

“The time evolution of the $L_1 - L_2$ interface for a longer periodic length of $\lambda/R_0 = 8$ is shown in Fig. 4.2 (a)-(c)⁶. The interface grows at the crest and shrinks at the trough. Eventually, the rod breaks up and separates into isolated droplets.” [60]

“During the evolution, the $L_1 - L_2$ interface is obtained by the locus of $c = 0.5$. The interface as a function of time and space can be written in the following form

$$\begin{aligned} r(t, z) &= R_0 + a \exp(\omega t) \sin(2\pi z/\lambda) \\ &= R_0 + a\omega t \sin(2\pi z/\lambda) + \dots, \end{aligned} \quad (4.1)$$

where ω is the growth rate which is determined by a linear fit to the curve describing the amplitude of the interface as a function of time. Based on the linear stability description, the relation $\omega = \omega(\lambda/R_0)$ for $H/R_0 = 5.6$ is plotted in Fig. 4.3 (a) for three different dimensionless numbers $M = 10000, 20000$ and 50000 . It is observed that the critical wavelength is at⁷

$$(\lambda/R_0)_{\text{crit}} = 6.2 \approx 2\pi,$$

which is consistent with the PR criterion, Eq. (2.4). Above the ratio of $(\lambda/R_0)_{\text{crit}}$, the cylinder breaks up into separate droplets and below the critical ratio, the cylinder is morphologically stabilized. In the unstable region, the growth rate ω is positive and increases with the dimensionless number M . In the stable region, the growth rate is negative and the absolute value increases with M . This is because that the interfacial force is proportional to M , as shown in Eq. (3.18). Thus, the interface grows or shrinks faster for a higher value of M . Also, the critical ratio $(\lambda/R_0)_{\text{critical}}$ is independent on M . Fig. 4.3 (b) depicts the transition diagram for three different values of H/R_0 with the same value of $M = 50000$. The critical perturbation wavelength remains unchanged for different values of H/R_0 .” [60]

⁶The figure is visualized by using the post-processing tool, which is developed by M.S.

⁷R.M. suggested to fit the curve near the critical point in Fig. 4.3 (b).

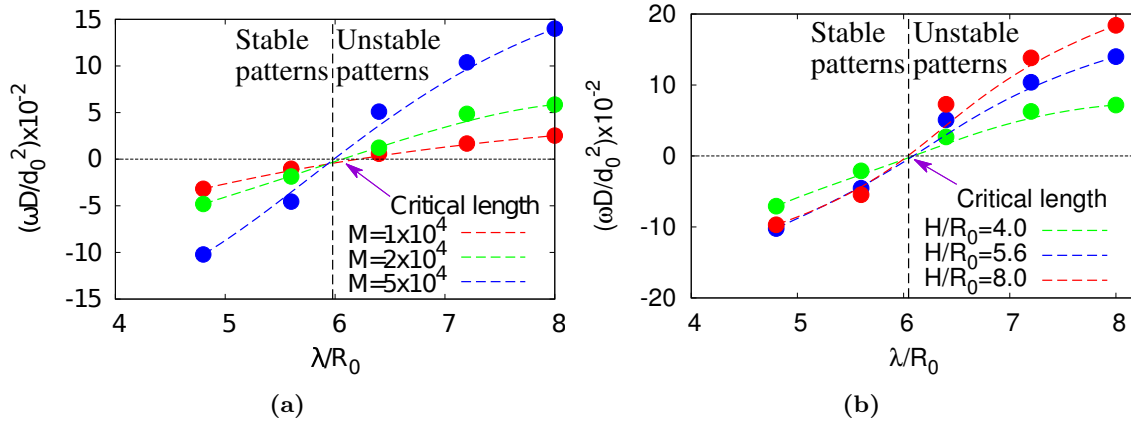


Figure 4.3: “Stability diagram: Stability to instability transition (a) for distinct values of M at a constant ratio of $H/R_0 = 5.6$ and (b) for different values of H/R_0 at a fixed $M = 50000$. The vertical dotted line distinguishes the stable from the unstable regions.” [60]

4.3 Significant deviations of the simulation results from the Plateau-Rayleigh criterion

In order to corroborate the mentioned criteria, Eqs. (2.4), (2.5), (2.10), and (2.21), I perform numerical experiments, based on the volume preserved Allen-Cahn (AC) and Cahn-Hilliard-Navier-Stokes (CHNS) models. Both approaches coincide with the second law of thermodynamics, so that the free energy continuously decreases in time. As mentioned in Ref. [61], the former one captures the mean curvature flow and the latter one models the surface diffusion/convection. The differences and similarities between the AC and CHNS models are summarized in Tab. 4.2. The simulation setup for both approaches is as in section 4.1.

Thermodynamical law	$d\mathcal{F}/dt \leq 0$	
Physical mechanisms	Mean curvature flow	Surface diffusion/convection
Normal velocity	$v_n = -M(\kappa - H)$	$v_n = B_s \nabla_s^2 \kappa$
Phase-field model	Allen-Cahn model	Cahn-Hilliard-Navier-Stokes model
Free energy functional	$\mathcal{F} = \int_{\Omega} [f(y) + \Gamma(\nabla y)^2] dx$	
Evolution equations	$\partial_t y = -M_1 \delta \mathcal{F} / \delta y - H$	$\begin{aligned} \partial_t y &= -\nabla \cdot \mathbf{J} \\ \mathbf{J} &= -M_2 \nabla (\delta \mathcal{F} / \delta y) + y \mathbf{u} \\ \rho (\partial_t \mathbf{u} + \mathbf{u} \cdot \nabla \mathbf{u}) &= -\nabla p + \nabla \cdot (\underline{\underline{\Theta}} + \underline{\underline{T}}) \\ \nabla \cdot \mathbf{u} &= 0 \end{aligned}$
<p>y is the order parameter, Γ is the gradient energy coefficient, M, B_s, M_1 and M_2 are positive constants, H is a Lagrange multiplier ensuring the constant-volume, \mathbf{J} is the flux, \mathbf{u} is the convection velocity, ρ is the density, p is the pressure, $\underline{\underline{\Theta}}$ and $\underline{\underline{T}}$ are the capillary and viscous stress tensors, respectively.</p>		

Table 4.2: Comparison between the AC and CHNS models.

For different amplitudes a , I vary the wavelength λ and run the corresponding simulations to find out the critical wavelength $\lambda_{AC}^{\text{crit}}$ for the AC model and $\lambda_{CH}^{\text{crit}}$ for the CHNS method. For the three-dimensional computation, the CHNS model (fourth order non-linear partial differential equation) requires much more computational effort than the AC model (second order non-linear partial differential equation). Due to this fact, the number of the numerical experimental data points from the CHNS model is less than the AC model.

The relative deviation of the simulation results from the mentioned criteria, as a function of the normalized amplitude $\alpha := a/R_0$, is illustrated in Fig. 4.4. The discrepancies of the numerical experimental results of the AC model from the classic PR criteria λ_1^{crit} and λ_2^{crit} reach as high as 40% and 60%, respectively. The corresponding maximum deviations from the work of Carter et al. and Nayfeh are 20% and 30%, respectively. The simulation results from the CHNS model show a similar convergence behavior as the AC model.

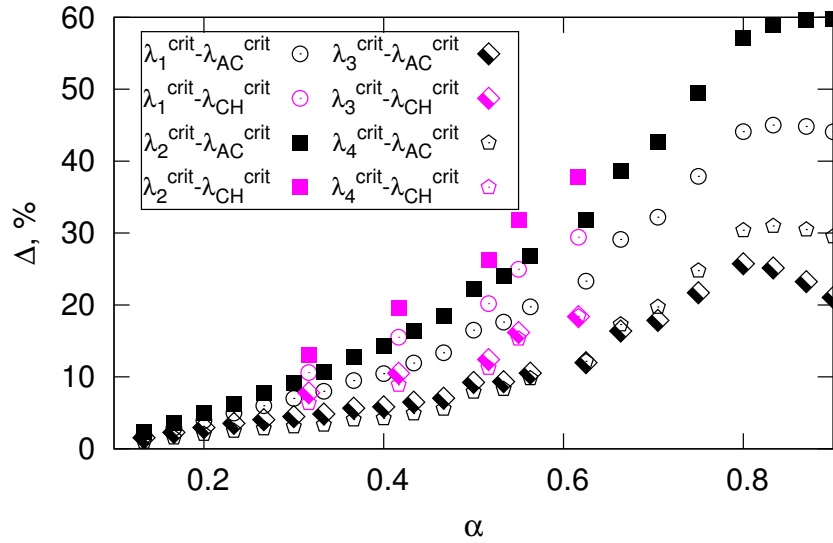


Figure 4.4: Relative deviation of the numerical experimental results from the existing criteria, Eqs. (2.4), (2.5), (2.10), and (2.21).

4.4 The problems for the stability criterion in literature

As mentioned, the volumes at the initial and perturbed states are not the same in the original PR criterion. This drawback prevents it from practical applications. Although the problem of non-consistency volume has been corrected, the amended PR criterion is only valid for tiny perturbations $a \ll R_0$.

Second and higher order stability analyses [5] show that the perturbation does not remain harmonic with time. Thus, the evolution of the jet generally does not follow the energy

trajectory shown in Fig. 2.4 and the results of Carter-Glaeser cannot be used to judge the morphological stability of jets.

The result of Nichols and Mullins is as the same as the original PR criterion and evidently, the volume is not conserved as well. The linear and second order stability analyses, which are carried out by Nichols et al. [3] and Nayfeh [5], respectively, show an improvement for the PR criterion. The problem is that the second order or even higher n -th order stability analyses have a residual error $\mathcal{O}(\alpha^{n+1})$ and their validity is confined to small values of α .

Chapter 5

A generalized morphological stability criterion for liquid jets

As shown in the previous chapter, a serious disagreement between the numerical experiment results and existing criteria is observed. This significant deviation reveals an incompleteness of the PR criterion. Motivated by the observed serious deviation as well as the mentioned limitations of existing criteria, I aim to derive a generalized stability criterion in the present chapter. This new criterion is obtained based on two independent methods: (i) surface energy minimization concept and (ii) analyzing the dynamic equations. An exemplary application of the criterion to the detachment of nanowires is discussed. Parts of this chapter were published in Ref. [62].

5.1 A general surface energy minimization concept

I start to derive a generalized morphological stability criterion from the energy principle that the free energy must be non-increasing in time. Nonlinear stability analyses [5, 63] show that the initial wave does not remain harmonic with time. Generally, the temporal change of the perturbations can be expressed in a Fourier series because of the periodicity in the longitudinal direction. Regarding the axisymmetry of the system, all sinusoidal contributions in the Fourier series vanish and the series is expressed as:

$$r(t, z) = R_0(t) + a_1(t) \cos kz + a_2(t) \cos 2kz + \dots . \quad (5.1)$$

In contrast to the only consideration of the leading order term a_1 in the classical works [1, 2, 4], I approximate the temporal perturbation till the second order. According to the surface integral

$$E_p(a_1, a_2) = \sigma \iint dA = 2\pi\sigma \int_{-\lambda/2}^{\lambda/2} r \sqrt{1 + (dr/dz)^2} dz, \quad (5.2)$$

we calculate the surface energy with the isotropic surface tension σ for all possible amplitudes a_1 and a_2 .

To properly compute the surface energy, Eq. (5.2), is the essential step for the energy minimization concept. In the following, we show the technical details to evaluate the integration in Eq. (5.2):

- (i) Firstly, the volumes of the unperturbed and perturbed jets must be the same. The volume of the perturbed jet is expressed as

$$V = \int_{-\lambda/2}^{\lambda/2} \pi r^2 dz = \pi \lambda \left[R_0^2(t) + \frac{1}{2} \sum_{n=1}^{\infty} a_n^2(t) \right]. \quad (5.3)$$

For the computation, we assume an unperturbed jet with uniform radius R_u , which has a volume of $\pi R_u^2 \lambda$. In comparison with Eq. (5.3), we have

$$R_u^2 = R_0^2(t) + \frac{1}{2} \sum_{n=1}^{\infty} a_n^2(t). \quad (5.4)$$

In the original work of Rayleigh, he compares the surface energy of a perturbed jet $R = R_0 + a \cos kz$ with a jet of uniform radius R_0 . It is noted that these two states do not have the same volume, namely, $\int_{-\lambda/2}^{\lambda/2} \pi (R_0 + a \cos kz)^2 dz = \pi (R_0^2 + \frac{1}{2} a^2) \lambda \neq \pi R_0^2 \lambda$.

- (ii) Secondly, we note that the leading order amplitude a_1 ranges from 0 to R_0 . With Eq. (5.4): $R_u^2 = R_0^2 + \frac{1}{2} a_1^2 = a_1^2 + \frac{1}{2} a_1^2$, we obtain an upper bound $a_1^m = \sqrt{(2/3)} R_u$ for a_1 .
- (iii) Thirdly, due to the axisymmetry, the crest of the wave perturbation remains convex with time. The convexity condition is mathematically defined as $\partial^2 R / \partial z^2|_{z=0} \leq 0, \forall t$. Substituting Eq. (5.1) into the inequality, we have $a_2 \geq -a_1/4 =: a_2^m$.

With the mentioned points (i)-(iii), we integrate Eq. (5.2) for all possible amplitudes $0 < a_1 < a_1^m$ and $a_2 > -a_1/4$. The required parameters for the integration are the volume V , wavelength λ , radius R_u , amplitudes a_1^m and a_2^m , and R_0 . For given volume V and wavelength λ , we obtain the radius R_u , according to $V = \pi R_u^2 \lambda$, as $R_u = \sqrt{V/(\pi \lambda)}$, and $a_1^m = \sqrt{(2/3)} R_u$ and $a_2^m = -a_1^m/4$. We apply the mass/volume conservation $R_0 = \sqrt{R_u^2 - \frac{1}{2}(a_1^2 + a_2^2)}$ (see Eq. (5.4)) to obtain the unknown R_0 .

For $V = 1$ and $\lambda = 2$, the difference $\Delta E := E_p - E_u$ of the surface energies for the perturbed $E_p(a_1, a_2)$ and unperturbed $E_u = (2\pi R_u \lambda) \sigma$ jets is plotted in Fig. 5.1. The energy isolines (the dashed lines) of $\Delta E = \Delta E(a_1^s, a_2^s)$ crosses at the saddle point (a_1^s, a_2^s) (the black ball) and divide the exemplary contour plot into four quadrants: A_u , A_s , M_1 and M_2 . For every geometric setup in A_u and A_s , the continuously decreasing of the

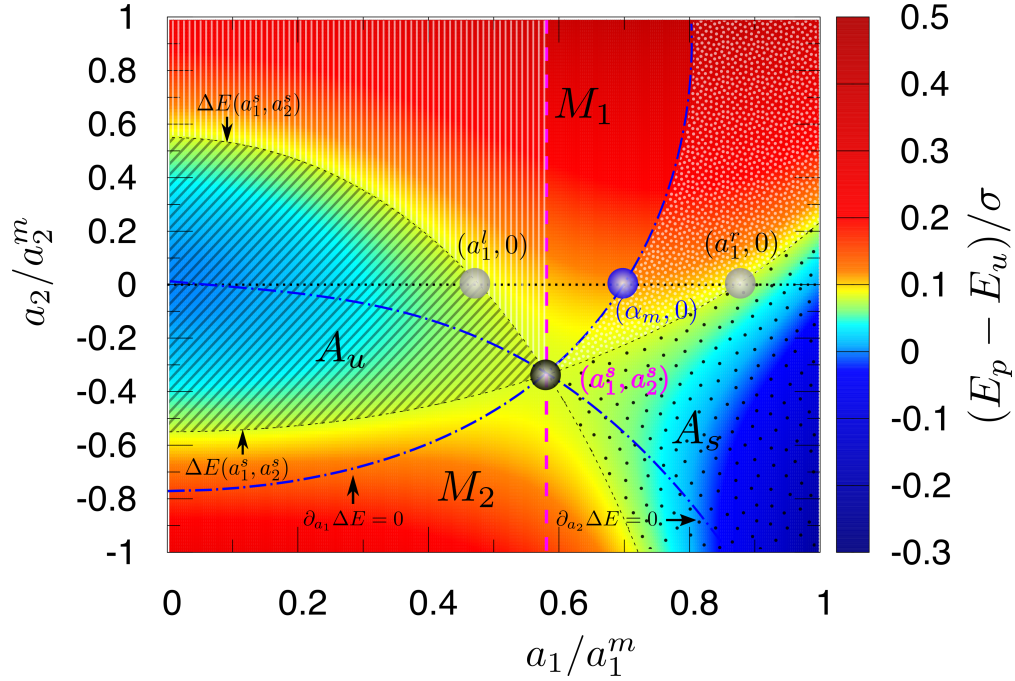


Figure 5.1: Contour plot for the difference of the surface energy $\Delta E := E_p - E_u$ as a function of a_1 and a_2 for a jet of $r = R_0 + a_1 \cos kx + a_2 \cos 2kx$. The volume and wavelength are set to be $V = 1$ and $\lambda = 2$.

free energy implies the temporal remaining of the amplitudes inside the corresponding domains and the convergence state is a jet and a chain of spheres, respectively. The end-state can be both for perturbations in M_1 and M_2 , which are named as metastable regions.

Considering the classical initial setup $a_2 = 0$ (the horizontal dotted line), the leading order amplitude a_1 is located in the metastable domain M_1 and we obtain a metastable interval $a_1 \in [a_1^l, a_1^r]$. For a jet with the initial amplitude a_1 inside this segment, the final state is ambiguous, either a uniform-radius jet or a chain of spheres.

The energy concept assumes only non-increasing surface energy in time, but does not consider the actual evolution. In order to determine the critical configuration more precisely, we refer to the corresponding evolution equations for different morphological changing mechanisms. In the considered models, the evolution equations are written in terms of the surface velocity. Knowing the distribution of the velocities on the surface, the resulting volume redistribution can be qualitatively estimated.

5.2 Physical mechanisms for spheroidization

A first mechanism for the spheroidization is surface diffusion/convection. When the jet is axisymmetrically perturbed by a wave in the radial direction, the diffusion potential is inhomogeneous along the surface due to the non-uniformity of the curvature κ . The

diffusion potential correlates to the curvature as [65]

$$\Phi = \mu_0 + \sigma\Omega\kappa, \quad (5.5)$$

where μ_0 is the potential of a reference state, σ is the isotropic interfacial energy, Ω is the atomic volume. For solid rods, the morphological change is driven by the surface diffusion flux $-\nabla\Phi$. For liquid rods, the surface flux contains two contributions: one from the surface diffusion and the other from the convection resulting from the momentum conservation law. In both cases, the morphological evolution is induced by the capillary force.

A second mechanism for the spheroidization is the mean curvature flow, which is a sort of geometric flow, and which is directly caused by the inhomogeneity of the mean curvature. The difference and similarity between the mean curvature flow and surface diffusion are that (i) the mean curvature flow usually does not conserve the volume, whereas the surface diffusion behaves in a conserved manner, (ii) the dynamics paths for the surface area minimization are different, and (iii) for nearly planar surface, the evolution equation of the mean curvature flow reduces to the diffusion equation. In present work, we refer to the volume preserved mean curvature flow, which is alternatively termed as surface tension flow.

5.3 Derivation for the generalized morphological stability criterion

The evolution equations for the processes driven by surface diffusion and mean curvature flow are expressed as [64–66]

$$v_n := \partial_t n = \begin{cases} -M\kappa, & \text{Mean curvature flow,} \\ B_s \nabla_s^2 \kappa, & \text{Surface diffusion/convection,} \end{cases}$$

where v_n is the normal velocity of the interface, M and B_s are positive constants. The mean curvature κ is defined as $\kappa := (\kappa_1 + \kappa_2)/2$, where κ_1 and κ_2 are the principal curvatures, and are mathematically calculated as

$$\begin{bmatrix} \Pi_u(\mathbf{e}_1, \mathbf{e}_1) & \Pi_u(\mathbf{e}_1, \mathbf{e}_2) \\ \Pi_u(\mathbf{e}_2, \mathbf{e}_1) & \Pi_u(\mathbf{e}_2, \mathbf{e}_2) \end{bmatrix} = \begin{bmatrix} \kappa_1 & 0 \\ 0 & \kappa_2 \end{bmatrix}.$$

Here, $\Pi_u(\mathbf{e}_1, \mathbf{e}_2) := \langle L_u(\mathbf{e}_1), \mathbf{e}_2 \rangle$ and $L_u(\mathbf{e}_i) := -\frac{\partial n}{\partial \mathbf{e}_i}$, where L_u is the Weingarten mapping [67], \mathbf{e}_1 and \mathbf{e}_2 are orthogonal unit vectors in the tangential space of the considered graph S , and \mathbf{n} is the normal vector. Further tedious calculation yields that the mean

curvature only depends on the longitudinal variable z

$$\kappa(z) = \frac{1}{2} \left\{ \underbrace{\frac{1/[R_0 + a \cos(2\pi z/\lambda)]}{[1 + (2a\pi/\lambda)^2 \sin^2(2\pi z/\lambda)]^{1/2}}}_{\text{radial curvature } \kappa_1} + \underbrace{\frac{a(2\pi/\lambda)^2 \cos(2\pi z/\lambda)}{[1 + (2a\pi/\lambda)^2 \sin^2(2\pi z/\lambda)]^{3/2}}}_{\text{longitudinal curvature } \kappa_2} \right\}.$$

For a wave perturbation, the mean curvature at the crest and trough is $1/(R_0 + a) + a(2\pi/\lambda)^2$ and $1/(R_0 - a) - a(2\pi/\lambda)^2$, respectively, where $\pm a(2\pi/\lambda)^2$ are the curvatures as in two dimensions and $1/(R_0 \pm a)$ are the contributions from the third-dimension. The normal velocity at the crest is inward since the mean curvature at this position is a summation of two positive values. Depending on the mean curvature at the trough, we come across three scenarios, as shown in Fig. 5.2 and summarized in the following:

- Scenario (a): For tiny perturbations, the curvature at the trough is dominated by the term $-ak^2$, resulting in an outward velocity, as depicted in Fig. 5.2 (a). Thereafter, the net volume flux appears from the crest to the trough, which finally leads to a uniform jet.
- By increasing amplitude, the mean curvature at the trough becomes positive and the velocity is inward, as shown in Fig. 5.2 (b). In spite of the fact that both velocities are inward, the volume flux at the crest is higher than the one at the trough, because of different shrinkage rates v_n . Thereafter, the volume redistribution leads also to a uniform jet.
- Scenario (c): With a further increase of the amplitude, the curvature at the trough is dominated by the radial curvature $1/(R_0 - a) > 1/(R_0 + a)$, as illustrated in Fig. 5.2 (c), and the normal velocity at this position exceeds the one at the crest. Thus, the trough shrinks faster than the crest, so that the net volume flux operates from the trough to the crest, eventually giving rise to spheroidization.

Accordingly, the critical configuration for the morphological stabilization is therefore given by the condition of $v_n|_{\text{crest}} = v_n|_{\text{trough}}$, or $\kappa|_{\text{crest}} = \kappa|_{\text{trough}}$, which yields the new criterion

$$\lambda_{\text{crit}} = 2\pi \sqrt{R_0^2 - a^2}. \quad (5.6)$$

For the surface diffusion process, the critical configuration is obtained by comparing the surface Laplace of the mean curvatures: $\nabla_s^2 \kappa|_{\text{crest}} = \nabla_s^2 \kappa|_{\text{trough}}$, which surprisingly gives rise to an identical criterion, as in Eq. (5.6). The evaluation of the surface Laplacian is provided in Appendix B.

The new criterion can be interpreted in such a way that there is either a critical wavelength λ_{crit} for a fixed amplitude a or a critical amplitude $a_{\text{crit}} = 2\pi R_0 \sqrt{1 - (\lambda/2\pi R_0)^2}$ for a fixed wavelength λ . In contrast to the classical PR theory, a finite water column can separate into a string of droplets, as long as the amplitude is sufficient large.

5.4 Comparison of the present stability criterion with existing criteria and with the simulation results

Fig. 5.3 shows the normalized critical wavelength $\lambda_{\text{crit}}/(2\pi R_u)$ as a function of the scaled perturbation amplitude $\alpha := a/R_0$. The shading region in gray color is the metastable region arising from the energy minimum concept, which is described in section 5.1. The upper and lower borders of the shading region correspond to α_1^l and α_m , respectively. The present criterion can be reformulated as

$$\lambda_{\text{crit}}/(2\pi R_u) = \sqrt{\frac{1 - (a/R_0)^2}{1 - \frac{1}{2}(a/R_0)^2}}, \quad (5.7)$$

using the volume constraint condition, and is illustrated by the red solid line. The simulation results from the AC and CHNS models are illustrated by the blue solid squares and the magenta diamonds, respectively. The criteria of existing theories are depicted by other lines/symbols.

Among all the existing theories for $\alpha \in [0, 1]$, only the result of Carter and Glaeser, the work of Nayfeh as well as the present work obey the energy minimum principle, which is based on the second order approximation. We emphasize that the present criterion, Eq. (5.6) is in good agreement with each previous criterion in their corresponding validity range. For $a \ll R_0$, the present criterion reduces to the PR criteria, $\lambda^{\text{crit}} \approx \lambda_1^{\text{crit}}, \lambda_2^{\text{crit}}$.

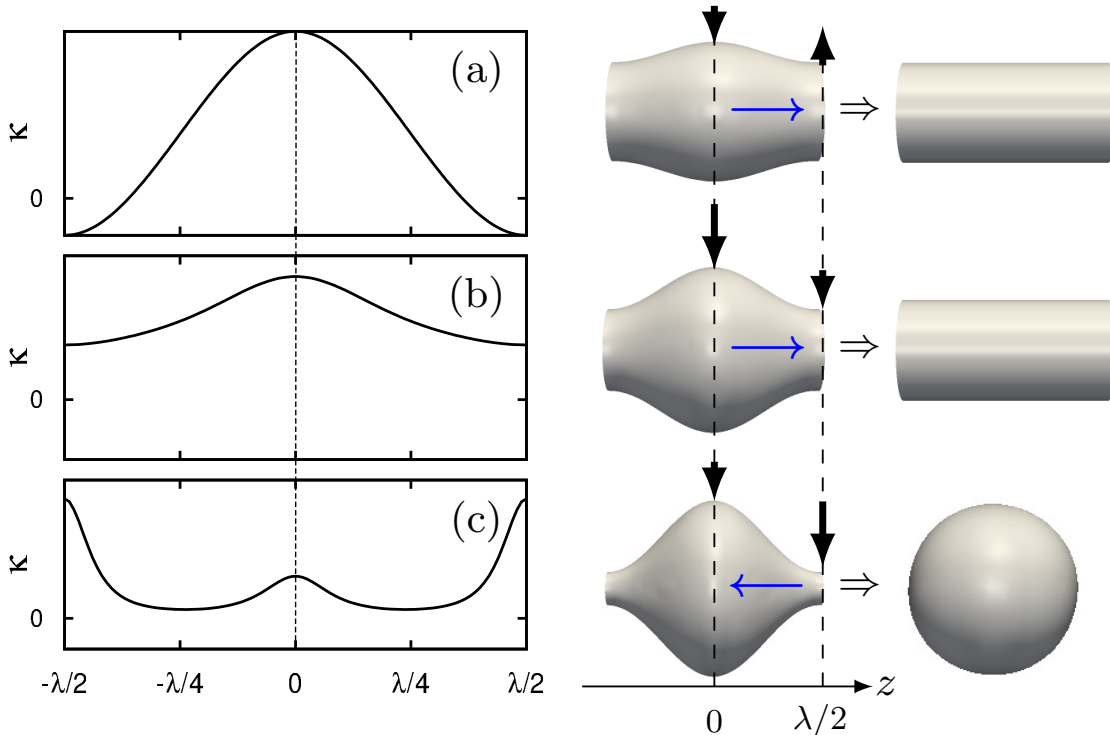


Figure 5.2: Illustration for the evolution of the rod for (a) tiny, (b) medium, and (c) large perturbations due to mean curvature flow.

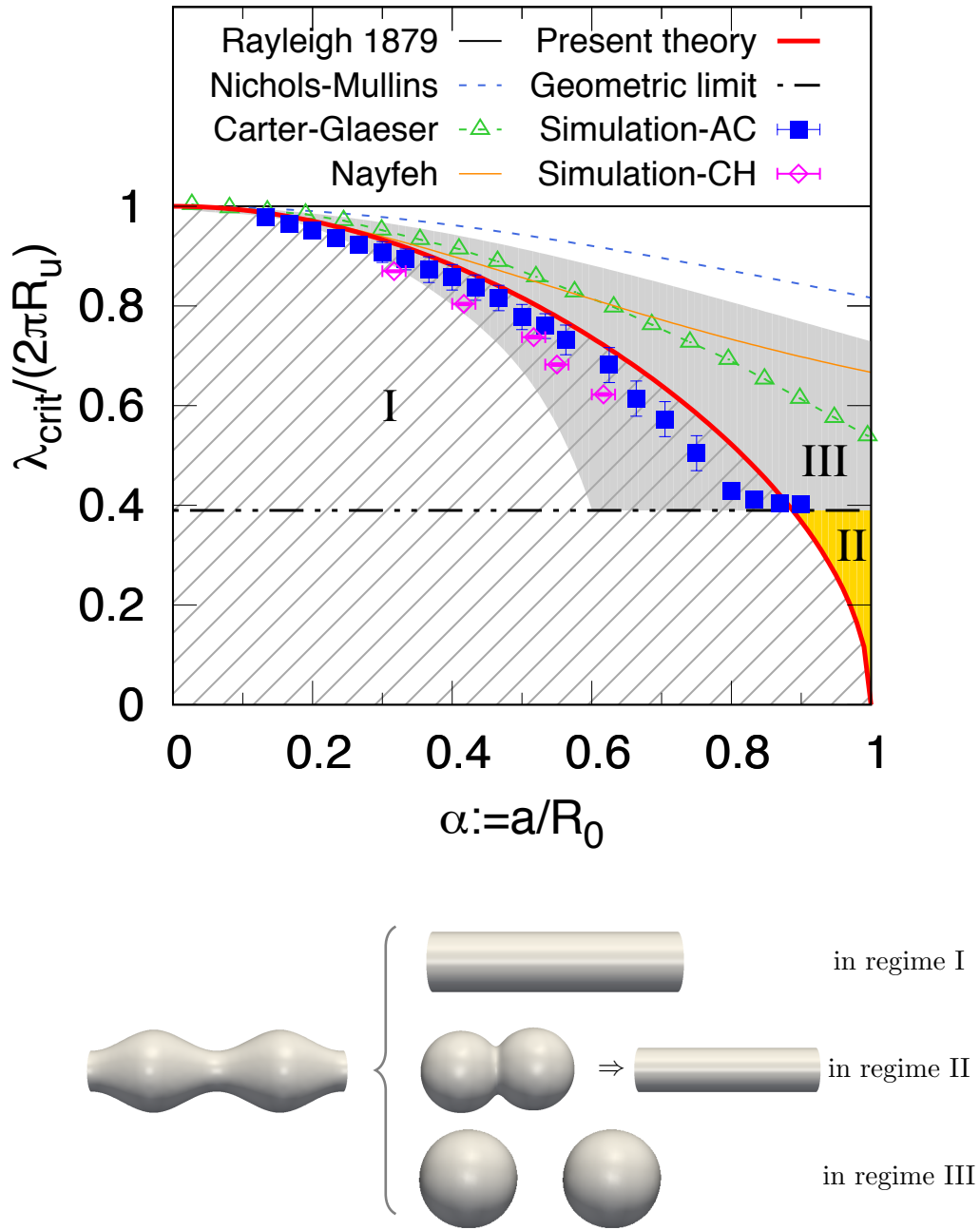


Figure 5.3: Stability diagram: the normalized critical wavelength $\lambda_{\text{crit}}/(2\pi R_u)$ as a function of the scaled perturbation amplitude $\alpha := a/R_0$.

Furthermore, the present work is well consistent with the second order stability analysis, $\lambda^{\text{crit}} - \lambda_4^{\text{crit}} = \mathcal{O}(\alpha^3)$ as well as with Carter's result, $\lambda^{\text{crit}} \approx \lambda_3^{\text{crit}}$ for $\alpha \lesssim 0.3$. For higher values of α , existing criteria significantly deviate from the present work. Moreover, we observe a satisfactory match between the numerical experimental results and the theory, in sharp contrast to the dramatic deviation in Fig. 4.4.

Paying careful attention to the fact that the diameter of the spheres cannot exceed the wavelength of the wave results in a lower geometric limit for the critical wavelength

$\lambda_{\text{crit}} = \sqrt{6}R_u$ or $\lambda_{\text{crit}}/(2\pi R_u) = \sqrt{6}/(2\pi)$, as shown by the dot-dashed line. The geometric constraint lies below all the critical wavelengths in literature and thus does not play a vital role for the morphological evolution. However, with the present criterion, the geometric limit crosses at $\alpha' = \sqrt{\frac{4\pi^2-6}{4\pi^2+3}} \approx 0.88777$ and we accordingly divide the stability diagram into three regimes:

- Regime I (filled with hatched lines): $0 \leq \alpha \leq 1$ and $\lambda < \lambda_{\text{crit}}$, the mean curvature at the crest is greater than the one at the trough. The surface flux is from the convex to the concave regions. The perturbed rod is morphologically stable.
- Regime II (filled with gold color): $\alpha' \leq \alpha \leq 1$ and $\lambda_{\text{crit}} \leq \lambda \leq \sqrt{6}R_u$, the perturbed rod first breaks up into separate particles due to the surface flux from the trough to the crest. After the breakup, the interfaces of the particles overlap with each other and the final state is a rod of uniform radius due to coalescence. The transition from rod to sphere and again to rod has not been tabulated in literature, but is observed in our numerical experiments, as shown in Fig. 5.4.
- Regime III (excluding I and II): $0 \leq \alpha \leq 1$, $\lambda \geq \lambda_{\text{crit}}$ and $\lambda \geq \sqrt{6}R_u$, the rod is morphologically unstable due to the surface flux from the trough to the crest and the final state is a line of spheres.

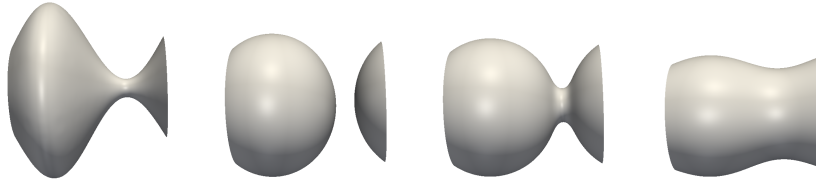


Figure 5.4: Transition from a rod to non-spherical particles and again to a rod.

We note that, according to the derivation of Rayleigh [2], there is a wavelength $\lambda_m = \sqrt{2}\lambda_{\text{crit}} = 2\sqrt{2}\pi R_u$, where the breakup of the rods has the maximum velocity. The derivation of this wavelength is based on the Lagrange's method using the potential energy of Eq. (2.6) and kinetic energy K of inviscid fluid to derive the dispersion relation $\omega = \omega(k)$ with $\frac{d}{dt}\left(\frac{\partial L}{\partial(\partial a/\partial t)}\right) = \frac{\partial L}{\partial a}$, where $L = K - E$. The wavelength λ_m corresponds to the growth rate ω having the maximum value. It is obvious that the calculation of the potential energy E (the surface energy) in the work of Rayleigh is based on the approximation of the first order term of the binomial series. Therefore the wavelength λ_m has to be amended for the general case of finite amplitude, which is the objective of a forthcoming work. The consideration of non-inviscid fluid may change the value of λ_m as well.

5.5 An application to the detachment of nanowires

“Metallic and semiconductor nanowires play essential roles in nanoelectronics, optoelectronics, sensorics, and numerous other fields. Thermal annealing is often applied on nanowires as a post-fabrication treatment to achieve desired physical properties. During the thermal annealing process or even at room temperature, nanowires may fragment into a chain of nanospheres, which prevents it from applications. Also, nanospheres are purposely produced from nanowires in microelectronic industry where the grain size affects the electrical resistance and is hence of significant relevance.” [62]

“As shown in Fig. 5.5 (a), the atoms of a planar interface of nanowire-environment are regularly ordered along the interface and therefore, the chemical potentials for atoms and vacancies are both uniformly distributed, establishing the thermodynamic equilibrium between the nanowire and environment. While the interface is stirred by a sinusoidal function, the potential energies along the interface of the nanowire are inhomogeneous because of non-uniformly distributed mean curvature. With contributions from the mean curvature, the diffusion potential energy is as shown in Eq. 5.5. For instance, in two dimensions, the diffusion potentials at $\lambda/4$ and $3\lambda/4$ are $\Phi_{\lambda/4} = \mu_A^0 + \gamma\Omega|\kappa|$ and $\Phi_{3\lambda/4} = \mu_A^0 - \gamma\Omega|\kappa|$, respectively (see Fig. 5.5 (b)). The gradient of the diffusion potential energy $-\nabla\Phi \propto 2\gamma\Omega\nabla\kappa$ in turn induces a surface flux from $\lambda/4$ to $3\lambda/4$, as schematically sketched in Fig. 5.5 (c), smoothing the nanowire.” [62]

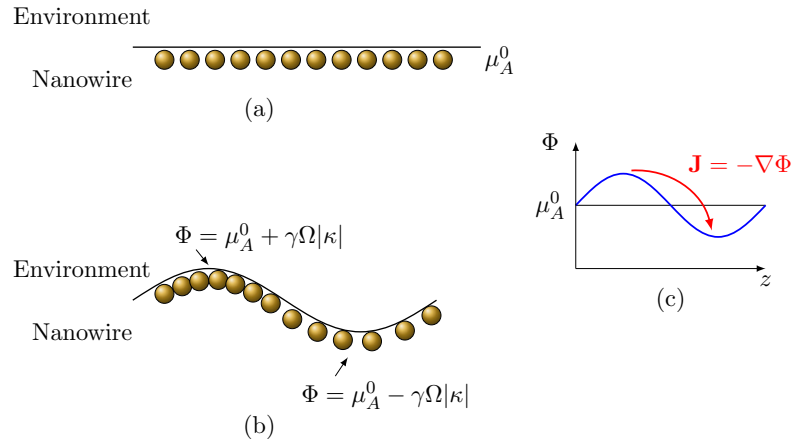


Figure 5.5: “Schematic illustration for chemical potential distribution affected by curvature: (a) The chemical potential is uniformly distributed for a planar interface. (b) The chemical potential along the interface of the nanowire is inhomogeneous because of perturbations. (c) A surface flux is induced by the gradient of diffusion potential Φ .” [62]

“The distribution of the mean curvature in the longitudinal direction z is illustrated in Fig. 5.6 (a) for different perturbation amplitudes. The corresponding geometric setting is $\lambda/d_0 = 160$ and $R_0/d_0 = 30$, where d_0 is the capillary length. For small amplitudes, e.g., $a/d_0 = 5$, the mean curvature decreases monotonically from $\lambda/4$ to $3\lambda/4$, as shown by the red solid line. In this case, the potential energy Φ at $\lambda/4$ is greater than the one at

$3\lambda/4$, since $\kappa_{\lambda/4} > \kappa_{3\lambda/4}$. The difference in the diffusion potential Φ consequently induces a surface flux \mathbf{J}_1 from $\lambda/4$ to $3\lambda/4$, as sketched in Fig. 5.6 (b). The subsequent effect is that the interface contracts towards the center of the nanowire at $\lambda/4$ and bulges out at $3\lambda/4$. The nanowire evolves till the interface becomes flat and the respective diffusion potential Φ is uniformly distributed along the interface. This monotonic decrease of the mean curvature from $\lambda/4$ to $3\lambda/4$ is comparable to the situation in two-dimensions. With an increase of the amplitude, extrema of the mean curvature occur between $\lambda/4$

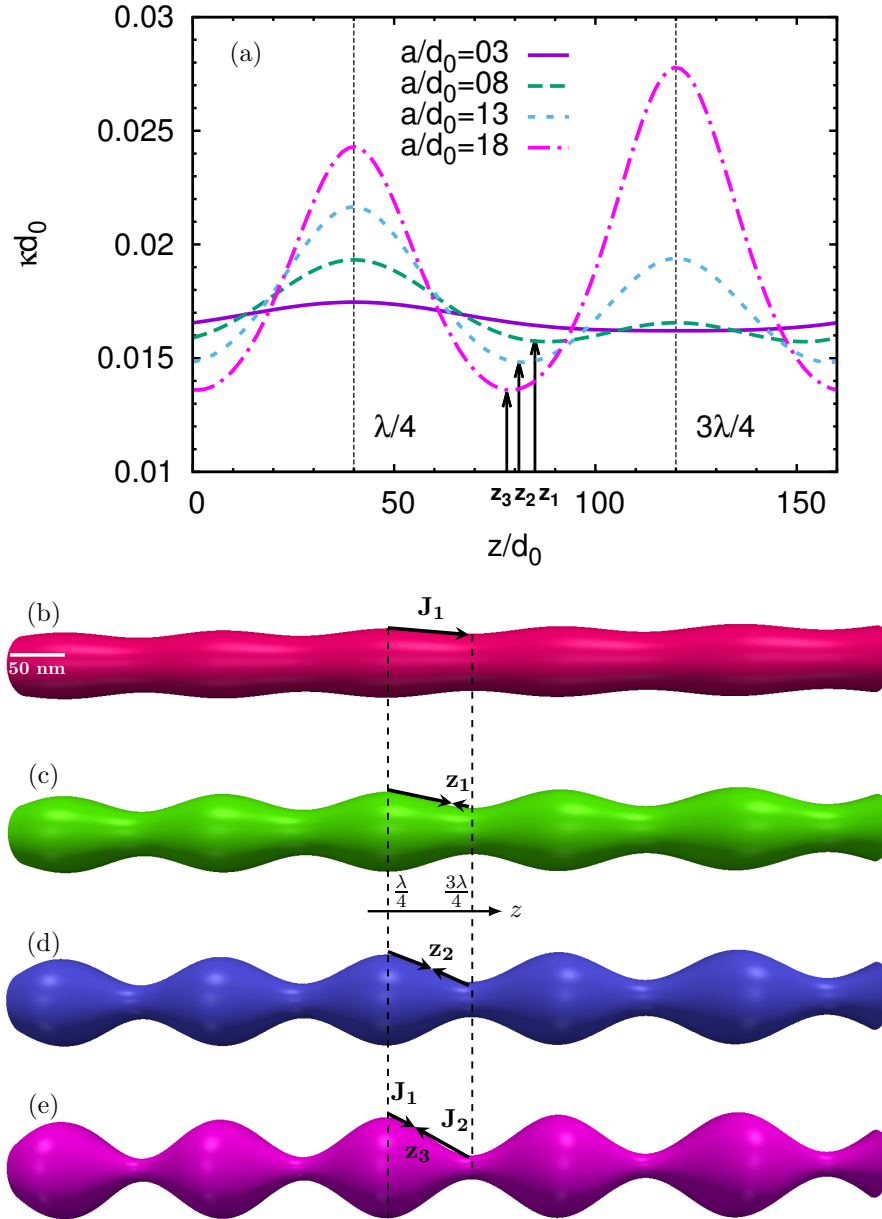


Figure 5.6: “Effect of curvature distribution on the surface flux for stirred nanowires: (a) mean curvature as a function of the spatial variable in the longitudinal direction for different perturbation amplitudes. (b), (c), (d), and (e) schematic drawings of the directions of the surface fluxes for perturbations with amplitudes $a/d_0 = 5, 8, 13, 18$, which correspond to the red, green, blue and magenta lines in (a), respectively.” [62]

and $3\lambda/4$, as illustrated by the green, blue and magenta lines in Fig. 5.6 (a). The locations of the curvature extrema for $a/d_0 = 8, 13$ and 18 are denoted by z_1, z_2 and z_3 , respectively. The corresponding potential energies Φ at $\lambda/4$ and $3\lambda/4$ are both greater than the ones at $z_i, i = 1, 2, 3$. Hence, two surface fluxes take place between $\lambda/4$ and z_i and between $3\lambda/4$ and z_i , as schematically depicted by \mathbf{J}_1 and \mathbf{J}_2 , respectively, in Fig. 5.6 (c), (d) and (e). It is noted that the surface flux \mathbf{J}_1 and \mathbf{J}_2 are in the opposite direction because of the fact that $\kappa_{\lambda/4} > \kappa_{z_i}$ and $\kappa_{3\lambda/4} > \kappa_{z_i}$.” [62]

“In the cases where there are curvature extrema between $\lambda/4$ and $3\lambda/4$, we divide the nano-wire into two parts, which are colored by green and magenta colors in Fig. 5.7. The connecting circle between the magenta and green regions is⁸

$$S : x^2 + y^2 = [R_0 + a \sin(2\pi z_i/\lambda)]^2, \quad (5.8)$$

where z_i is the location of the curvature extremum, as illustrated by z_1, z_2 and z_3 in Fig. 5.6 (a). When there is a net surface flux across the surface S from the green to the magenta region, the perturbed nanowire becomes stable; when the net flux across the surface S is in the opposite direction, the interface contracts towards the center of the nanowire at $3\lambda/4$ and eventually breaks into separated nanospheres.” [62]

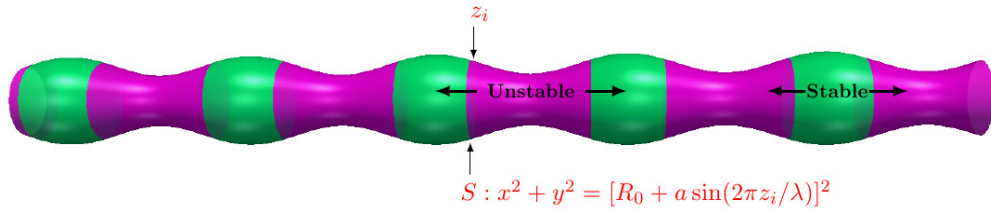


Figure 5.7: “Illustration of the stability criterion: the perturbed nanowire is unstable when there is a net surface flux from the magenta to the green region; otherwise the nanowire is stable. The connecting surface between the magenta and green regions is given by the circle in Eq. (5.8).” [62]

“According to the derivation by Mullins [64], the local surface current $\mathbf{J}_i, i = 1, 2$ is expressed as

$$\mathbf{J}_{1,2} = -(D_s \gamma \Omega \nu / kT) \nabla_s \kappa, \quad (5.9)$$

where D_s is the surface self-diffusion coefficient, ν is the number of diffusing atoms per unit surface area, k is the Boltzmann constant, and T is the temperature. Integrating from $\lambda/4$ to $3\lambda/4$ yields that $\mathbf{J}_{\text{net}} = -(D_s \gamma \Omega \nu / kT) [\kappa(z)_{z=3\lambda/4} - \kappa(z)_{z=\lambda/4}] \mathbf{e}_z$. A straightforward physical interpretation is that the total surface flux switches its direction when the mean curvature at $3\lambda/4$ is greater than the one at $\lambda/4$, in contrast to the situation in two-dimensions shown in Fig. 5.5 (c). When the surface flux is from $\lambda/4$ to $3\lambda/4$, the barycenter of the nanowire shifts from the green to the magenta regions and the

⁸B.N. suggested to add Eq. (5.8) and this contribution is also shown in Fig. 5.7.

nanowire is stabilized; when the surface flux is from $3\lambda/4$ to $\lambda/4$, the barycenter of the nanowire operates in the opposite direction and the nanowire becomes unstable.” [62]

Chapter 6

Underdamped capillary wave

In this chapter, I investigate the dissipation behavior of perturbations at a liquid-liquid interface using the Cahn-Hilliard-Navier-Stokes model. It is observed that a capillary wave is formed when the capillary force is greater than a particular value. The aim is to numerically address the criterion for the occurrence of capillary wave. This chapter was published in Ref. [68].

6.1 Simulation setup

“I take Fe-Sn as an exemplary system for the present study, since its phase diagram reveals a miscibility gap where two immiscible liquids phases, namely the Fe-rich L_1 phase and the Sn-rich L_2 phase, are in chemical equilibrium. We consider a two-dimensional finite domain with a size of $N_x \times N_y$, where N_x and N_y denote the lengths in the horizontal and vertical directions, respectively, and the spatial length is scaled by the capillary length d_0 . As schematically shown in Fig. 6.1, the upper half domain is filled by the L_1 phase and the rest is occupied by the L_2 phase. I assume that the $L_1 - L_2$ interface is located at $y = 0$. The mole fractions of Fe in the L_1 and L_2 phases both are set at equilibrium values from the phase diagram.”[68]

“The simulation parameters are tabulated in Tab. 6.1. The gradient energy coefficient is determined as follows: We set up a flat $L_1 - L_2$ interface and the two phases are in thermodynamic equilibrium. The interfacial energy is calculated as

$$\sigma = 2\kappa_c \int_{-\infty}^{\infty} (dc/dx)^2 dx.$$

The gradient energy coefficient is thus numerically evaluated as $\kappa_c = \sigma/\Psi$, where Ψ is a numerical integration calculated as $\Psi = 2 \int_{-\infty}^{\infty} (dc/dx)^2 dx$. The interfacial tension σ of immiscible liquids is taken from Ref. [55]. The capillary length is estimated by Eq. (3.16), as shown by Langer [69]. The diffusivity D is referred to the self-diffusion coefficient of Fe near the melting point [70]. The densities and the viscosities of the two immiscible

liquids are assumed to be the same, which are approximated by the density and viscosity of Sn at the melting point [71]. The dimensionless number M is proportional to $1/D^2$. The diffusivity D changes with temperature referring to the Stokes-Einstein equation. A slight variation of the diffusivity by raising or decreasing the temperature results in a change of M in magnitude, e.g., if D is $3.1623 \approx \sqrt{10}$ times bigger or less, the order of M varies. Hence, different M corresponds to distinct temperatures.” [68]

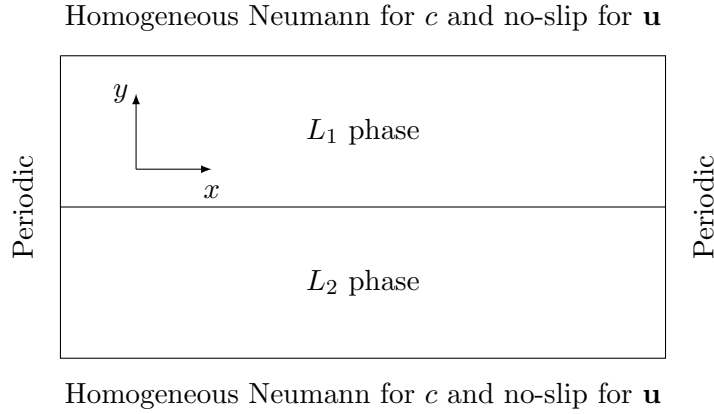


Figure 6.1: “Schematic illustration for the simulation setup.” [68]

Parameters	Descriptions	Value
κ_c (J/m)	Gradient energy coefficient	2×10^{-9}
$\Delta x = \Delta y$	Discretization space step	d_0
Re	Reynolds number	0.01
d_0 (nm)	Capillary length	1
η (Pas)	Dynamic viscosity	1×10^{-3}
ρ (kg/m ³)	Density	7×10^3
D (m ² /s)	Diffusivity	1×10^{-9}
$R_g T_m / v_m$ (J/m ³)	Scaling factor of free energy density	1×10^9
T_m (K)	Monotectic temperature	1403
c_{l1}^0	Monotectic mole fraction of L_1	0.7132
c_{l2}^0	Monotectic mole fraction of L_2	0.2868
$\Omega_1 / (R_g T_m / v_m)$	Interaction coefficient	0.345
$\Omega_2 / (R_g T_m / v_m)$	Interaction coefficient	4.379

Table 6.1: Parameters used for simulations. This table is from Ref. [68].

6.2 Results and discussion

“Initially, a perturbation with 10×10 grid cells is imposed at the middle of the $L_1 - L_2$ planar interface. Due to the perturbation, a local curvature difference appears, which in turn causes a concentration gradient, namely Gibbs-Thomson effect. As the Marangoni force is proportional to the concentration gradient, a Marangoni convection occurs and consequently drives the motion of the interface. The position of the interface is given by the locus of $c = 0.5$ and evolves as a function of time. The result of the interface position for three different Marangoni numbers is shown in Fig. 6.2, where we can see that the perturbation directly dissipates for $M = 5 \times 10^4$. The inset in Fig. 6.2 (a) shows a magnification of the interface at the perturbation region. For higher Marangoni numbers, i.e. $M = 5 \times 10^5$ and $M = 5 \times 10^6$, the interface additionally propagates along the horizontal phase boundary resulting in an interfacial wave, as shown in Fig. 6.2 (b) and (c).” [68]

“The evolution of the interface shown in Fig. 6.2 is until the time of 0.7. A long time behavior of the dissipation of the disturbance is given in Fig. 6.3⁹. At a simulation time of 19 (the cyan line), the interface has a maximum amplitude of 1 grid cell and there is no oscillation observed, which significantly differs from the oscillatory behaviors of the interface in Fig. 6.2 (b) and (c). ” [68]

“Fig. 6.4 (a)¹⁰ portrays an initial state where the planar $L_1 - L_2$ interface is disturbed. Fig. 6.4 (b) and (c) illustrates the velocity field of the convection at $t = 0.2$ and 0.4 , respectively, for $M = 5 \times 10^6$, where the direction of the arrows denote the convective direction for the component Fe. In the L_1 phase (blue region), there are a clockwise (left) vortex and an anti-clockwise (right) vortex. In the L_2 phase (yellow region), there are two convection vortices as well, but the left one is anti-clockwise and the right one is clockwise. With time, the vortices propagate in the horizontal direction.” [68]

“For a planar interface, the equilibrium mole fractions of Fe in the L_1 and L_2 phases follow the phase diagram. For a curved interface, the equilibrium mole fractions in both phases shift away from the phase diagram. The changed amount in each phase is defined as $\Delta c^i := c_{\text{Fe}}^{\text{curved}} - c_{\text{Fe}}^{\text{eq}}$, which is proportional to κ/m_i according to the Gibbs-Thomson law, where κ is the mean curvature and m_i is the slope of the phase diagram for the phase L_i . The Marangoni force is expressed as $\mathbf{F} = \nabla_s \sigma$. With the chain rule and realizing that σ has a single dependency on the interfacial concentration at the isothermal condition, we obtain

$$\mathbf{F} \propto \sigma_{,c} \nabla_s \kappa / m_i. \quad (6.1)$$

Fig. 6.4 (d) depicts the position of the $L_1 - L_2$ interface shown in Fig. 6.4 (c). The curvature is negative at x_2 and is almost zero at x_3 . This gives rise to a curvature

⁹In the revision process of the manuscript, F.W. discussed with M.B.S to add Fig. 6.3.

¹⁰M.S. contributed to the visualization of Fig. 6.4 (a)-(c).

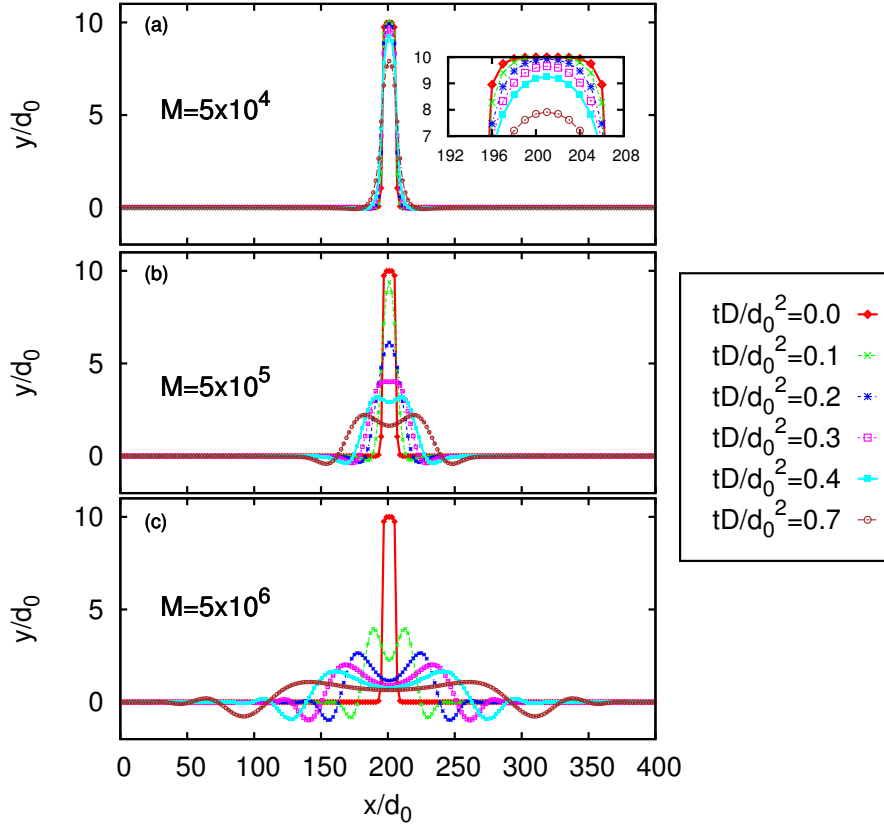


Figure 6.2: “Temporal evolution of the $L_1 - L_2$ interface for three different Marangoni numbers: $M = 5 \times 10^4$, 5×10^5 and 5×10^6 . The Cahn number, which is defined as λ/L , where λ is the width of the interface and L is the height of the domain, is 0.18 by setting $\lambda/d_0 = 18$, $L/d_0 = 100$.” [68]

gradient from x_3 to x_2 . With the assumption that $\sigma_c < 0$ and the fact that $m_{L_2} > 0$, the direction of the Marangoni force is from x_3 to x_2 in the L_2 phase, generating an anti-clockwise vortex in the L_2 phase. Since $\kappa_1 > 0$ and $m_{L_1} < 0$, the Marangoni force is from x_3 to x_1 in the L_1 phase, resulting in a clockwise vortex in the L_1 phase.” [68]

“During the propagation of the interfacial wave, the contour line may be written in Fourier series as

$$y(x, t) = \frac{a_0}{2} + \sum_{k=1}^{\infty} a_k(t) \cos(2\pi kx/N) + b_k(t) \sin(2\pi kx/N), \quad (6.2)$$

where the coefficients are calculated as $a_k(t) = \frac{2}{N} \sum_{x=1}^N y(x, t) \cos(2\pi kx/N) \Delta x$, $b_k(t) = \frac{2}{N} \sum_{x=1}^N y(x, t) \sin(2\pi kx/N) \Delta x$ with N being the number of grid cells in x direction. The amplitudes of the leading term $k = 1$ of the Fourier modes in Eq. (6.2) are plotted as a function of time for different Marangoni numbers in Fig. 6.5. The diagrams in each row of Fig. 6.5 are for different Cahn numbers. The diagram at the top corresponds to $\text{Cn} = 0.045$. The profiles display an exponential decrease of the amplitude $a_1(t)$ to zero for $M = 5 \times 10^3$ and $M = 1 \times 10^4$. For $M = 5 \times 10^4$, the amplitude changes its sign twice in the time interval $[40 : 100]$ and finally approaches zero, which indicates the occurrence

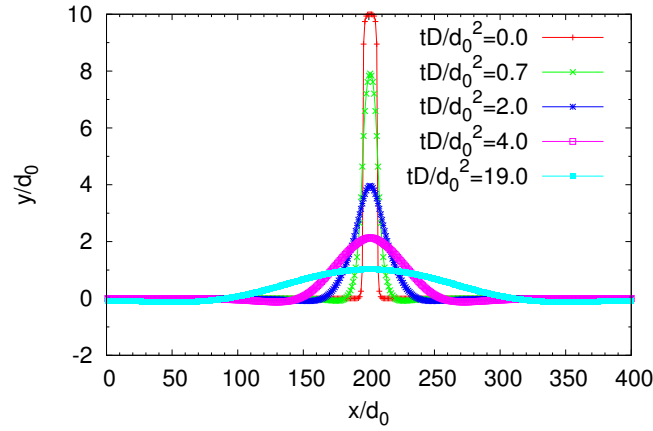


Figure 6.3: “Long time behavior of the dissipation of the disturbance corresponding to Fig. 6.2 (a).”[68]

of oscillation. A further increasing of the Marangoni number to $M = 1 \times 10^5$ leads to a more pronounced oscillation. Similar phenomena are observed for other two Cahn numbers $Cn = 0.18$ and 0.36 , as shown by the second and last diagrams in Fig. 6.5. The difference between the three diagrams is that the critical Marangoni number varies.”[68] “In Fig. 6.6 (a) we discuss the effect of the Cahn number on the critical Marangoni number as a function of the wavenumber k . The cyan, red and blue lines describe the simulation results for Cahn number 0.36 , 0.18 , and 0.045 , respectively. The critical Marangoni number rises as the the Cahn number increases. This is explained as follows¹¹: the Marangoni number is proportional to the gradient energy coefficient κ_c , which defines the interfacial width of the $L_1 - L_2$ interface λ . With the definition of the Cahn number $Cn = \lambda/L$, we reach the conclusion that the Marangoni number quadratically increases with the Cahn number: $M_c \sim Cn^2$.”[68]

“On the other hand, the chemical potential μ is defined as the variational derivative $\mu := \delta\mathcal{F}/\delta c = f_{,c} - 2\kappa_c\Delta c$. Thus $\mu \propto Cn^2$. Therefore, the diffusion term at the right hand side of the Cahn-Hilliard equation becomes stronger while increasing the Cahn number. This results in a pronounced dissipation of the perturbation. To overcome the dissipation effect and to observe the oscillatory convection, the interfacial force has to be increased, which can be achieved by increasing the Marangoni number. ”[68]

“As illustrated in Fig. 6.5, the oscillation period varies with the Marangoni number. The oscillation period for $k = 1$ as a function of Marangoni number at different Cahn numbers are pictured in Fig. 6.6 (b). It shows that the period of oscillation decreases with the increase of Marangoni number. The oscillation is intrinsically driven by the Marangoni convection. Increasing the Marangoni number results in an increase of the frequency of the oscillation, as shown in Fig. 6.5. Since the period of the oscillation is

¹¹This explanation benefits from the discussions with M.B.S.

¹²M.B.S. suggested that the Cahn number is significant for the present study.

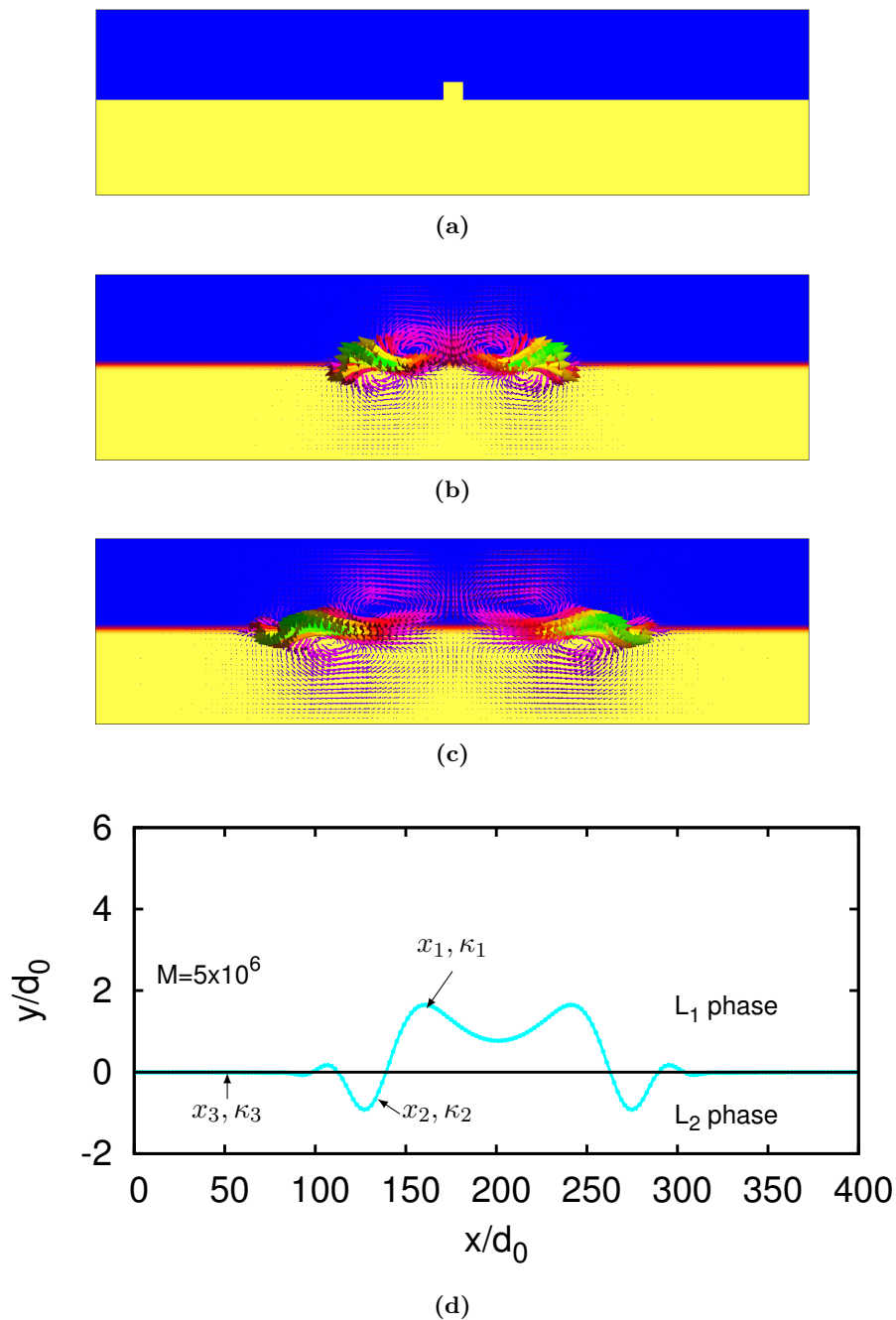


Figure 6.4: “The convection fields for $M = 5 \times 10^6$ at dimensionless time of (a) 0, (b) 0.2, and (c) 0.4. L_1 and L_2 phases are represented by the blue and green regions, respectively. (d) shows the $L_1 - L_2$ interface at $tD/d_0^2 = 0.4$ and schematic illustration for the direction of the convection vortex.” [68]

inversely proportional to the frequency, the frequency of the oscillation decreases with the Marangoni number. For an interfacial wave with a wave length of, for example, $\lambda = 1$ cm and using the parameters: $D = 0.67 \times 10^{-3}$ m²/s, $Cn = 0.045$ and $d_0 = 1$ cm, we obtain that the typical oscillation frequencies range from 0.19 to 0.94 s⁻¹, in comparison to the experimental observed oscillation frequency ranging from 0.21 to 1.2 s⁻¹ [72].” [68]

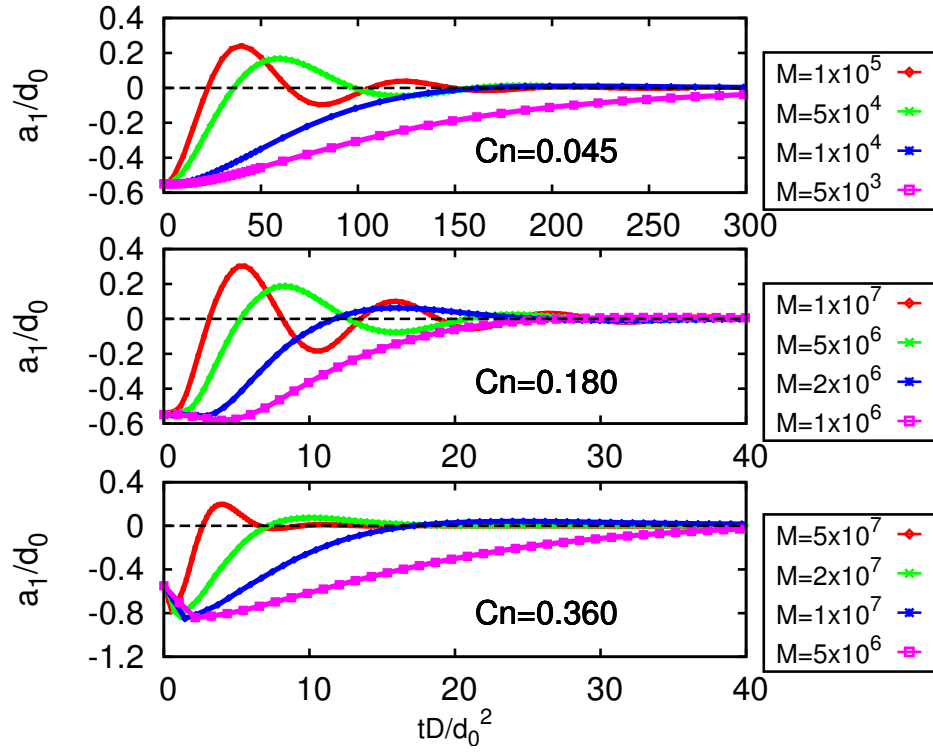


Figure 6.5: “Fourier coefficient $a_1(t)$ as a function of time for different Marangoni numbers. The figures at the first, second and last row correspond to Cahn numbers $Cn = 0.045, 0.18$ and 0.36 , respectively.” [68]

“For the lowest Cahn number $Cn = 0.045$ of the present work, we further increase the Marangoni number to examine the propagation behavior of the interfacial waves. In the first row of Fig. 6.5, the Marangoni number ranges from 5×10^3 to 1×10^5 . Fig. 6.7¹³ illustrates the temporal evolution of the leading mode of the Fourier coefficients a_1 for Marangoni numbers changing from 5×10^5 to 1×10^7 . For smaller Marangoni numbers, i.e. 5×10^5 , 2×10^6 and 5×10^6 , the Fourier coefficient a_1 reveals a under-damped behavior, as shown by the red, blue and green lines. When the Marangoni number reaches 1×10^7 , the maximal value of the Fourier coefficient a_1 increases with time, indicating the occurrence of the oscillatory instability. Hence, the critical Marangoni number of the oscillatory instability of leading mode is between 5×10^6 and 1×10^7 . In the analysis of Reichenbach and Linde [73], they define a critical Marangoni number above which the disturbances can grow in an oscillatory manner. The critical Marangoni from their analysis is on the order of 10^7 . Also, they assume a linear distribution of concentration in the bulk phase. With interfacial matching conditions and after dimensionless, they define a Marangoni number as

$$M_1 = -\frac{d\sigma}{dc} \frac{d_0^2 X}{D\eta}, \quad (6.3)$$

¹³This figure is based a meeting between B.N., M.S., and M.B.S.

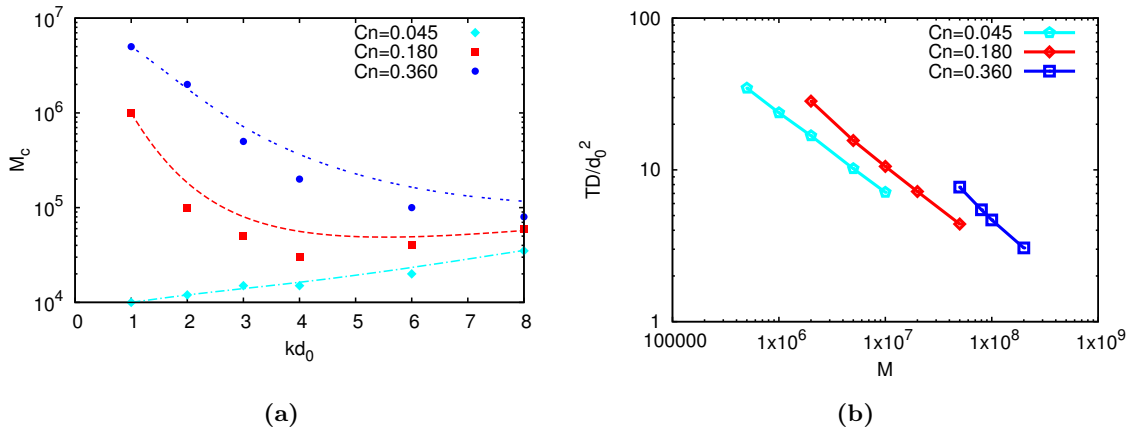


Figure 6.6: “(a) Critical Marangoni number as a function of wave number: the blue, red, cyan lines correspond to the simulation results from the Cahn-Hilliard-Navier-Stokes model for Cahn number 0.36, 0.18 and 0.045, respectively. (b) The dominated oscillation period T in Eq. (6.2) as a function of the Marangoni number for three different Cahn numbers.” [68]

where X is the slope of the linear distribution function of the concentration in bulk, in contrast to the definition of the Marangoni number in the present work

$$M = \kappa_c / (\rho D^2). \quad (6.4)$$

The Marangoni number in the work of Reichenbach & Linde is affected by the bulk

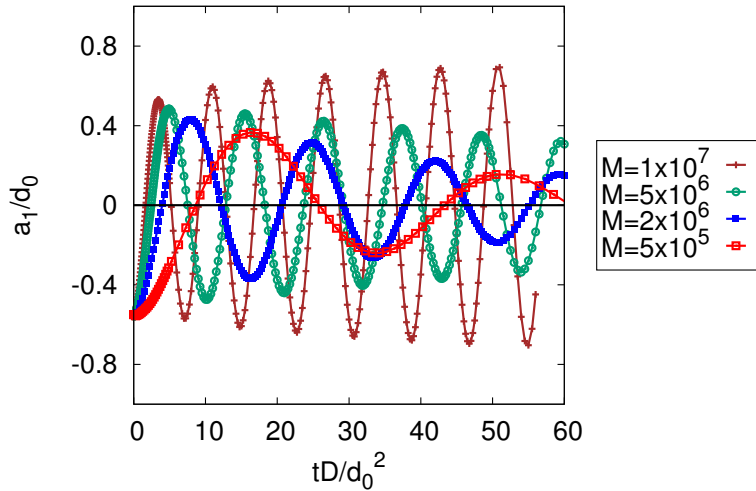


Figure 6.7: “Oscillatory instability of the leading mode: The leading mode of the Fourier coefficients a_1 as a function time for different Marangoni numbers. When the Marangoni number exceeds 10^7 , the Fourier coefficient a_1 increases with time, indicating the oscillatory instability.” [68]

concentration distribution (X), which is different from the Marangoni number defined in the present work. The Marangoni convection in the present work is caused by the surface

gradient of the interfacial concentration/tension due to the inhomogeneous curvature arising from disturbances. In the work of Sternling & Scriven [74] and Reichenbach & Linde, they assume constant fluxes of solute from one phase to the other and the different ratios of diffusivity and viscosity result in the non-uniformity of accumulation or dispersion of solute at the interface, which gives rise to the inhomogeneous interfacial concentration/tension. Though the Marangoni flow in their work is also induced by the gradient of the interfacial tension, the problem treated seems to be different from the present work. Also, we should pay attention that the interfacial tension is only defined on a manifold in the sense of sharp interface. Rigorously, the relevant operator for the stress balance condition at the interface is the surface gradient operator, i.e. $\nabla_s \sigma$, rather than the convective gradient operator that is used in the analysis of Reichenbach & Linde. These differences make it intricate to make a direct comparison of our work with that of Reichenbach & Linde.” [68]

Chapter 7

Effect of capillary flow on motion, coarsening and coalescence of droplets

After the breakup of liquid jets, the resulted droplets may interact with each other, giving rise to a non-uniform concentration gradient along the surface of the droplets. The inhomogeneous interfacial concentration consequently results in a capillary flow, driving the motion of the droplets.

In the first part of this chapter, I analytically study the motion of droplets in a bipolar coordinate. In the second part, I numerically investigate the motion of two droplets using the Cahn-Hilliard-Navier-Stokes model. As a further extension of the work for two droplets, I investigate the effect of capillary flow on the spinodal decomposition process where multi-droplets appear. This chapter was published in Refs. [\[48, 75\]](#).

Part I: Analytical Study on the motion of two droplets

7.1 Analytical study

“In the analysis, we assume undeformable interface and the droplet is in the form of a sphere or a nearly sphere. The capillary number $C := \eta U_c / \sigma$, where η is the viscosity, U_c is the characteristic velocity and σ is the interfacial tension, measures a ratio of the viscosity force to the interfacial tension force. It is an indicative parameter for the degree of deformation. For $C \ll 1$, the droplet stays in the form of a sphere or a nearly sphere [76]. The characteristic velocity U_c is evaluated by D/d_0 where D is the diffusivity and d_0 is the capillary length. With $D \sim 1 \times 10^{-9} \text{ m}^2/\text{s}$, $d_0 \sim 1 \times 10^{-9} \text{ m}$, $\sigma \sim 0.1 \text{ J/m}^2$ and $\eta \sim 1 \times 10^{-3} \text{ Pas}$, the capillary number C is about 10^{-4} , which is much less than 1. Based on this, we study the motion of two nearly spherical droplets in the bipolar coordinate.” [75]

7.1.1 Bipolar coordinate

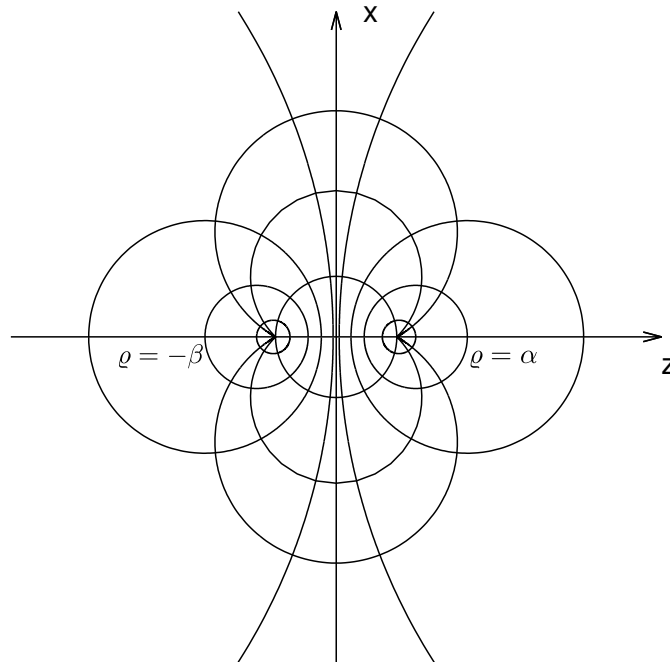


Figure 7.1: “Schematic figure for the bipolar coordinate: the surface of the left droplet is described by $\varrho = -\beta$, and the surface of the right droplet is denoted by $\varrho = \alpha$.” [75]

“The relation between the bipolar coordinate (ϱ, φ) and the cylindrical coordinate (z, x) is defined by [77]

$$z + ix = iq \cot \left[\frac{1}{2}(\varphi + i\varrho) \right], \quad \varphi \in [-\pi, \pi], \quad \varrho \in (-\infty, \infty), \quad (7.1)$$

where q is a positive constant. Eq. (7.1) yields

$$z = \frac{q \sinh \varrho}{\cosh \varrho - \cos \varphi}, \quad x = \frac{q \sin \varphi}{\cosh \varrho - \cos \varphi}. \quad (7.2)$$

By eliminating φ in Eq. (7.2), we have the following relation

$$(z - q \coth \varrho)^2 + x^2 = \left(\frac{q}{\sinh \varrho} \right)^2,$$

which defines a circle with center at $(q \coth \varrho, 0)$ and radius $q/\sinh \varrho$. For the left droplet with radius b and the right droplet with radius a , we have

$$a = \frac{q}{\sinh \alpha}, \quad b = \frac{q}{\sinh \beta},$$

where α and β denote the surfaces of the right and left droplets in the bipolar coordinate, respectively, as shown in Fig. 7.1. The separation distance between the two droplets is given by

$$\begin{aligned} d &= \left(q \coth \alpha - \frac{q}{\sinh \alpha} \right) - \left(-q \coth \beta + \frac{q}{\sinh \beta} \right) \\ &= a(\cosh \alpha - 1) + b(\cosh \beta - 1). \end{aligned}$$

Choosing a as the dimensionless factor for space, we get the new relation between the bipolar coordinate and the cylindrical coordinate

$$z = \frac{\sinh \alpha \sinh \varrho}{\cosh \varrho - \cos \varphi}, \quad x = \frac{\sinh \alpha \sin \varphi}{\cosh \varrho - \cos \varphi}.$$

The non-dimensionalized separation distance is expressed as

$$d = (\cosh \alpha - 1) + \frac{b}{a}(\cosh \beta - 1).$$

Realizing that $\cosh^2 \alpha = 1 + \sinh^2 \alpha$, we get the following relation between α in the bipolar coordinate and the separation distance and the ratio of the radii

$$\begin{aligned} \cosh \alpha &= \frac{(d+1+r)^2 + 1 - r^2}{2(d+1+r)}, \\ \cosh \beta &= \frac{(d+1+r)^2 - 1 + r^2}{2r(d+1+r)}, \end{aligned}$$

where $r = b/a$. In our analysis, without loss of generality, we assume that the bigger droplet is the one with radius b , thus $r \geq 1$.” [75]

7.1.2 Solution of the Laplace equation in the bipolar coordinate

“When the Péclet number fulfills $\frac{d_0 U_c}{D} \ll 1$, the concentration equation transfers into the Laplace equation

$$\Delta c = 0. \quad (7.3)$$

The general solution of the Laplace equation in the bipolar coordinate has been found by Stimson & Jeffery [41, 42]

$$c(\varrho, \varphi) = (\cosh \varrho - \cos \varphi)^{1/2} \sum_{n=1}^{\infty} \left(G_n \cosh(n + 1/2)\varrho + H_n \sinh(n + 1/2)\varrho \right) P_n(\cos \varphi), \quad (7.4)$$

where $P_n(\cos \varphi)$ are Legendre polynomials, and G_n and H_n are coefficients to be determined by boundary conditions.” [75]

“We employ the following boundary conditions [43, 78] for mass transfer between the droplets and continuous phase

$$\begin{aligned} \frac{\cosh \varrho - \cos \varphi}{\sinh \alpha} \frac{\partial c}{\partial \varrho} + \varsigma(c - 1) &= 0, & \varrho &= \alpha, \\ \frac{\cosh \varrho - \cos \varphi}{\sinh \alpha} \frac{\partial c}{\partial \varrho} - \varsigma(c - 1) &= 0, & \varrho &= -\beta, \end{aligned} \quad (7.5)$$

where ς is the Sherwood number which denotes the ratio of convective to diffusive mass transport. Substituting the general solution of the Laplace equation Eq. (7.4) into the boundary conditions Eq. (7.5) result in the following equation (for $\varrho = \alpha$)

$$\begin{aligned} & \sum_{n=1}^{\infty} \left(G_n \sinh \alpha \cosh(n + 1/2)\alpha + H_n \sinh \alpha \sinh(n + 1/2)\alpha \right) P_n(\cos \varphi) \\ & + (\cosh \alpha - \cos \varphi) \sum_{n=1}^{\infty} (2n + 1) \left(G_n \sinh(n + 1/2)\alpha + H_n \cosh(n + 1/2)\alpha \right) P_n(\cos \varphi) \\ & + 2q\varsigma \sum_{n=1}^{\infty} \left(G_n \cosh(n + 1/2)\alpha + H_n \sinh(n + 1/2)\alpha \right) P_n(\cos \varphi) \\ & = 2q\varsigma \frac{1}{(\cosh \alpha - \cos \varphi)^{1/2}}. \end{aligned} \quad (7.6)$$

The right hand side of Eq. (7.6) can be expanded as

$$\frac{1}{(\cosh \alpha - \cos \varphi)^{1/2}} = \sqrt{2} \sum_{n=0}^{\infty} e^{-(n+1/2)\alpha} P_n(\cos \varphi), \quad \forall \varphi \in [-\pi, \pi],$$

which is obtained by making use of the generating function of the Legendre polynomial, and Bonnet’s recursion formula

$$(2n + 1) \cos \varphi P_n(\cos \varphi) = (n + 1)P_{n+1}(\cos \varphi) + nP_{n-1}(\cos \varphi).$$

Comparing the coefficients of the Legendre polynomial in Eq. (7.6), we get the following linear system for the coefficients G_n and H_n

$$\begin{aligned} g_{-1}^{(n,\alpha)} G_{n-1} - g_0^{(n,\alpha)} G_n + g_1^{(n,\alpha)} G_{n+1} + h_{-1}^{(n,\alpha)} H_{n-1} - h_0^{(n,\alpha)} H_n + h_1^{(n,\alpha)} H_{n+1} &= -u^{(n,\alpha)}, \\ g_{-1}^{(n,\beta)} G_{n-1} - g_0^{(n,\beta)} G_n + g_1^{(n,\beta)} G_{n+1} + h_{-1}^{(n,\beta)} H_{n-1} - h_0^{(n,\beta)} H_n + h_1^{(n,\beta)} H_{n+1} &= u^{(n,\beta)}, \end{aligned} \quad (7.7)$$

where the coefficients $g_{-1}^{(n,\alpha)}$, $g_0^{(n,\alpha)}$, $g_1^{(n,\alpha)}$, $h_{-1}^{(n,\alpha)}$, $h_0^{(n,\alpha)}$, $h_1^{(n,\alpha)}$, $g_{-1}^{(n,\beta)}$, $g_0^{(n,\beta)}$, $g_1^{(n,\beta)}$, $h_{-1}^{(n,\beta)}$, $h_0^{(n,\beta)}$, $h_1^{(n,\beta)}$, $u^{(n,\alpha)}$ and $u^{(n,\beta)}$ are given in Appendix C.” [75]

“For two droplets with the same radius, the concentration profile is axial-symmetrical, therefore

$$H_n = 0, \quad \forall n.$$

Since the concentration is bounded, we get $G_n \rightarrow 0$ and $H_n \rightarrow 0$ as $n \rightarrow \infty$. Thus we truncate the linear system Eq. (7.7) by setting $G_n = 0$ and $H_n = 0$ for $n > N$ and solve the $2N$ linear equations.” [75]

“Fig. 7.2 illustrates the isolines of the concentration for two equal-sized droplets with different spacings (The spacing is the separation distance as defined in Section 7.1.1). As shown in Fig. 7.2 (a)-(d), an increase of the separation distance between droplets results in a weaker interaction between the two droplets and the concentration at the surface of each droplets is no-uniform. The inhomogeneous concentration consequently drives the convection. The convection and the diffusion are coupled by the tangential force balance between the surface force caused by the non-uniform interfacial concentration and the viscosity stress due to the resistance of the fluid.” [75]

7.1.3 Stream function

“For an incompressible Stokes flow, the stream function is given by

$$L_{-1}^2 \psi = 0,$$

where L_{-1}^2 is the axial-symmetric Stokes operator, which is expressed in the cylindrical coordinate as

$$L_{-1} = \frac{\partial^2}{\partial z^2} - \frac{1}{z} \frac{\partial}{\partial z} + \frac{\partial^2}{\partial x^2}.$$

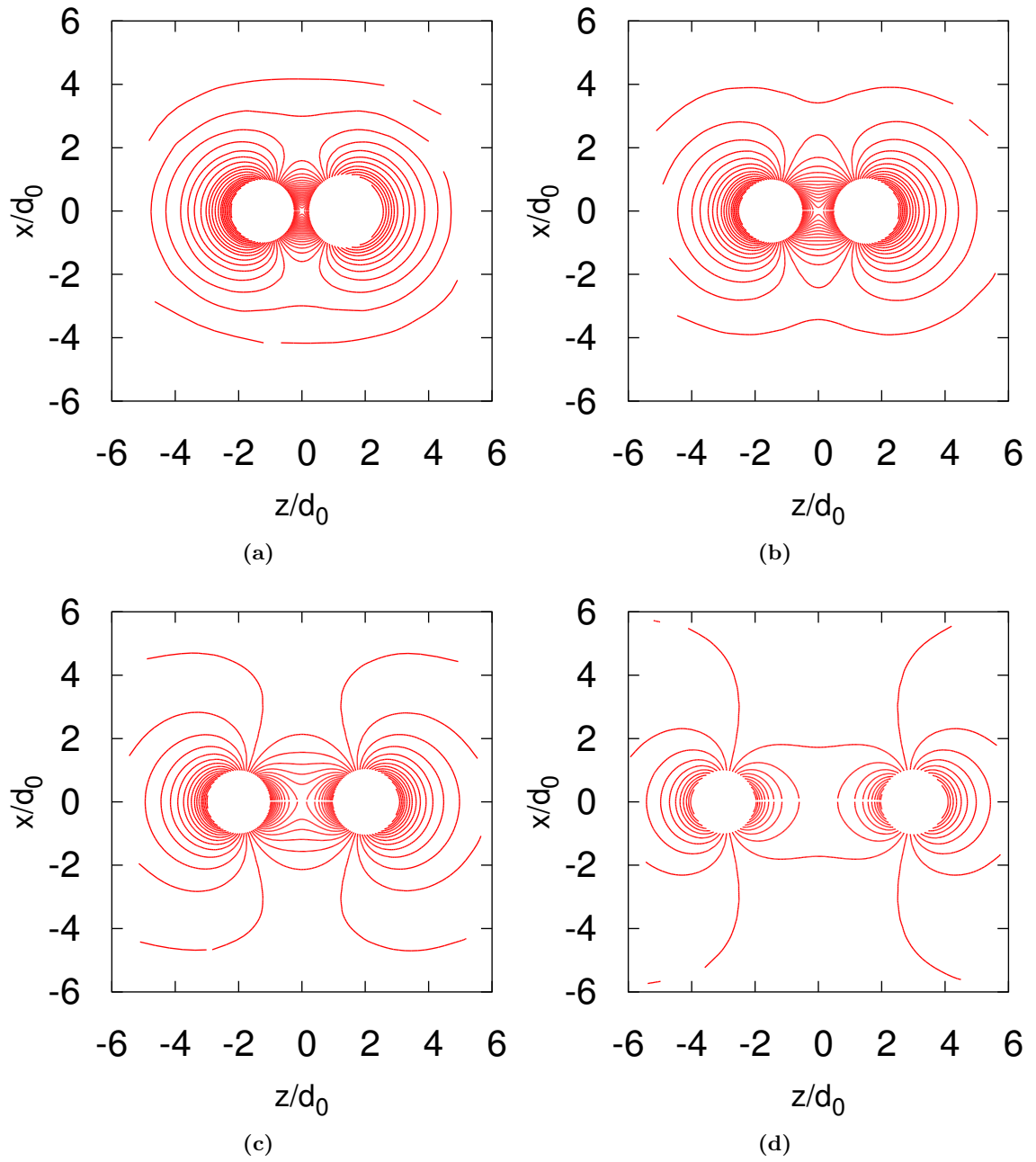


Figure 7.2: “Analytically calculated isolines of concentration for two equal-sized droplets with four different spacings: (a) $d = 0.5$, (b) $d = 1$, (c) $d = 2$ and (d) $d = 4$.” [75]

In the bipolar coordinate, the velocity of the fluid due to convection can be related to the Stokes stream function as

$$\begin{aligned}
 u_{\varrho} &= \frac{(\cosh \varrho - \cos \varphi)^2}{q^2 \sinh \varphi} \frac{\partial \psi}{\partial \varphi}, \\
 u_{\varphi} &= -\frac{(\cosh \varrho - \cos \varphi)^2}{q^2 \sinh \varphi} \frac{\partial \psi}{\partial \varrho},
 \end{aligned}
 \tag{7.8}$$

in which the Stokes stream function satisfies the following equation

$$\Phi^2 (\Phi^2 \psi) = 0, \quad (7.9)$$

with Φ^2 being expressed as

$$\Phi^2 = \frac{\cosh \varrho - \cos \varphi}{q} \left[\frac{\partial}{\partial \varrho} \left(\frac{\cosh \varrho - \cos \varphi}{q} \frac{\partial}{\partial \varrho} \right) + (1 - \cos^2 \varphi) \frac{\partial}{\partial \cos \varphi} \left(\frac{\cosh \varrho - \cos \varphi}{q} \frac{\partial}{\partial \cos \varphi} \right) \right].$$

The general solution of Eq. (7.9) in the bipolar coordinate has been found by Stimson et al. [41]

$$\psi^{(0)}(\varrho, \varphi) = (\cosh \varrho - \cos \varphi)^{-3/2} \sum_{n=1}^{\infty} X_n^{(0)}(\varrho) C_{n+1}^{-1/2}(\cos \varphi), \quad (7.10)$$

$$\psi^{(\alpha)}(\varrho, \varphi) = (\cosh \varrho - \cos \varphi)^{-3/2} \sum_{n=1}^{\infty} X_n^{(\alpha)}(\varrho) C_{n+1}^{-1/2}(\cos \varphi), \quad (7.11)$$

$$\psi^{(\beta)}(\varrho, \varphi) = (\cosh \varrho - \cos \varphi)^{-3/2} \sum_{n=1}^{\infty} X_n^{(\beta)}(\varrho) C_{n+1}^{-1/2}(\cos \varphi), \quad (7.12)$$

where $C_{n+1}^{-1/2}(\cos \varphi)$ is the Gegenbauer polynomial, which is related to the Legendre polynomial by

$$(2n+1)C_{n+1}^{-1/2}(\cos \varphi) = P_{n-1}(\cos \varphi) - P_{n+1}(\cos \varphi), \quad C_{n+1}^{1/2}(\cos \varphi) = P_{n+1}(\cos \varphi).$$

The coefficients in Eq. (7.10)–Eq. (7.12) read as

$$\begin{aligned} X_n^{(0)} &= I_n^{(0)} \cosh(n-1/2)\varrho + J_n^{(0)} \sinh(n-1/2)\varrho \\ &\quad + K_n^{(0)} \cosh(n+3/2)\varrho + L_n^{(0)} \sinh(n+3/2)\varrho, \\ X_n^{(\alpha)} &= I_n^{(\alpha)} e^{-(n-1/2)\varrho} + K_n^{(\alpha)} e^{-(n-1/2)\varrho}, \\ X_n^{(\beta)} &= I_n^{(\beta)} e^{(n-1/2)\varrho} + K_n^{(\beta)} e^{(n-1/2)\varrho}, \end{aligned}$$

where $I_n^{(0)}$, $J_n^{(0)}$, $K_n^{(0)}$, $L_n^{(0)}$, $I_n^{(\alpha)}$, $K_n^{(\alpha)}$, $I_n^{(\beta)}$ and $K_n^{(\beta)}$ are unknown coefficients to be determined by boundary conditions.” [75]

“The continuity of stream function and velocity in the tangential direction yields

$$\psi^{(0)} = \psi^{(\alpha)}, \quad \varrho = \alpha, \quad (7.13)$$

$$\psi^{(0)} = \psi^{(\beta)}, \quad \varrho = -\beta, \quad (7.14)$$

$$\frac{\partial \psi^{(0)}}{\partial \varrho} = \frac{\partial \psi^{(\alpha)}}{\partial \varrho}, \quad \varrho = \alpha, \quad (7.15)$$

$$\frac{\partial \psi^{(0)}}{\partial \varrho} = \frac{\partial \psi^{(\beta)}}{\partial \varrho}, \quad \varrho = -\beta. \quad (7.16)$$

The impenetrability at the surfaces of each droplet gives

$$\mathbf{i}_\varrho \cdot (\mathbf{u}^{(0)} - \mathbf{U}^{(\alpha)}) = 0, \quad \varrho = \alpha, \quad (7.17)$$

$$\mathbf{i}_\varrho \cdot (\mathbf{u}^{(0)} - \mathbf{U}^{(\beta)}) = 0, \quad \varrho = -\beta, \quad (7.18)$$

where \mathbf{i}_ϱ is the unit vector in the bipolar coordinate, $\mathbf{U}^{(\alpha)}$ is the motion velocity of the droplet α , scaled by $\frac{\partial\sigma}{\partial c}/\nu$, where ν is the dynamic viscosity of the continuous phase and σ is the surface tension. $\mathbf{U}^{(\alpha)}$ is expressed as $\mathbf{U}^{(\alpha)} = U^{(\alpha)}\mathbf{i}_z$, where \mathbf{i}_z is the unit vector along the z axis. Eq. (7.17) and Eq. (7.18) generate a relation between $U^{(\alpha)}$ and the stream function as (see Appendix D for the full derivation)

$$\psi^{(0)} = -\frac{1}{2}U^{(\alpha)}\frac{q^2 \sin^2 \varphi}{(\cosh \alpha - \cos \varphi)^2}, \quad (7.19)$$

$$\psi^{(0)} = -\frac{1}{2}U^{(\beta)}\frac{q^2 \sin^2 \varphi}{(\cosh \beta - \cos \varphi)^2}. \quad (7.20)$$

In the tangential direction, the force balance between the viscous stress and capillary force in terms of concentration gradient yields

$$\tau_{\varrho\varphi}^{(0)} - \eta\tau_{\varrho\varphi}^{(\alpha)} = \frac{\cosh \varrho - \cos \varphi}{q} \frac{\partial c}{\partial \varphi}, \quad \varrho = \alpha, \quad (7.21)$$

$$\tau_{\varrho\varphi}^{(0)} - \eta\tau_{\varrho\varphi}^{(\beta)} = -\frac{\cosh \varrho - \cos \varphi}{q} \frac{\partial c}{\partial \varphi}, \quad \varrho = -\beta, \quad (7.22)$$

where η is the ratio of viscosity between the droplet and the continuous phase and $\tau_{\varrho\varphi}$ is the tangential component of the viscous stress tensor, calculated by

$$\begin{aligned} \tau_{\varrho\varphi} &= \mathbf{i}_\varrho \cdot \left[\frac{1}{2}(\nabla \mathbf{u} + \nabla \mathbf{u}^T) \right] \cdot \mathbf{i}_\varphi \\ &= h \left[u_{\varrho,\varphi} + u_{\varphi,\varrho} - hu_\varrho \left(\frac{1}{h} \right)_{,\varrho} - hu_\varphi \left(\frac{1}{h} \right)_{,\varphi} \right], \end{aligned}$$

where h is the scaling factor in the bipolar coordinate, which is defined as

$$h := \frac{\cosh \varrho - \cosh \varphi}{q}.$$

Boundary conditions Eqs. (7.13)-(7.16) give

$$\sum_{n=1}^{\infty} X_n^{(0)}(\alpha) C_{n+1}^{-1/2}(\cos \varphi) = \sum_{n=1}^{\infty} X_n^{(\alpha)}(\alpha) C_{n+1}^{-1/2}(\cos \varphi) \quad (7.23)$$

$$\sum_{n=1}^{\infty} X_n^{(0)}(-\beta) C_{n+1}^{-1/2}(\cos \varphi) = \sum_{n=1}^{\infty} X_n^{(\beta)}(-\beta) C_{n+1}^{-1/2}(\cos \varphi) \quad (7.24)$$

$$\sum_{n=1}^{\infty} \frac{dX_n^{(0)}(\alpha)}{d\varrho} C_{n+1}^{-1/2}(\cos \varphi) = \sum_{n=1}^{\infty} \frac{dX_n^{(\alpha)}(\alpha)}{d\varrho} C_{n+1}^{-1/2}(\cos \varphi) \quad (7.25)$$

$$\sum_{n=1}^{\infty} \frac{dX_n^{(0)}(-\beta)}{d\varrho} C_{n+1}^{-1/2}(\cos \varphi) = \sum_{n=1}^{\infty} \frac{dX_n^{(\beta)}(-\beta)}{d\varrho} C_{n+1}^{-1/2}(\cos \varphi), \quad \forall \varphi \in [-\pi, \pi]. \quad (7.26)$$

Eqs. (7.19) and (7.20) are equivalent to

$$\sum_{n=1}^{\infty} X_n^{(0)}(\alpha) C_{n+1}^{-1/2}(\cos \varphi) = -U^{(\alpha)} q^2 \frac{\sin^2 \varphi}{2(\cosh \alpha - \cos \varphi)^{1/2}} \quad (7.27)$$

$$\sum_{n=1}^{\infty} X_n^{(0)}(-\beta) C_{n+1}^{-1/2}(\cos \varphi) = -U^{(\beta)} q^2 \frac{\sin^2 \varphi}{2(\cosh \alpha - \cos \varphi)^{1/2}}, \quad \forall \varphi \in [-\pi, \pi] \quad (7.28)$$

The force balance equations Eqs. (7.21) and (7.22) can be simplified to

$$\begin{aligned} \sum_{n=1}^{\infty} \left(\frac{d^2 X_n^{(0)}(\alpha)}{d\varrho^2} - \eta \frac{d^2 X_n^{(\alpha)}(\alpha)}{d\varrho^2} \right) C_{n+1}^{-1/2}(\cos \varphi) = & (1 - \eta) q^2 U^{(\alpha)} \left[\frac{\cosh \alpha \sin^2 \varphi}{4(\cosh \alpha - \cos \varphi)^{3/2}} \right. \\ & \left. - \frac{3 \sinh^2 \alpha \sin^2 \varphi}{8(\cosh \alpha - \cos \varphi)^{5/2}} \right] \\ & + \frac{q^2 \sin^2 \varphi}{(\cosh \alpha - \cos \varphi)^{1/2}} \frac{\partial c}{\partial \cos \varphi}, \quad (7.29) \end{aligned}$$

and

$$\begin{aligned} \sum_{n=1}^{\infty} \left(\frac{d^2 X_n^{(0)}(\alpha)}{d\varrho^2} - \eta \frac{d^2 X_n^{(\beta)}(-\beta)}{d\varrho^2} \right) C_{n+1}^{-1/2}(\cos \varphi) = & (1 - \eta) q^2 U^{(\beta)} \left[\frac{\cosh \beta \sin^2 \varphi}{4(\cosh \beta - \cos \varphi)^{3/2}} \right. \\ & \left. - \frac{3 \sinh^2 \beta \sin^2 \varphi}{8(\cosh \beta - \cos \varphi)^{5/2}} \right] \\ & - \frac{q^2 \sin^2 \varphi}{(\cosh \beta - \cos \varphi)^{1/2}} \frac{\partial c}{\partial \cos \varphi}, \quad \forall \varphi \in [-\pi, \pi]. \quad (7.30) \end{aligned}$$

The first term at the right hand side of Eq. (7.29) and Eq. (7.30) is the viscous resistance and the second term is the capillary force in terms of the concentration gradient.” [75]

“Using the expansion (See Appendix E for the derivation)

$$\frac{\sin^2 \varphi}{2(\cosh \alpha - \cos \varphi)^{1/2}} = \frac{\sqrt{2}}{2} \sum_{n=1}^{\infty} n(n+1) \left(\frac{e^{-(n-1/2)\alpha}}{2n-1} - \frac{e^{-(n+3/2)\alpha}}{2n+3} \right) C_{n+1}^{-1/2}(\cos \varphi), \quad (7.31)$$

$$\frac{\cosh \alpha \sin^2 \varphi}{4(\cosh \alpha - \cos \varphi)^{3/2}} = \frac{\sqrt{2}}{4} \sum_{n=1}^{\infty} n(n+1) \left(e^{-(n-1/2)\alpha} + e^{-(n+3/2)\alpha} \right) C_{n+1}^{-1/2}(\cos \varphi), \quad (7.32)$$

$$\frac{3 \sinh^2 \alpha \sin^2 \varphi}{8(\cosh \alpha - \cos \varphi)^{5/2}} = \frac{\sqrt{2}}{8} \sum_{n=1}^{\infty} n(n+1)(2n+1) \left(e^{-(n-1/2)\alpha} - e^{-(n+3/2)\alpha} \right) C_{n+1}^{-1/2}(\cos \varphi). \quad (7.33)$$

Eq. (7.23)-Eq. (7.30) result in the following linear system

$$\Xi_n \mathbf{b}_n = q^2 \mathbf{t}_n^{(\alpha)} + q^2 \mathbf{t}_n^{(\beta)} - q^2 U^{(\alpha)} \mathbf{v}_n^{(\alpha)} - q^2 U^{(\beta)} \mathbf{v}_n^{(\beta)}, \quad (7.34)$$

where $\mathbf{b}_n = (I_n^{(0)}, J_n^{(0)}, K_n^{(0)}, L_n^{(0)}, I_n^{(\alpha)}, K_n^{(\alpha)}, I_n^{(\beta)}, K_n^{(\beta)})^T$. Ξ_n , \mathbf{t}_n and \mathbf{v}_n are matrices given in Appendix F. It is important to note that the factor of the second term at the right hand side of Eq. (7.29): $\frac{q^2 \sin^2 \varphi}{(\cosh \alpha - \cos \varphi)^{1/2}}$ can be expanded by making use of Eq. (7.31). As noted above, the concentration profile is obtained by solving the linear system Eq. (7.7). In order to find the function $c(\alpha, \cos \varphi)$, we plot the concentration as a function of $\cosh \varphi$ in Fig. 7.3. A quadratic polynomial is used to fit the data points reading

$$c(\alpha, \cos \varphi) = \frac{1}{2} a (\cos \varphi)^2 + b \cos \varphi + d.$$

The fitted results for coefficients a and b are listed in Tab. 7.1. A derivative with respect

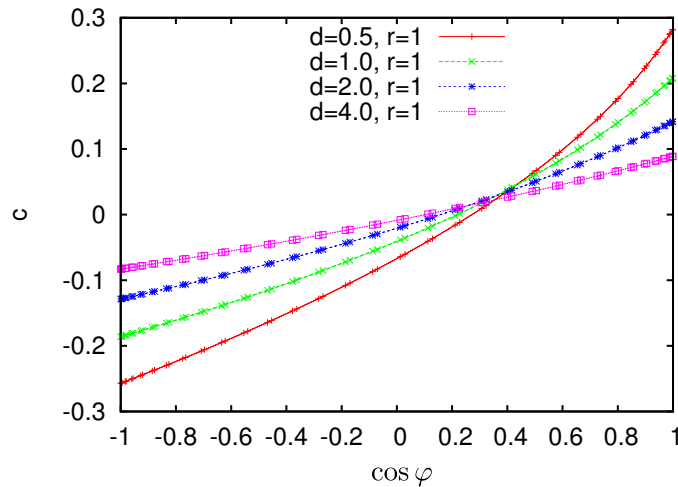


Figure 7.3: “Concentration as a function of $\cos \varphi$ at $\varrho = \alpha$ for different spacings.” [75]

to $\cos \varphi$ yields

$$\frac{\partial c}{\partial \cos \varphi} = a \cos \varphi + b. \quad (7.35)$$

Substituting Eq. (7.35) into Eq. (7.29) and combining the recursion relation for the Gegenbauer polynomial, we get the matrices $\mathbf{t}_n^{(\alpha)}$ and $\mathbf{t}_n^{(\beta)}$ (See Appendix G).” [75]

Parameters	a_α	b_α	a_β	b_β
$d = 0.5, r = 1$	0.157295	0.256925	0.157295	0.256925
$d = 1.0, r = 1$	0.103128	0.191166	0.103128	0.191166
$d = 2.0, r = 1$	0.0546745	0.133095	0.0546745	0.133095
$d = 4.0, r = 1$	0.0231863	0.0853591	0.0231863	0.0853591
$d = 1.0, r = 2$	0.0684062	0.194992	0.25623	0.33982
$d = 1.0, r = 4$	0.0441915	0.216205	0.448396	0.490051

Table 7.1: “Fitted parameter in Eq. (7.35).” [75]

“According to Refs. [41, 44], the drag force on each droplet is given by

$$F^{(\alpha)} = \frac{2\sqrt{2}\pi\nu}{q} \sum_{n=1}^{\infty} (I_n^{(0)} + J_n^{(0)} + K_n^{(0)} + L_n^{(0)}),$$

$$F^{(\beta)} = \frac{2\sqrt{2}\pi\nu}{q} \sum_{n=1}^{\infty} (I_n^{(0)} - J_n^{(0)} + K_n^{(0)} - L_n^{(0)}).$$

Assuming quasi-stationary, we get

$$F^{(\alpha)} = 0, \quad F^{(\beta)} = 0. \quad (7.36)$$

Combining Eqs. (7.34) and (7.36), we get the following system for the moving velocity of two droplets

$$\begin{aligned} \Lambda_\alpha^+ U_\alpha + \Lambda_\beta^+ U_\beta &= \Lambda_{t_\alpha}^+ + \Lambda_{t_\beta}^+, \\ \Lambda_\alpha^- U_\alpha + \Lambda_\beta^- U_\beta &= \Lambda_{t_\alpha}^- + \Lambda_{t_\beta}^-, \end{aligned} \quad (7.37)$$

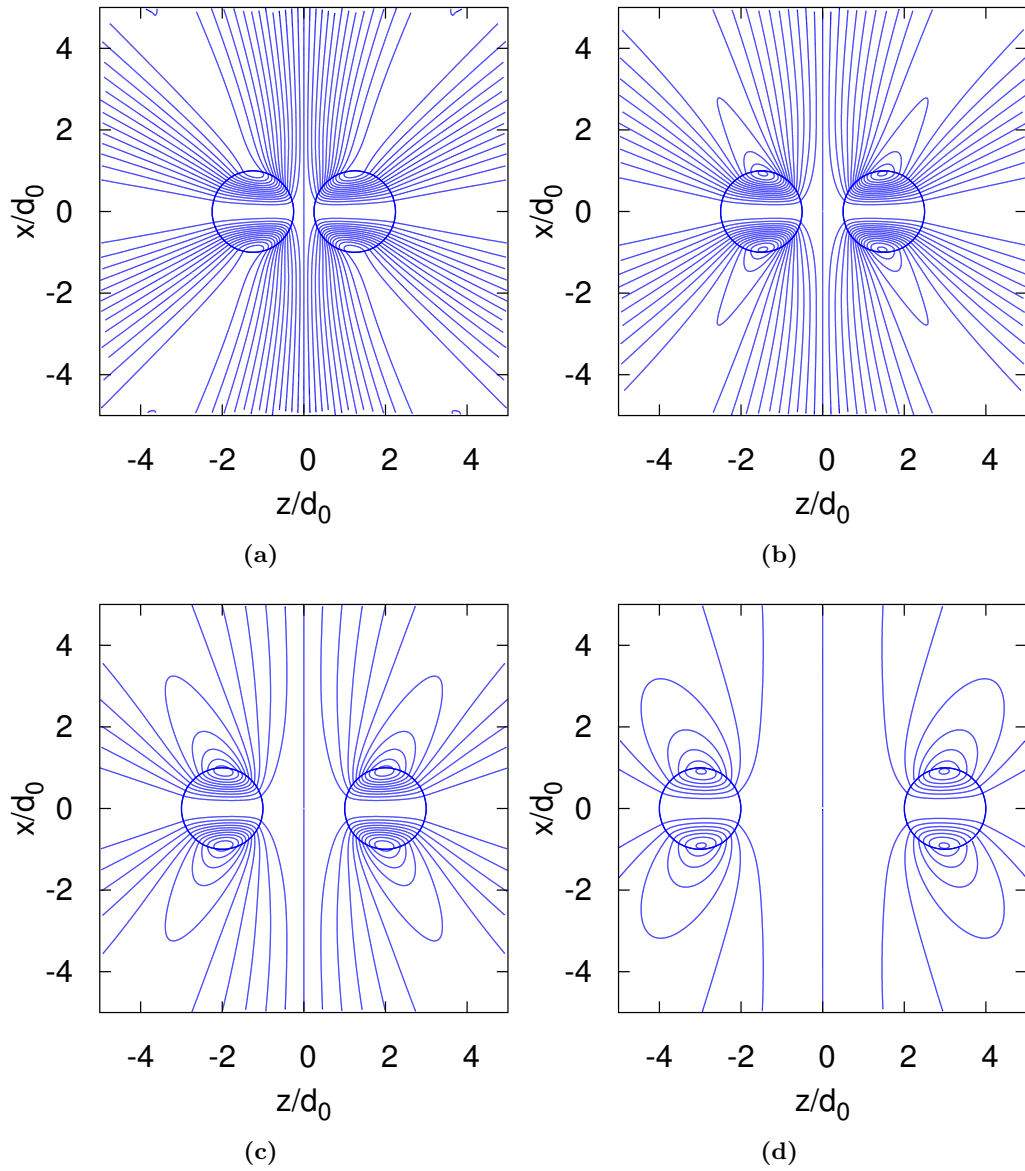


Figure 7.4: “Analytically calculated stream lines for two equal-sized droplets with different spacings: (a) $d = 0.5$, (b) $d = 1$, (c) $d = 2$ and (d) $d = 4$.” [75]

where

$$\begin{aligned}\Lambda_{\alpha}^{\pm} &= \sum_{n=1}^{\infty} I_n^{(v_n^{\alpha},0)} \pm J_n^{(v_n^{\alpha},0)} + K_n^{(v_n^{\alpha},0)} \pm L_n^{(v_n^{\alpha},0)}, \\ \Lambda_{\beta}^{\pm} &= \sum_{n=1}^{\infty} I_n^{(v_n^{\beta},0)} \pm J_n^{(v_n^{\beta},0)} + K_n^{(v_n^{\beta},0)} \pm L_n^{(v_n^{\beta},0)}, \\ \Lambda_{t_{\alpha}}^{\pm} &= \sum_{n=1}^{\infty} I_n^{(t_n^{\alpha},0)} \pm J_n^{(t_n^{\alpha},0)} + K_n^{(t_n^{\alpha},0)} \pm L_n^{(t_n^{\alpha},0)}, \\ \Lambda_{t_{\beta}}^{\pm} &= \sum_{n=1}^{\infty} I_n^{(t_n^{\beta},0)} \pm J_n^{(t_n^{\beta},0)} + K_n^{(t_n^{\beta},0)} \pm L_n^{(t_n^{\beta},0)}.\end{aligned}$$

In summary, the whole analysis reduces to three linear systems, Eqs. (7.7), (7.34) and (7.37), where Eq. (7.7) concerns the analytical solution for the concentration, Eq. (7.34) deals with the solution for the stream function which is based on the solution of Eq. (7.7). The motion velocity is given by Eq. (7.37). It is important to note that Eq. (7.37) needs to be solved first after obtaining the concentration profile, in order to get the motion velocity. Then, the coefficients $I_n^{(0)}$, $J_n^{(0)}$, $K_n^{(0)}$, $L_n^{(0)}$, $I_n^{(\alpha)}$, $K_n^{(\alpha)}$, $I_n^{(\beta)}$, $K_n^{(\beta)}$ in the general solution of stream function Eqs. (7.10)-(7.12) are obtained by substituting $U^{(\alpha)}$ and $U^{(\beta)}$ into Eq. (7.34).” [75]

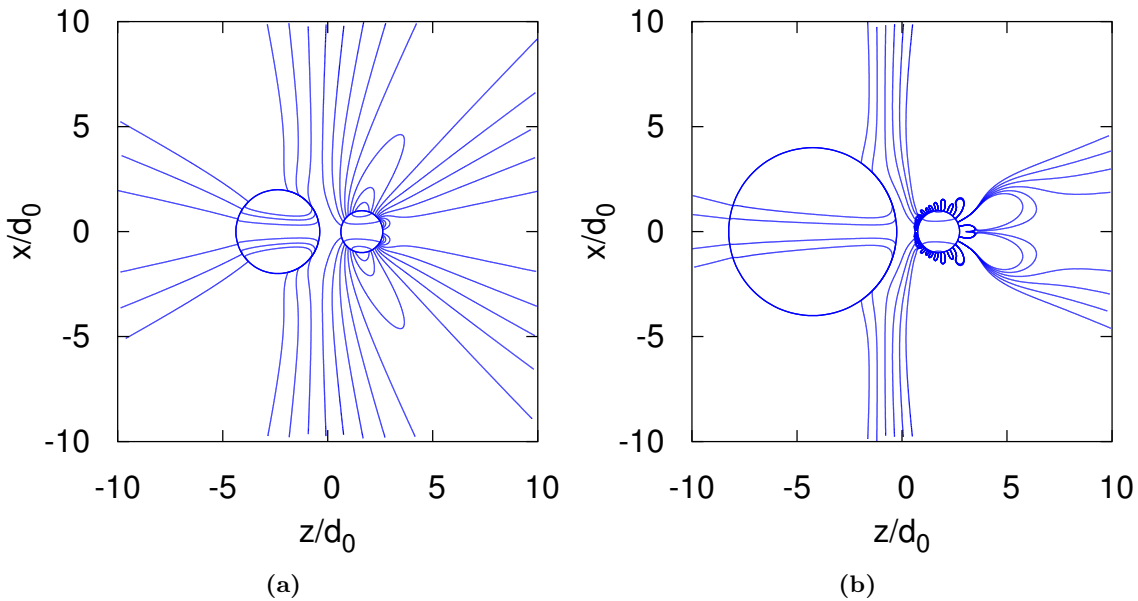


Figure 7.5: “Stream lines for different ratios of the radius of the droplet: (a) $r = 2$, (b) $r = 4$. In both cases, the spacing is 1.” [75]

“Fig. 7.4 shows the stream lines for two equal-sized droplets with spacing ranging from 0.5 to 4. It is observed that there are four convection swirls around the droplets. These convection swirls transport the solute in the continuous phase and in the droplets, which give rise to the non-uniform concentration along the surface of the droplet. Consequently, the capillary force because of the gradient of the concentration drives the motion of the droplets.” [75]

“The stream lines for different ratios of the radius of the droplet with the same spacing are illustrated in Fig. 7.5. The size difference results in the asymmetry of the stream lines. For $r = 2$, we can still observe four convection swirls around the surface of the droplet. However, the convection swirl is not able to occur around the surface of the smaller droplet with increasing the radius ratio to 4, as shown in Fig. 7.5 (b).” [75]

“At the end of the section of our analysis which is based on the work of Golovin et al., we point out some major differences between the work of us and the one from Golovin et al.: (i) One important technique which has not been reported in the work of Golovin et

al. is presented in the present work. Eqs. (7.29) and (7.30) are two boundary conditions for the stream function resulting from the tangential stress balance. The left hand sides of Eqs. (7.29) and (7.30) are in terms of Gegenbauer polynomials. To compare the coefficients of the Gegenbauer polynomials, the right hand sides of Eqs. (7.29) and (7.30) have to be expanded in terms of Gegenbauer polynomials. Concerning the last term at the right hand sides of Eqs. (7.29) and (7.30): $\frac{q^2 \sin^2 \varphi}{(\cosh \alpha - \cos \varphi)^{1/2}} \frac{\partial c}{\partial \cos \varphi}$, the expansion of the factor $\frac{q^2 \sin^2 \varphi}{(\cosh \alpha - \cos \varphi)^{1/2}}$ into Gegenbauer polynomials is given by Eq. (7.31) and Appendix E. If we use the general solution for concentration c (Eq. (7.4)) to calculate the derivative $\frac{\partial c}{\partial \cos \varphi}$, we would have a multiplication of Gegenbauer polynomials with Legendre polynomials, which makes it difficult to compare the coefficients of Gegenbauer polynomials at both sides of Eqs. (7.29). To avoid this, we propose a quadratic polynomial fit to the function $c(\cos \varphi)$. The quadratic fitting and the corresponding fitting results are shown in Fig. 7.3 and Tab. 7.1. Thus the derivative yields $\frac{\partial c}{\partial \cos \varphi} = a \cos \varphi + b$. Then we expand the term $\frac{q^2 \sin^2 \varphi}{(\cosh \alpha - \cos \varphi)^{1/2}} (a \cos \varphi + b)$ into Gegenbauer polynomials with the aid of the recursion relation for Gegenbauer polynomial, which is shown in Appendix G.

(ii) In the work of Golovin et al., it is not clear how the linear systems are derived. The detailed derivations are presented in the present work. (iii) We show the stream lines and isolines of concentration affected by the spacing between the two droplets, which is not analyzed in the work of Golovin et al.” [75]

7.1.4 Interpretation of the analysis

The framework of the analysis is sketched in Fig. 7.6. The aim of the analysis is to find the analytical solutions for the Laplace equation, Eq. (7.3) and the biharmonic equation, Eq. (7.9) in the bipolar coordinate. The solution of the Laplace equation is expressed as a summation of the Legendre polynomials, as depicted by Eq. (7.4). Applying the boundary conditions, Eq. (7.5), the unknown coefficients in Eq. (7.4) are determined and we thereafter obtain the concentration distribution, as shown in Fig. 7.2.

The stream function follows the biharmonic equation, Eq. (7.9), the solution of which is expressed as a summation of the Gegenbauer polynomials, as shown by Eqs. (7.10), (7.11) and (7.12). In the general solutions for the stream function, the unknown coefficients $I_n^{(0)}$, $J_n^{(0)}$, $K_n^{(0)}$, $J_n^{(\alpha)}$, $I_n^{(\alpha)}$, $J_n^{(\alpha)}$, $K_n^{(\alpha)}$, $J_n^{(\beta)}$, $I_n^{(\beta)}$, $J_n^{(\beta)}$, $K_n^{(\beta)}$, and $J_n^{(\beta)}$ are determined by applying the boundary conditions, Eqs. (7.13)-(7.20), which result in a linear system for the eight unknowns, as depicted by Eq. (7.34). It is noted that the linear system, Eq. (7.34) contains two additional unknowns, $U^{(\alpha)}$ and $U^{(\beta)}$, which are obtained by solving the equation system, Eq. (7.37).

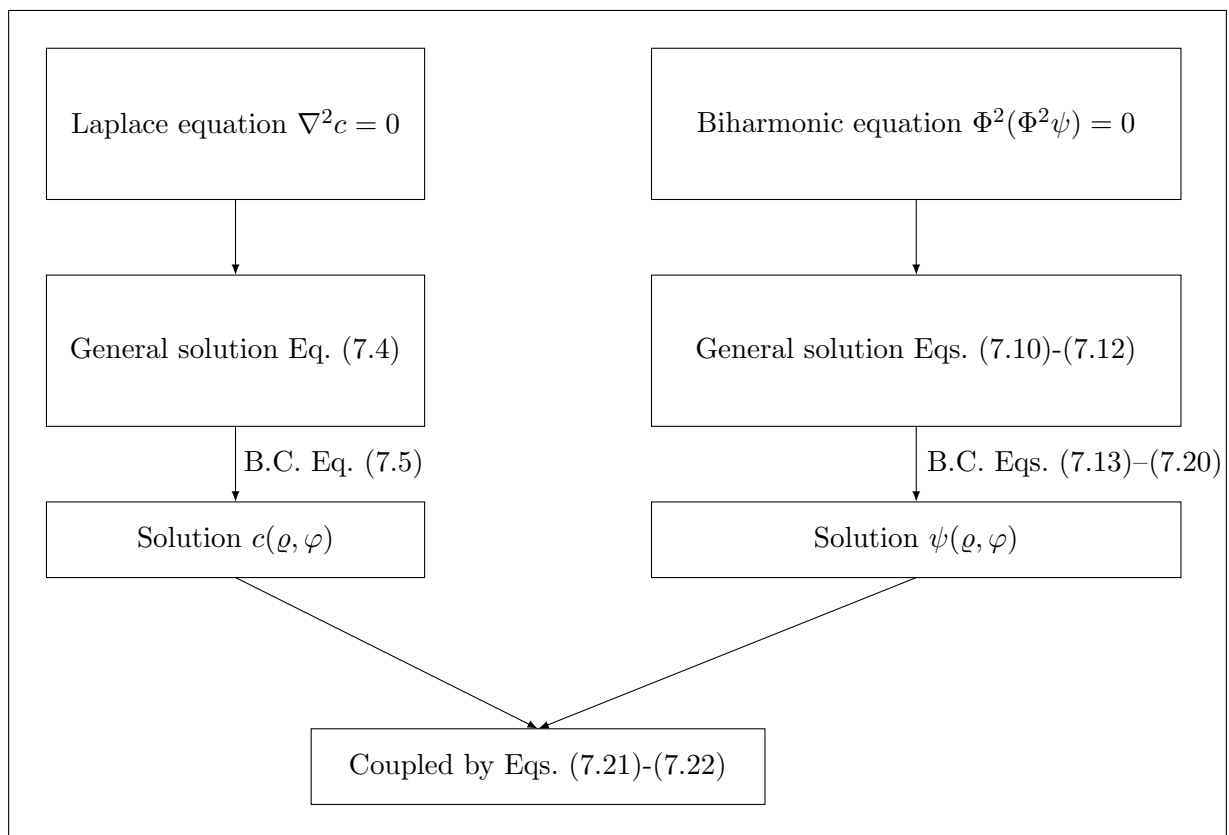


Figure 7.6: Schematic illustration for the framework of the analysis.

Part II: Numerical Investigation

7.2 Numerical investigation on the motion of the droplets driven by capillary flow

7.2.1 Motion

“We place two equal-sized droplets (radius of 30 grid points) of L_2 phase with a distance above 20 grid cells apart, which is greater than the interface width. This setting ensures that coalescence and coarsening do not take place between the droplets. The size of the simulation domain is 300×300 grid cells. Periodic boundary conditions are implemented both, for concentration and velocity fields.” [48]

“Due to the application of solving equations based on an explicit finite difference discretization on a rectangular mesh, there are curvature differences along the surface of droplets after the filling of droplets into the simulation domain. We therefore use the following equation to smoothen the interface of each droplet before starting the simulation

$$c_n = c_o + D_c \nabla^2 c_o,$$

where c_n and c_o are the new and old concentrations, respectively, and D_c is a coefficient set to be 0.05. After 20 steps smoothening, the relative curvature differences (grid effect) along the droplets become less than 1% of the curvature of an ideal circle, such that the curvature differences due to filling can be neglected.” [48]

“After the above precondition, we start simulations with a temperature being 5 K below the temperature of $T/T_m = 1$, to make sure that the droplets maintain their size. However, due to this setting, the droplets grow a little in size and after a transient state reach the equilibrium with the matrix. After reaching equilibrium, these two droplets move towards each other due to the capillary flow induced by the nonuniform concentration along the surface of the droplets.” [48]

“The convection pattern and stream lines for two droplets 40 grid cells apart, are shown in Fig. 7.7 (a) and (b)¹⁴, respectively. Interestingly, several swirls appear around the interface of each droplet. As we can see from the convection direction and the stream line, the swirls between the inter-droplet region influences the motion of the droplets towards each other, whereas the swirls on the opposite sides of the droplets are likely to play a negative role.” [48]

“The mass transfer along the surface of each droplet and between the two droplets are influenced by the convection through the convective term in the concentration equation, causing the shift in barycenter of each droplet. The velocity as a function of initial distance between the two droplets is shown in Fig. 7.7 (c). The star, circle and square symbols denote the simulated velocities when the dimensionless number M is 10, 100

¹⁴M.S. made contributions to the visualization of the convection field in Fig. 7.6 (a) and the streams in Fig. 7.6 (b).

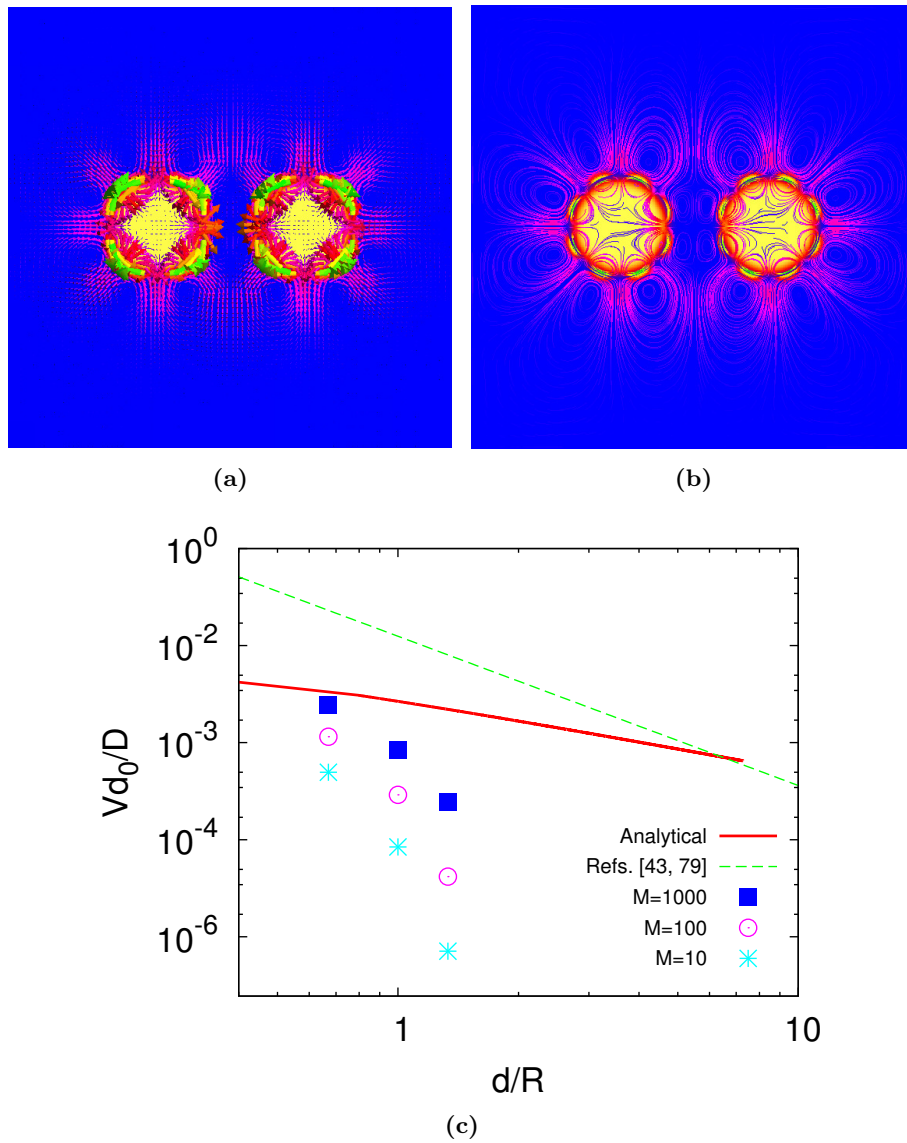


Figure 7.7: “(a) The convection profile of the capillary flow under the condition: $d/d_0 = 40$, $R/d_0 = 30$, $\varsigma = 2$, at a dimensionless time of 2×10^5 , (b) the stream lines of the capillary flow corresponding to image (a). (c) the motion velocity of droplet’s barycenter varying with distance between droplets: the solid red line is the analytical results from section 7.1, the dashed green line shows the result from Refs. [43, 79] according to Eq. (7.38), and the star, circle, square symbols denote the simulation results at different dimensionless number M .” [48]

and 1000, respectively. The solid red line is the analytical result from section 7.1 and the dashed green line shows the result from Refs. [43, 79] according to the equation

$$V = \frac{\varsigma}{2.5(\varsigma + 1)(\varsigma + 2)} \left(\frac{d}{R} \right)^{-2}. \quad (7.38)$$

As denoted by symbols representing the simulation results, the effect of convection is reduced with increasing the distance between the two droplets and becomes stronger

while increasing the dimensionless number M . The former tendency is easy to understand: The droplets with a larger distance have a comparable effect of convection at inner- and outer-droplet region and smaller concentration difference along the surface. While decreasing the distance between the droplets, the effect of inner swirls becomes stronger than outer swirls, and this, subsequently, causes a dramatic enhancement of the velocity. For comprehending the latter phenomenon, we rewrite the dimensionless number as $M = (RT/v_m)d_0^2/(\rho D_l^2)$, where RT/v_m is a scaling factor derived from surface tension and capillary length. The increase of the dimensionless number from 10 to 100 or 1000 can be achieved by decreasing the diffusion coefficient to $D_l/\sqrt{10}$ or one order lower, which is possible in real alloys [80]. The trending of velocity vs initial distance between droplets, obtained from simulation, is quite similar to the one from Eq. (7.38), which is used to predict the case when $d \rightarrow \infty$.”[48]

“However, the velocity obtained from our simulation using the capillary stress tensor is less than that obtained from the analytical result. This may be due to the competition between the inter-droplets swirls and the ones at the opposite sides of the droplets, which has not been considered in the analytical model. Decreasing the distance of the two droplets can strengthen the effect of convection, but due to the fact that we have a finite interface width, which has not been considered in the analytical model, the droplets are expected to undergo a coalescence process with the decrease in distance.”[48]

7.2.2 Transition from motion to coalescence

“As described in Section 7.2.1, the two distant droplets move towards each other due to the capillary flow induced by the non-uniform curvature distribution along the surface. The interfaces of the two droplets can overlap each other after some time, thereafter, coalescence will be the dominant mechanism between them.”[48]

“As illustrated in Fig. 7.8 (a), we show the trace of the line with a value of 0.5, of each droplet, when the initial distance between the two droplets is 30 grid cells. The region between the two droplets is zoomed in Fig. 7.8 (b). The solid red, dashed blue, dotted pink, dot dashed black and dot dot dashed green lines correspond to the simulation time of 8760, 27760, 41760, 52760 and 55160, respectively. From the figure we can see, the droplets almost maintain the morphology till the time 52760 during the motion process. However, the droplets develop protrusions in the x direction (see Fig. 7.8 (b)) decreasing the distance between the droplets, which means that they go inside the coalescing stage.”[48]

“In addition, Fig. 7.8 (c)¹⁵ shows the barycenter of the left droplet at the simulation time of 8760, 27760, 41760, 52760 and 55160, represented by the red circle, blue square, pink lozenge, black pentagon and green triangle, respectively.”[48]

¹⁵R.M. suggested to trace the barycenter of the droplets.

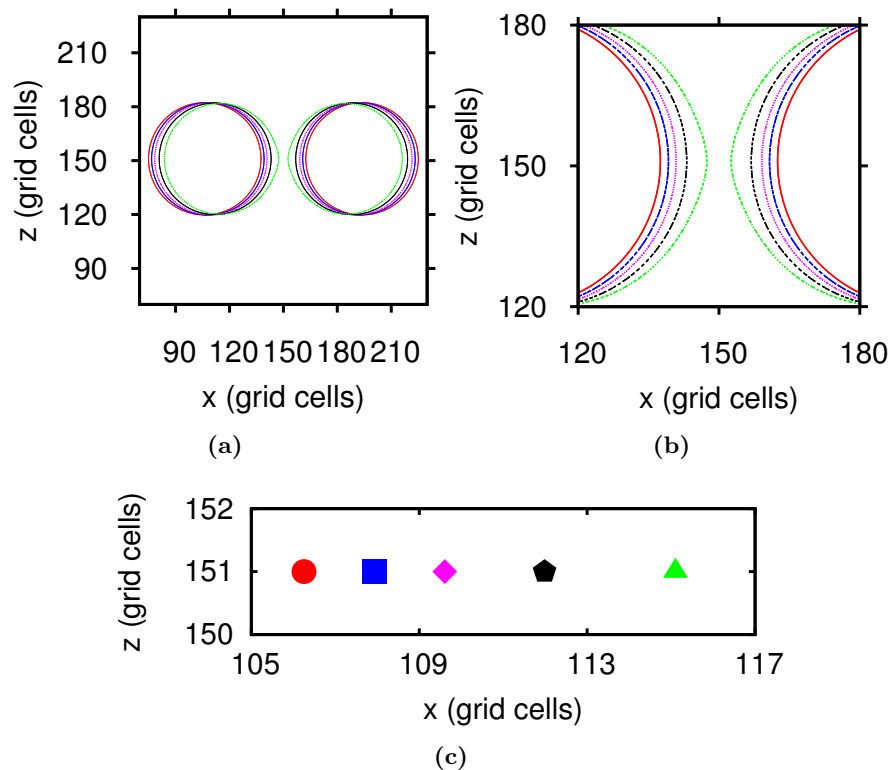


Figure 7.8: “Transition from motion to coalescence: (a) shows the trace of the line with a value of 0.5, of each droplets, when the initial distance between the two droplets is 30 grid cells and $M = 1000$. The solid red, dashed blue, dotted pink, dot dashed black and dot dot dashed green lines correspond to the dimensionless time of 8760, 27760, 41760, 52760 and 55160, respectively. (b) is a zoom in figure of (a). (c) shows the barycenter of the left droplet at the dimensionless time of 8760, 27760, 41760, 52760 and 55160, represented by the red circle, blue square, pink lozenge, black pentagon and green triangle, respectively.” [48]

7.2.3 Coalescence

“In this section, we investigate the effect of capillary convection on the coalescence process. Initially, we put two droplets of L_2 phase in contact and inside the L_1 matrix, with a distance being less than the interface width, as illustrated in Fig. 7.9 (a). The mole fraction of Fe in the droplets and in the matrix are 0.2868 and 0.7132, respectively.” [48]

“With time, the two droplets join to reduce the total surface area, causing a concave region where two droplets contact each other. This, subsequently, induces a convection along the surface of each droplets due to the difference in the interfacial concentration.” [48]

“We show the coalescing morphology at the initial stage in Fig. 7.9 (a) ¹⁶. The path of convection and stream lines at the time of 3220 for $M = 10$ are given in Fig. 7.9 (b) and (c), respectively. The isolines for pressure caused by capillary flow corresponding

¹⁶Fig. 7.8 (a) and (b) are visualized by using the post-processing tool which is developed by M.S.

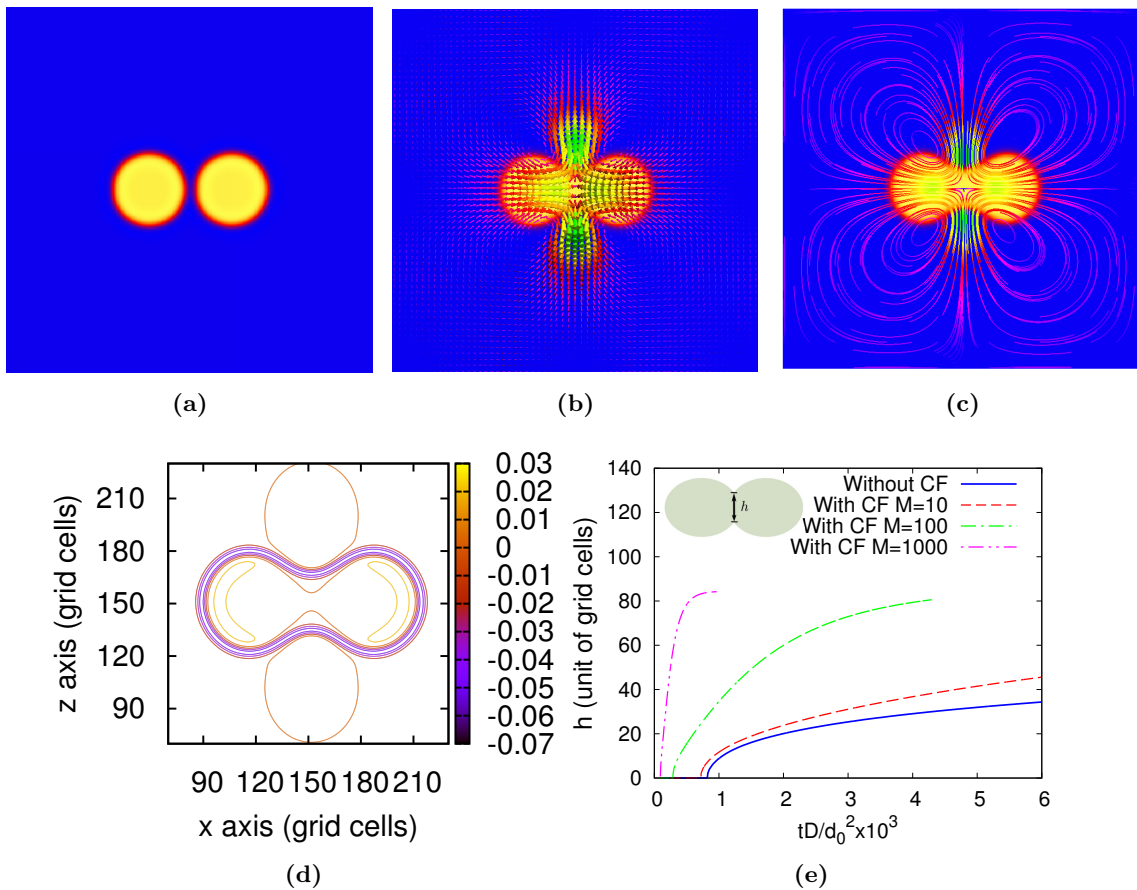


Figure 7.9: “Coalescence of droplets assisted by capillary convection in monotectic systems: (a) is the initial morphology for the simulation where two droplets are 8 grid cells apart from each other, (b) shows the coalescing morphology with the path of capillary convection at a dimensionless time of 3220, (c) illustrates the stream line which results from capillary convection, (d) displays the isolines of pressure caused by capillary convection corresponding to the state of (b), and (e) draws the height of the neck varying with time in the cases of including capillary flow at different dimensionless numbers and not considering capillary convection, containing the schematic figure for comprehending where we measure the height of the neck.” [48]

to the state in (b) are plotted in Fig. 7.9 (d). We take the following route to obtain the pressure profile. We first solve the Navier-Stokes equation with capillary tensor and then substitute the results into the Eq. (3.12) because of the assumption of incompressible flow, which results in a Poisson equation for the pressure. By employing SOR iteration to solve the Poisson equation, we thus obtain the pressure profile resulting from convection. For a detailed mathematical procedure, one may refer to Ref. [58].” [48]

“To compare the coalescing process both in the presence and absence of capillary flow, we calculate the height of neck as a function of time, as illustrated in Fig. 7.9 (e). We include a schematic figure inside for better understanding of where we exactly measure the height of the neck. The dashed red, dot dashed green and dot dot dashed pink lines

represent the cases with capillary flow for $M = 10, 100$ and 1000 , respectively. The solid blue line depicts the process only governed by diffusion. It shows that the interfaces of the two droplets get in touch with each other earlier and the height of the neck evolves faster while considering capillary flow. Moreover, the increase in dimensionless number from 10 to 1000 substantially raises the rate of coalescence.” [48]

7.2.4 Coarsening

“Two droplets with different sizes and at a distance larger than the interface width undergo an Oswald ripening process due to the Gibbs-Thomson effect. To capture the effect of capillary flow on the coarsening process, we perform two sets of simulation: (a) two droplets, one with diameter of 60 grid cells and the other of 30 grid cells, with a distance of 30 grid cells, (b) the same as (a) except that the diameter of the smaller droplet is 40 grid cells. During the coarsening process, the bigger droplet grows, whereas the smaller one shrinks and tends to vanish.” [48]

“To address the effect of capillary flow, we plot the radius of the bigger droplets as a function of time in two sets of simulation, both with and without capillary flow, as shown in Fig. 7.10. We observe that the evolution velocity of case (a) is faster than that of case (b). This is due to the fact that in case (a) the driving force, which is proportional to curvature difference of the two droplets, is higher than that of case (b). Moreover, in each case, the coarsening velocity of the two droplets is relatively unaffected, upon incorporation of capillary flow, although increasing the dimensionless number M has a very weak enhancement of the velocity. We therefore conclude that capillary flow has no obvious effect on the mass transfer between the two droplets and thus coarsening process is not likely to be influenced by capillary flow.” [48]

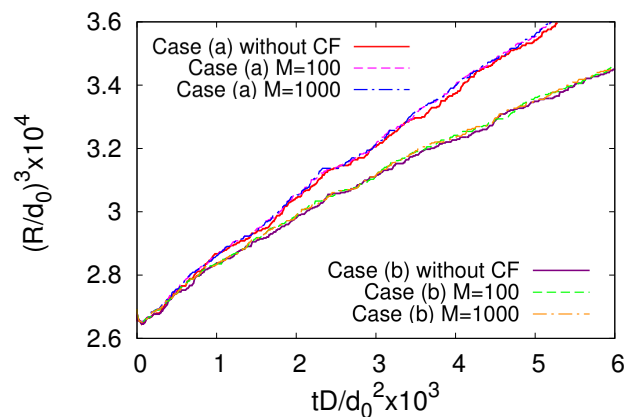


Figure 7.10: “The radius of droplets as a function of time during coarsening process: the solid red (upper) and solid brown (down) lines show the case (a) and (b) without capillary flow, respectively, the dashed pink (upper) and dashed green (down) lines depict the case (a) and (b) with capillary flow at $M = 100$, respectively, the dotted blue (upper) and dotted orange (down) lines illustrate the case (a) and (b) with capillary flow at $M = 1000$, respectively.” [48]

7.2.5 Phase separation affected by capillary flow in Fe-50 at% Sn alloy

“In this section, phase separation influenced by capillary convection in Fe-50 at% Sn alloy is investigated. The composition of the alloy is inside the region of the spinodal region, where the primary liquid is unstable and in the presence of fluctuations decomposes into two liquids differing only by concentrations. Perturbations in the form of conserved noise are introduced to initiate spinodal decomposition. Based on these conditions, simulations are performed under isothermal condition at a dimensionless temperature of 0.8, corresponding to a dimensional value of 1122.4 K. The temperature of the spinodal decomposition at this composition of Fe-50 at% Sn is 1781 K and the monotectic temperature of the system is 1403 K.” [48]

“At the early stage of phase separation, an incipient interface forms between the two phases and the non-uniform concentration distribution along this interface results in convection. The concentration field together with the fluid flow profile at a simulation time of 3175 is displayed in Fig. 7.11 (b). When the concave and convex interfaces are near each other, i.e., a larger curvature difference, the convection becomes stronger. The phase separation morphology without capillary flow at the same time is illustrated in Fig. 7.11 (a). A comparison between these two morphologies reveals that the capillary flow accelerates the evolution process of phase separation in Fe-50 at% Sn alloy. Quantitative analysis is given below by making a comparison between the evolution modes in these two cases.” [48]

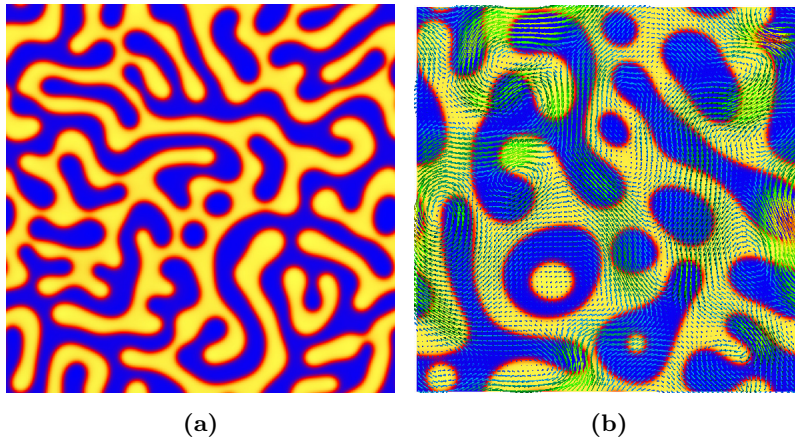


Figure 7.11: “Phase separation morphologies in Fe-50 at% Sn alloy without capillary flow (a), and with capillary flow (b) ($M = 10$) both at time $tD/d_0^2 = 3175$.” [48]

“If an isotropic system is assumed, we can make a circular approximation to the square simulation domain and use the circular averaged concentration, which is a function of the radial distance, to evaluate the spatial periodicity in the phase separation process

by writing the radial distribution of the concentration as

$$C(r) = \frac{1}{N_r} \sum_{R, |R|=r} (c(r) - c_0),$$

where $c(r)$ is the concentration at each radius r , N_r is the number of the points with radius r .”[48]

“In order to identify the individual modes, distinguished by the wave numbers in reciprocal space, we perform a Fourier transformation of the circular averaged concentration as

$$F(\mathbf{k}) = \int dr C(r) e^{-i\mathbf{k}\cdot\mathbf{r}}. \quad (7.39)$$

The intensities of $F(\mathbf{k})$ with respect to the wave number at the simulation time of

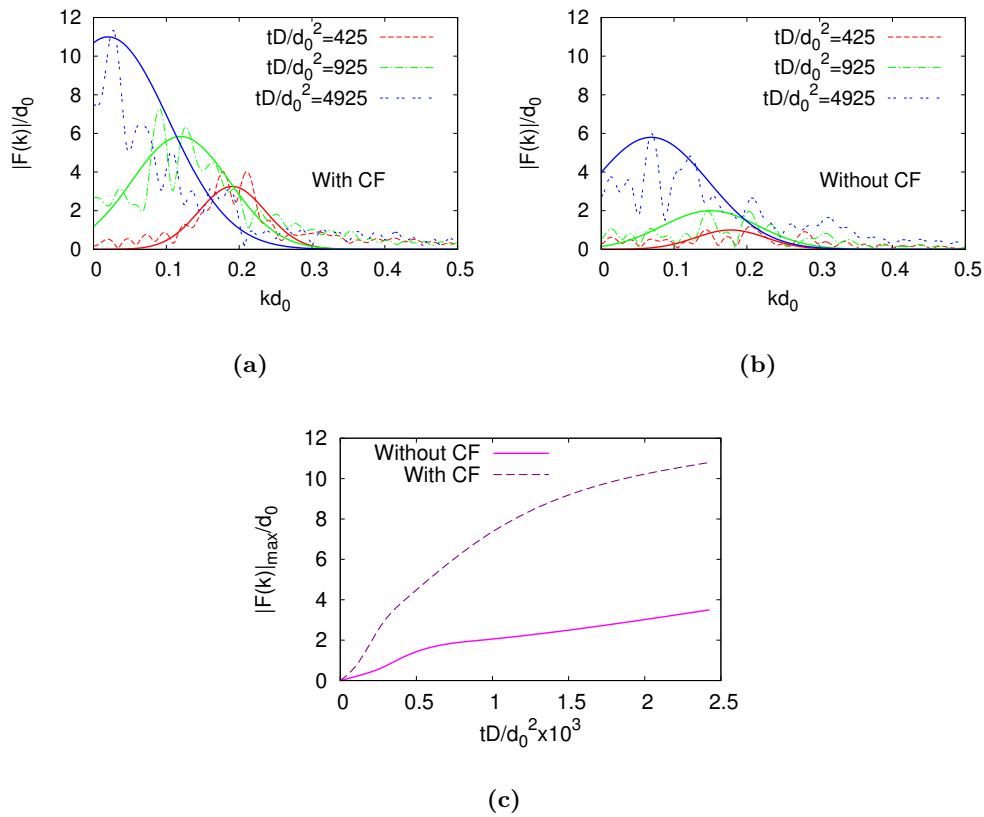


Figure 7.12: “The effect of capillary flow on the X-ray spectra in Fe-50 at% Sn alloy: (a) and (b) shows the intensity, calculated from Eq. (7.39), as a function of the wave number in the cases with and without capillary flow, respectively. The dashed red, dot dashed green and dotted blue lines are for simulation time of 425, 925 and 4925, respectively. The solid lines correspond to the fitting curves, (c) depicts the value of the peak of the spectra as a function of time with and without capillary flow, represented by the dashed purple and solid pink lines, respectively.”[48]

425, 925 and 4925 with and without capillary flow, are shown in Fig. 7.12 (a) and (b), respectively. With time, the peak of $|F(\mathbf{k})|$ shifts towards the long-wave-length direction, which is accordance with the analytical results obtained by Langer [81]. However, if we compare the peak of $|F(\mathbf{k})|$ at the same time with and without capillary flow, we find that the value is higher in the former case. In addition, in Fig. 7.12 (c) we plot the amplitude of the spectra as a function of time with and without capillary flow, respectively. It shows that capillary flow dramatically accelerates the evolution process.” [48]

7.2.6 Phase separation influenced by capillary flow in Fe-40 at% Sn alloy

“In this section, we investigate the phase separation in hyper-monotectic Fe-40 at% Sn alloy influenced by capillary flow. Simulation conditions are the same as that in Section 7.2.5, initializing phase separation by using a conserved noise, which is switched off after a short evolution. The temperature of the spinodal decomposition at this composition is 1529.9 K and the simulations are performed at a dimensionless temperature of 0.8 relating to a dimensional value of 1122.4 K.” [48]

“The morphologies resulting from spinodal decomposition at a simulation time of 2475 are shown in Fig. 7.13 (a) and (b) ¹⁷, where figure (a) refers to the case without capillary flow and figure (b) shows the snapshot of phase separation coupled with capillary flow. Compared with the bi-continuous microstructure resulted from the phase-separation of Fe-50 at %Sn alloy shown in Fig. 7.11, a structure composed of droplets forms at Fe-40 at% Sn alloy. Moreover, the path of fluid flow caused by the non-uniform concentration gradient is illustrated in Fig. 7.13 (b). Notably, when two droplets begin to coalesce, the fluid flow around the contact point becomes much stronger than the other places. This is due to the fact that the negative curvature occurs at the neck of two droplets during the process of coalescence, which causes a larger difference in concentration gradient.” [48]

“Fig. 7.13 (c) shows the cube of the average radius of droplets as a function of time. The solid red and dot dashed blue lines represent the cases with and without capillary flow, respectively, and the dashed green and dot dot dashed pink lines correspond to the linear fits. From the figure we conclude, without capillary flow the cube of average radius changes linearly with time during the evolution process, as predicted by Lifshitz and Slyozov [82] and simulation [83].” [48]

“When capillary flow is considered, the average radius of droplets is bigger than that not considering capillary flow, and the average radius as a function of time can be divided into three regimes: I (from simulation time 0 to 5000), the average radius increases rapidly due to the fact that there is a large number of droplets with short distance between each other where capillary flow has a substantial accelerating effect and this

¹⁷Fig. 7.12 (a) and(b) are visualized by using the post-processing tool, which is developed by M.S.

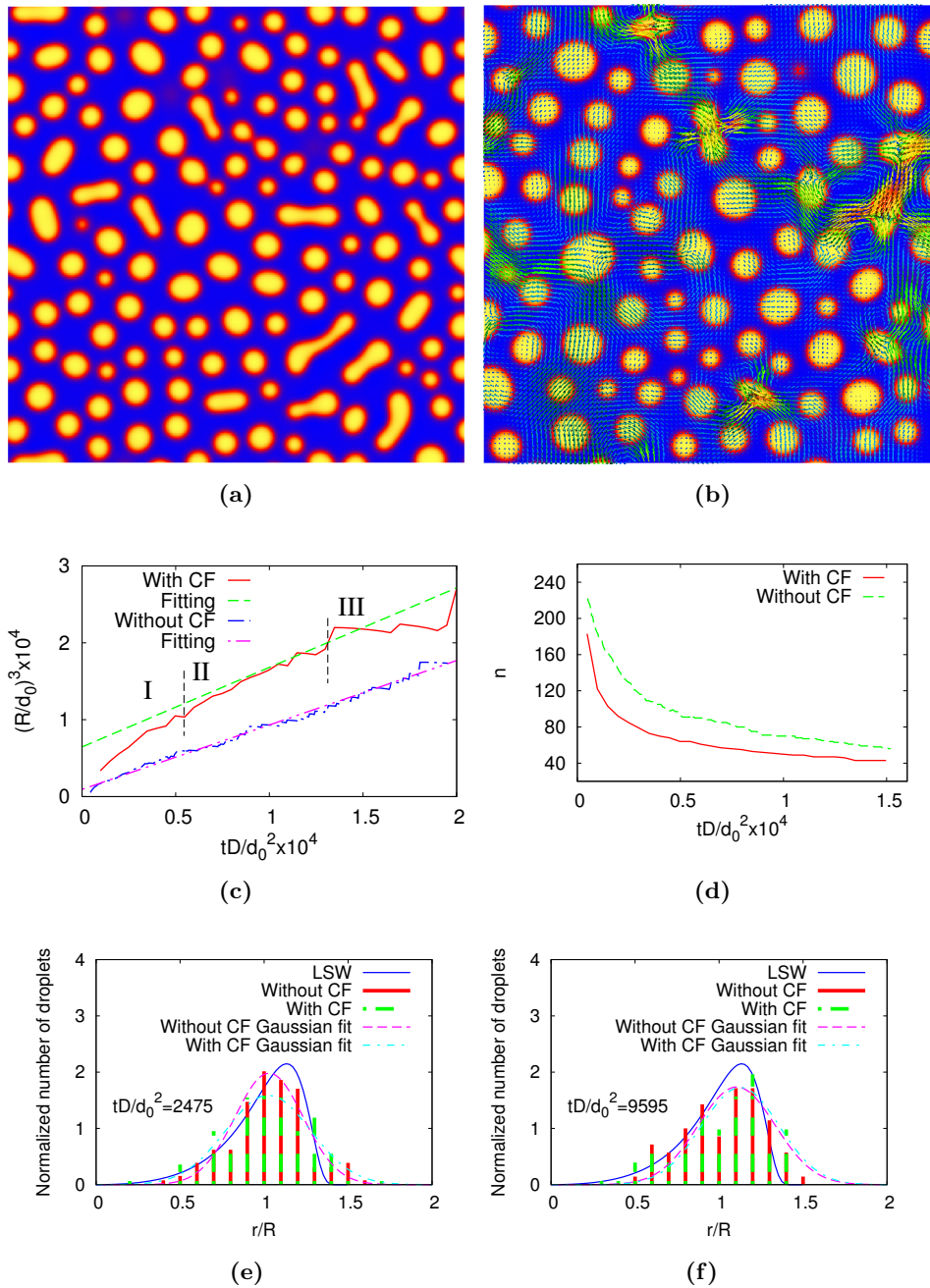


Figure 7.13: “Phase separation morphologies in Fe-40 at% Sn alloy without capillary flow (a), and with capillary flow (b) ($M = 10$), the average radius and number of droplets varying with time are shown in (c) and (d), respectively. Bar chart diagram (e) and (f) show the size distribution of droplets at simulation time of 2475 and 9595, respectively, in comparison with the LSW theory.” [48]

process is accordance with the simulation results in Ref. [83]¹⁸, in which they got a $R^2 \sim t$ relation; II (from time 5000 to 15000), the capillary flow is weakened when the number of droplets decreases and the cube of the average radius of droplets changes

¹⁸B.N. suggested to compare the results with the work of Diepers et al. and the discussion for the dynamic behavior in regime I is partially contributed by B.N.

linearly with time; III (after time 15000), the number of droplets is fairly less, resulting in a non-smooth increase in average radius with time. In addition, Fig. 7.13 (d) shows the the number of droplets as a function of time for the cases with and without capillary flow. From the curves in Fig. 7.13 (d), we can see that the number of droplets considering capillary flow is less than that without capillary flow. The gap between the two curves is mainly due to the initial accelerating effect of capillary flow on the coalescence of droplets, which corresponds to the regime I in Fig. 7.13 (c).” [48]

“Fig. 7.13 (e) and (f) present the size distribution of droplets at the simulation time of 2475 and 9595, respectively. In each figure, the thick solid red and thick dashed green bars represent the case without and with capillary flow, respectively. The short dashed pink and dot dashed cyan lines represent the Gaussian fits without and with capillary flow, respectively. The solid blue line is plotted to show the LSW size distribution according to Ref. [82, 84] as¹⁹

$$g(r) = \frac{4}{9} \left(\frac{r}{R}\right)^2 \left(\frac{3}{3 + \frac{r}{R}}\right)^{7/3} \left(\frac{1.5}{1.5 - \frac{r}{R}}\right)^{11/3} \exp\left(\frac{\frac{r}{R}}{\frac{r}{R} - 1.5}\right),$$

where r is the radius of droplet, and R denotes the mean radius over all droplets. Fig. 7.13 (e) shows that capillary flow causes a broader and flatter size distribution than that obtained without capillary flow, which is similar to the results obtained by Tegze et al. [85]. With time, the size distribution of droplets in the two cases tends to overlap each other, as shown in Fig. 7.13 (f). A comparison with the LSW theory shows that the size distributions are broader with smaller amplitude for both the cases.

¹⁹R.M. suggested to compare the present results with the LSW theory.

²⁰A.C. and R.M. suggested to compare the size distribution of droplets of equivalent statistical states and the discussions for Fig. 7. 13 are partially contributed by A.C. and R.M.

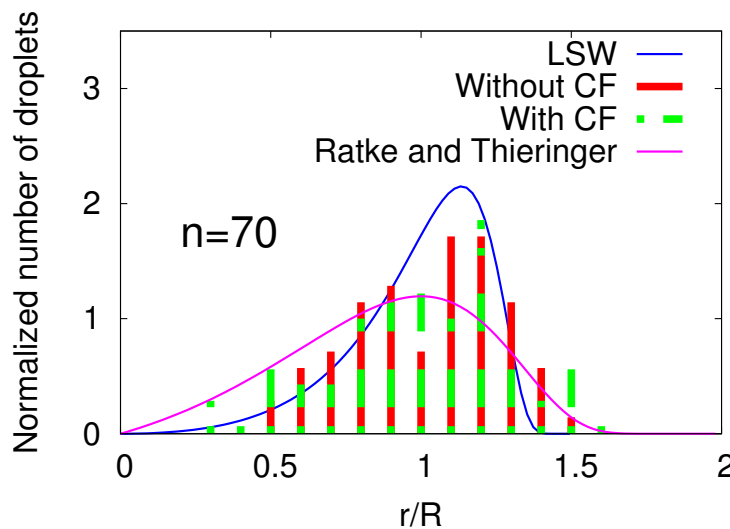


Figure 7.14: “The effect of capillary flow on the size distribution of droplets corresponding to the equivalent statistical states.” [48]

This is due to the fact that LSW is valid for predicting the size distribution for dilute alloys [82, 84]. For high volume fraction regime, the size distribution broadens and the amplitude decreases [86–88].” [48]

“Fig. 7.14 shows the effect of capillary flow on the size distribution of droplets at equivalent statistical states (equal number of droplets). In the figure, we compare the size distributions at time 9595 (without capillary flow) and at time 3975 (with capillary flow), which are located in the linear regime in Fig. 7.13 (c). In both cases the number of droplets is 70. It shows that the case considering capillary flow has a broader size distribution and the peak shifts towards the larger droplet direction. Moreover, the analytical result considering capillary flow, obtained by Ratke and Thieringer [89], is shown in the figure by the dashed pink line. It is observed, that the size distribution of the droplets at larger and smaller size region tends to the analytical results achieved by Ratke et al., whereas the LSW curve fits better around the area of $r/R = 1$.” [48]

Chapter 8

Conclusion and outlook

8.1 Conclusion and remarks

I have shown that the morphological stability criterion for perturbed jets is addressed by two parts:

$$\lambda_{\text{crit}} = \begin{cases} 2\pi\sqrt{R_0^2 - a^2}, & 0 < a/R_0 < \sqrt{\frac{4\pi^2 - 6}{4\pi^2 + 3}}, \\ \sqrt{6R_0^2 + 3a^2}, & \sqrt{\frac{4\pi^2 - 6}{4\pi^2 + 3}} \leq a/R_0 < 1. \end{cases}$$

Besides the fundamental significance, I am convinced that the present theory can serve as a useful reference in a wide variety of practical applications. In directional solidifications [90–93], rod-shaped phases are usually formed behind the front of the solid-liquid interface. The rod phase simultaneously breaks up into a chain of spheres and the size of the particles affects the mechanical and electrical properties of the materials. In nanotechnology [94–97], metallic nanowires are usually used as conductors or semiconductors and the morphological stability is of crucial importance, especially at elevated temperature where the surface diffusivity is increased. In medical science and cosmetics, the separation of a fluid column into a line of droplets is extensively observed [98–106] and may be predicted more accurately by the present theory.

Experimentally, the distance between the resulted droplets is likely to be the wavelength where the maximum velocity of the detachment takes place. According to the linear stability analysis of Rayleigh, the maximum growth rate occurs at $\lambda_m = \sqrt{2}\lambda_{\text{crit}}$ [2], as reviewed in section 2.2.2. The derivation of the wavelength λ_m is based on the Lagrange's method using the potential energy of Eq. (2.6) and kinetic energy K of inviscid fluid. However, the potential energy of Eq. (2.6) is based on the binomial series approximation for tiny perturbations. Hence, the prevailing wavelength λ_m has to be amended for the general case where the amplitude of the perturbation is large.

The second topic that was investigated is the capillary wave at a fluid-fluid interface. By using a Fourier analysis, I have shown that the interfacial wave is induced by the

oscillatory modes of the capillary flow. I have addressed a critical dimensionless number M , above which the oscillatory modes are able to occur.

In the third part of the thesis, I have analytically and numerically studied the motion of two droplets driven by capillary flow. For small capillary numbers, the interface is assumed to be non-deformable and the motion of the droplets thus can be analyzed in the bipolar coordinate. The stream lines from the Cahn-Hilliard-Navier-Stokes model are qualitatively consistent with the analysis in the bipolar coordinate. The effect of capillary flow on the coalescence as well as the coarsening processes of two droplets is further explored. It has been found that the capillary flow has a weaker effect on the coarsening process, whereas the speed of coalescence is significantly enhanced when the capillary flow is considered.

Based on the investigation of the capillary effect on the interaction of two droplets, I examine the motion of multi-droplets in the process of spinodal decomposition. I find that the capillary flow speeds up the spinodal decomposition and the mean size of the droplets is bigger than the case without capillary flow. Moreover, in comparison with the LSW theory, the droplets have a broader size distribution.

8.2 Future directions

8.2.1 Irregular perturbation

As the classic work of Rayleigh, a single-wavelength perturbation $r = R_0 + a \cos kx$ is considered in the present work. In reality, perturbations are likely to be stochastically generated and the perturbed jet can be expressed in a more general form

$$r = R_0 + \sum_{n=1}^{\infty} a_n \cos nkx, \quad (8.1)$$

where a_n is the Fourier coefficient of the n -th order perturbation.

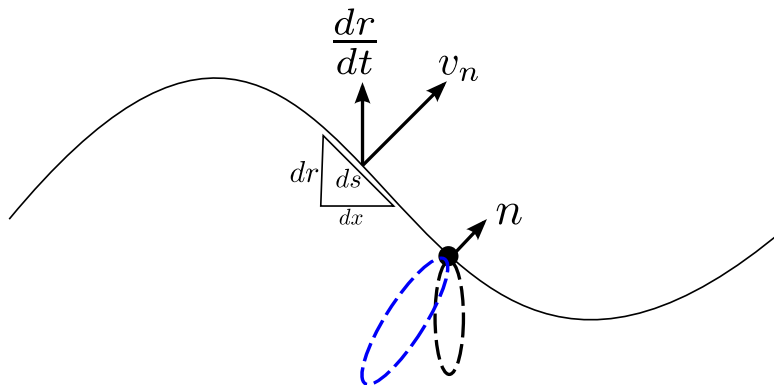


Figure 8.1: Sketch of a perturbed jet.

As sketched in Fig. 8.1, the normal velocity v_n correlates to the evolution rate of the radius $\partial_t r$ as

$$v_n = \partial_t r \sqrt{1 + (\partial_x r)^2} = \left(\partial_t R_0 + \sum_{n=1}^{\infty} \partial_t a_n \cos nkx \right) \sqrt{1 + (\partial_x r)^2}. \quad (8.2)$$

Using the relationship, $ds^2 = dr^2 + dx^2$ (see Fig. 8.1), the surface Laplace operator is expressed as $\frac{d^2}{ds^2} = \frac{1}{\sqrt{1+(\partial_x r)^2}} \frac{d}{dx} \left(\frac{1}{\sqrt{1+(\partial_x r)^2}} \frac{d}{dx} \right)$ and the surface Laplace of the mean curvature reads

$$\frac{d^2 \kappa}{ds^2} = \frac{1}{\sqrt{1 + (\partial_x r)^2}} \partial_x \left(\frac{1}{\sqrt{1 + (\partial_x r)^2}} \partial_x \kappa \right). \quad (8.3)$$

The evolution equation of surface diffusion is rearranged as

$$\partial_t R_0 + \partial_t a_1 \cos kx + \partial_t a_2 \cos 2kx + \dots = \frac{1}{1 + (\partial_x r)^2} \partial_x \left(\frac{1}{\sqrt{1 + (\partial_x r)^2}} \partial_x \kappa \right). \quad (8.4)$$

A future work is to analyze the above evolution equation to obtain the dynamic equations for the coefficients a_n . The critical setup for the breakup can be derived by the condition of whether the leading amplitude a_1 increases or decreases with time.

8.2.2 Satellite mini droplets

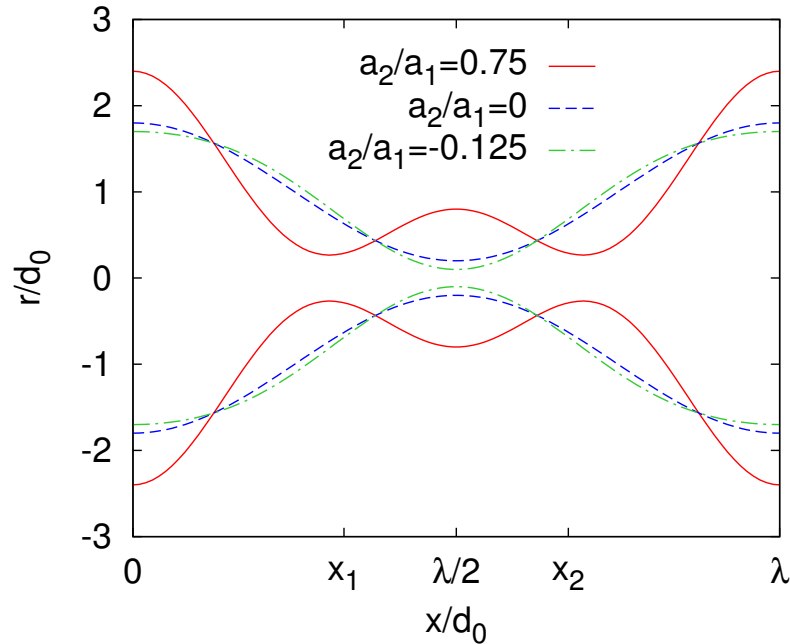


Figure 8.2: Illustration for jets $r = R_0 + a_1 \cos kx + a_2 \cos 2kx$ with different ratios of a_2/a_1 .

In experiments, we often observe breakups with satellite mini droplets. An illustration for the reason of the creation of satellite mini droplets is shown in Fig. 8.2, which depicts

jets $r = R_0 + a_1 \cos kx + a_2 \cos 2kx$ for different ratios of a_2/a_1 . For ratios of $a_2/a_1 = 0$ (the dashed line) and $a_2/a_1 = -0.125$ (the dot-dashed line), the surface of the jet is monotonic from the crest to the trough and the jet tends to break up at the trough of the wave ($x = \lambda/2$) when the surface flux is from the trough to the crest. For a positive ratio of a_2/a_1 (the solid line), two additional extrema points appear at x_1 and x_2 . If the secondary amplitude further increases with time, the radial curvature ($\approx 1/r$) becomes the dominating curvature and the mean curvatures at x_1 and x_2 are greater than the values at other places. Due to the surface flux $\mathbf{J} = -\nabla_s \kappa$, the breakup takes place at x_1 and x_2 , forming a daughter droplet between the main droplet. So, the formation of satellite mini droplets is due to an increase of the higher order term a_2 in the Fourier series. To carry out such a non-linear stability analysis to derive the dynamic equation for a_2 could be a future work.

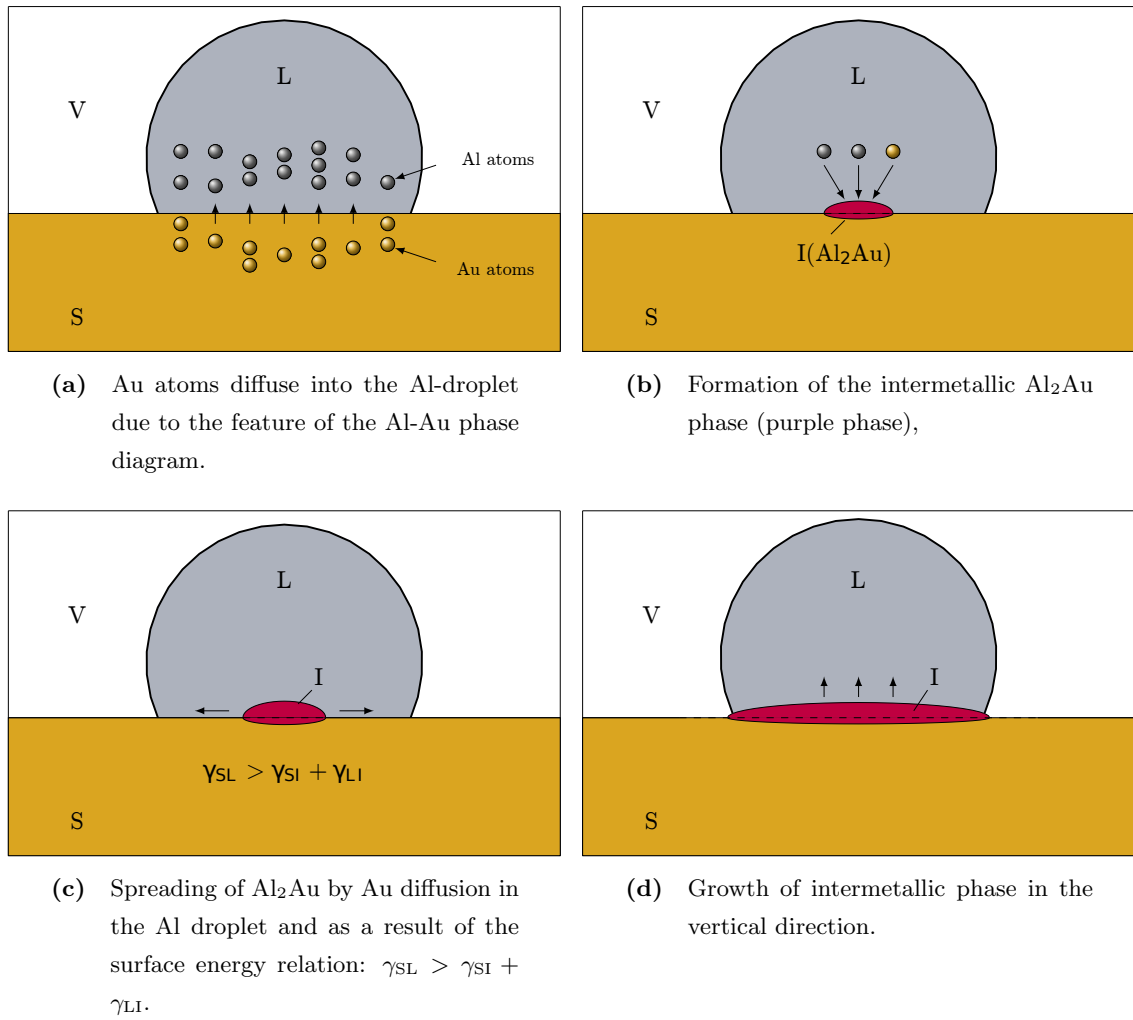
8.2.3 Other applications of the numerical models

The multiphase Allen-Cahn model can be used for the grain growth [107] and wetting phenomena [108] and, if coupled with the multicomponent diffusion equation, it can be employed to study phase transformation in the solidification process, formation of intermetallic phases, etc. An example which has been published in Ref. [109] is briefly depicted in the following.

“Fig. 8.3 schematically illustrates the mechanism for the formation of the intermetallic phase Al_2Au in the Al-Au system. From the binary phase diagram of Al-Au, the equilibrium mole fractions of Au in liquid and solid are relative high. While placing an Al-liquid droplet on an Au-solid substrate, the composition of Au in liquid tends to approach the equilibrium mole fraction. This is achieved by a diffusion of Au into the Al-liquid, as schematically illustrated in Fig. 8.3 (a).” [109]

“Thereafter, the Al and Au combines with a ratio of 2, forming the intermetallic phase Al_2Au , as shown in Fig. 8.3 (b). Due to the surface energy relation: $\gamma_{\text{SL}} > \gamma_{\text{SI}} + \gamma_{\text{LI}}$, the triple point of solid-liquid-intermetallic phase is not stable, resulting in the growth of the intermetallic phase in the horizontal direction, as illustrated in Fig. 8.3 (c). During the spreading of the intermetallic phase, the Au atoms constantly diffuse into the Al-liquid, which provides the source for the later growth of the intermetallic phase in the vertical direction.” [109]

“When the two triple points SIV (Solid-Intermetallic-Vacuum) and LIV (Liquid-Intermetallic-Vacuum) are established, the spreading of the intermetallic phase in the horizontal direction stops. The intermetallic phase then grows in the vertical direction, increasing its thickness, as illustrated in Fig. 8.3 (d). At this stage, the liquid is no longer in contact with the solid. Since the diffusivity of Au in liquid Al is greater than the one in solid Au, the intermetallic phase grows into the liquid droplet. The required Au for the



(a) Au atoms diffuse into the Al-droplet due to the feature of the Al-Au phase diagram.

(b) Formation of the intermetallic Al_2Au phase (purple phase),

(c) Spreading of Al_2Au by Au diffusion in the Al droplet and as a result of the surface energy relation: $\gamma_{SL} > \gamma_{SI} + \gamma_{LI}$.

(d) Growth of intermetallic phase in the vertical direction.

Figure 8.3: “(a) Schematic illustration of a liquid droplet L (Al) on top of a substrate S (Au) surrounded by vacuum V . (b)-(d) Formation and growth of the intermetallic phase I (Al_2Au).” [109]

growth of the intermetallic phase is provided from the stages shown in Fig. 8.3 (a), (b) and (c).” [109]

“Fig. 8.4 shows a temporal evolution of the intermetallic phase Al_2Au computed by the phase-field model. The yellow, purple and gray regions represent Au-solid substrate, intermetallic phase Al_2Au and Al-liquid droplet, respectively. Fig. 8.4 (a) corresponds to an initial filling where the intermetallic phase Al_2Au is set as a small nucleus inside the Al droplet. Due to the relation that $\gamma_{SL} > \gamma_{SI} + \gamma_{LI}$, the intermetallic phase propagates along the solid-liquid interface and spreads in the horizontal direction, as shown in Fig. 8.4 (b). When the solid-liquid interface is completely covered, the intermetallic phase grows in the vertical direction towards the Al liquid and its thickness increases, as depicted in Fig. 8.4 (c).” [109]

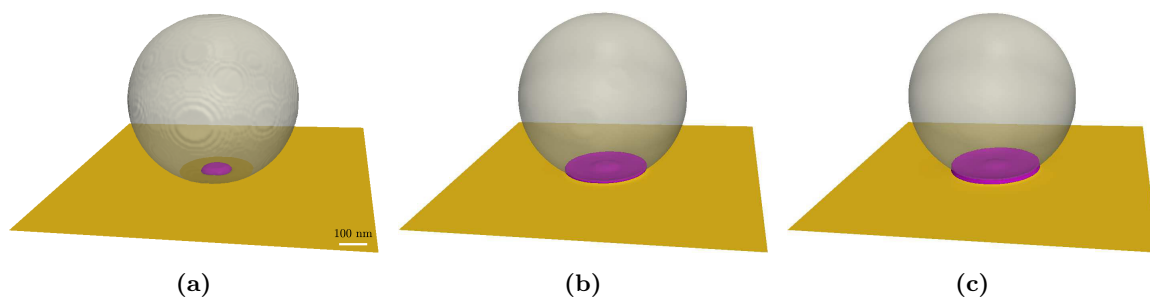


Figure 8.4: “Time evolution of the intermetallic phase Al_2Au from a phase-field simulation: (a) Earlier stage of the intermetallic phase Al_2Au inside the Al-droplet, (b) spreading of the intermetallic phase in the horizontal direction, (c) growth of the intermetallic phase grows in the vertical direction.” [109]

Appendix A

Capillary tensor

“We perform a transformation to the coordinates x and field variables $c(x)$ as

$$\xi^\mu = x^\mu + w_\nu^\mu x^\nu + a^\mu \equiv x^\mu + \kappa^\mu(x), \quad (\text{A.1})$$

$$\phi(\xi) = c(x) + \delta c(x), \quad (\text{A.2})$$

where a^μ represents a space time translation, w_ν^μ is a Lorentz transformation and antisymmetry. ξ is the new coordinate and $\phi(\xi)$ is the new field variable after transformation. According to Noether’s theorem [50], a specific transformation of the coordinates and field variables does not change the action

$$\delta S = \int_{\Omega'} \mathcal{L}(\phi(\xi), \partial'_\mu \phi(\xi)) d\Omega' - \int_{\Omega} \mathcal{L}(c(x), \partial_\mu c(x)) d\Omega = 0. \quad (\text{A.3})$$

For a scalar field $\phi(\xi) = c(x)$ and using $d\Omega' = d\Omega$, we write

$$\int_{\Omega'} \mathcal{L}(\phi(\xi), \phi'_{,\mu}(\xi)) d\Omega' = \int_{\Omega} \mathcal{L}(c(x), \partial'_\mu c(x)) d\Omega. \quad (\text{A.4})$$

Combining with Eq. (A.1), we obtain

$$\partial'_\mu = \frac{\partial x^\nu}{\partial \xi^\mu} \partial_\nu = \partial_\mu - (\partial_\mu \kappa^\nu) \partial_\nu.$$

Substituting the above expression in Eq. (A.4) and expanding it, we get

$$\int_{\Omega} \mathcal{L}(c, [\partial_\mu - (\partial_\mu \kappa^\nu) \partial_\nu] c) d\Omega = \int_{\Omega} \mathcal{L}(c, \partial_\mu c) d\Omega - \int_{\Omega} \frac{\partial \mathcal{L}}{\partial(\partial_\mu c)} (\partial_\mu \kappa^\nu) \partial_\nu c d\Omega. \quad (\text{A.5})$$

The second term in Eq. (A.5) can be written as

$$\frac{\partial \mathcal{L}}{\partial(\partial_\mu c)} (\partial_\mu \kappa^\nu) \partial_\nu c = \partial_\mu \left(\frac{\partial \mathcal{L}}{\partial(\partial_\mu c)} \kappa^\nu \partial_\nu c \right) - \kappa^\nu \partial_\mu \left(\frac{\partial \mathcal{L}}{\partial(\partial_\mu c)} \partial_\nu c \right). \quad (\text{A.6})$$

The last term can be rewritten as by using Euler-Lagrange equation $\frac{\partial \mathcal{L}}{\partial c} = \partial_\mu \frac{\partial \mathcal{L}}{\partial (\partial_\mu c)}$

$$\partial_\nu \mathcal{L} = \partial_\mu \left(\frac{\partial \mathcal{L}}{\partial (\partial_\mu c)} \partial_\nu c \right).$$

Thus, Eq. (A.3) reads as when we use $\partial_\nu \kappa^\nu = 0$ due to the antisymmetry of $w_{\mu\nu}$

$$\delta S = - \int_\Omega \partial_\mu \left(\frac{\partial \mathcal{L}}{\partial (\partial_\mu c)} \kappa^\nu \partial_\nu c - \kappa^\mu \mathcal{L} \right) d\Omega.$$

Since, the action is assumed to be invariant under the transformation in Eq. (A.1) and Eq. (A.2) for arbitrary volumes Ω , we have a conserved current, $\partial_\mu \Theta^\mu = 0$, with:

$$\Theta^\mu = \frac{\partial \mathcal{L}}{\partial (\partial_\mu c)} \kappa^\nu \partial_\nu c - \kappa^\mu \mathcal{L}.$$

By writing

$$\Theta_\nu^\mu = \frac{\partial \mathcal{L}}{\partial (\partial_\mu c)} \partial_\nu c - \delta_\nu^\mu \mathcal{L},$$

our conservation law $\partial_\mu \Theta^\mu = 0$ now implies

$$\partial_\mu \Theta_\nu^\mu = 0.$$

”[48]

Appendix B

Surface Laplacian evaluation

For a graph $z = S(x, y)$ or $F(x, y, z) := z - S(x, y) = 0$, the norm vector is defined as $\mathbf{n} = \nabla F / |\nabla F|$ and the mean curvature is calculated according to

$$\kappa(x, y, z) = -\frac{1}{2} \nabla \cdot \mathbf{n}.$$

The surface gradient of the mean curvature reads

$$\nabla_s \kappa = \nabla \kappa - (\mathbf{n} \cdot \nabla \kappa) \mathbf{n}.$$

The surface Laplacian is evaluated as

$$\nabla_s^2 \kappa = \text{Tr}[\nabla(\nabla_s \kappa)(\mathbf{1} - \mathbf{n} \otimes \mathbf{n})].$$

At the crest and trough of the wave, we readily have $\mathbf{n} \cdot \nabla \kappa = 0$. The comparison of the surface Laplacian $\nabla_s^2 \kappa|_{\text{crest}} = \nabla_s^2 \kappa|_{\text{trough}}$ turns to the evaluation of the second derivative of the mean curvature

$$0 = \nabla_s^2 \kappa|_{\text{crest}} - \nabla_s^2 \kappa|_{\text{trough}} = -2ak^4 - 6a^3k^6 + \frac{ak^2}{(R_0 + a)^2} + \frac{ak^2}{(R_0 - a)^2} - \frac{a^2k^4}{(R_0 + a)} + \frac{a^2k^4}{(R_0 - a)}.$$

The obtained roots are as follows:

- $a = 0$, rejected;
- $a = R_0 \sqrt{1 - (\lambda/2\pi R_0)^2}$, accepted;
- $a = -R_0 \sqrt{1 - (\lambda/2\pi R_0)^2}$, rejected for negative values;
- $a = \pm \frac{\sqrt{6}}{12\pi} \sqrt{\lambda^2 + 12\pi^2 R_0^2 + \sqrt{(\lambda^2 + 12\pi^2 R_0^2)^2 + 48\pi^2 R_0^2}}$, rejected for $|a| > R_0$;
- $a = \pm \frac{\sqrt{6}}{12\pi} \sqrt{\lambda^2 + 12\pi^2 R_0^2 - \sqrt{(\lambda^2 + 12\pi^2 R_0^2)^2 + 48\pi^2 R_0^2}}$, rejected for $a \in \mathbb{C}/\mathbb{R}$.

The equality $a = R_0\sqrt{1 - (\lambda/2\pi R_0)^2}$ can be reformulated as $\lambda = 2\pi\sqrt{R_0^2 - a^2}$.

Appendix C

Coefficients

“

$$\begin{aligned}g_{-1}^{(\alpha,n)} &= n \sinh(n - 1/2)\alpha, \\g_0^{(\alpha,n)} &= (\sinh \alpha + 2q\varsigma) \cosh(n + 1/2)\alpha + \\&\quad (2n + 1) \cosh \alpha \sinh(n + 1/2)\alpha, \\g_1^{(\alpha,n)} &= (n + 1) \sinh(n + 3/2)\alpha, \\h_{-1}^{(\alpha,n)} &= n \cosh(n - 1/2)\alpha, \\h_0^{(\alpha,n)} &= (\sinh \alpha + 2q\varsigma) \sinh(n + 1/2)\alpha + \\&\quad (2n + 1) \cosh \alpha \cosh(n + 1/2)\alpha, \\h_1^{(\alpha,n)} &= (n + 1) \cosh(n + 3/2)\alpha, \\u_n^{(n,\alpha)} &= 2\sqrt{2}q\varsigma e^{-(n+1/2)\alpha}, \\u_n^{(n,\beta)} &= 2\sqrt{2}q\varsigma e^{-(n+1/2)\beta}.\end{aligned}$$

$g_{-1}^{(\beta,n)}$, $g_0^{(\beta,n)}$, $g_1^{(\beta,n)}$, $h_{-1}^{(\beta,n)}$, $h_0^{(\beta,n)}$ and $h_1^{(\beta,n)}$ are obtained by replacing α with $-\beta$ and ς with $-\varsigma$.” [75]

Appendix D

Velocity and stream function

“Eq. (7.17) is equivalent to

$$u_\varrho = U^{(\alpha)} \mathbf{i}_\varrho \cdot \nabla z = U^{(\alpha)} \frac{1 - \cosh \alpha \cos \varphi}{\cosh \alpha - \cos \varphi}. \quad (\text{D.1})$$

Thus with aid of Eq. (7.8), Eq. (D.1) becomes

$$\frac{\partial \psi^{(0)}}{\partial \varphi} = U^{(\alpha)} q^2 \left[\frac{\cosh \alpha \sin \varphi}{(\cosh \alpha - \cos \varphi)^2} - \frac{\sinh^2 \alpha \sin \varphi}{(\cosh \alpha - \cos \varphi)^3} \right]. \quad (\text{D.2})$$

After integration, Eq. (D.2) gives

$$\psi^{(0)} = -U^{(\alpha)} q^2 \left[-\frac{\cosh \alpha}{(\cosh \alpha - \cos \varphi)} + \frac{\sinh^2 \alpha}{2(\cosh \alpha - \cos \varphi)^2} + C \right],$$

where C is an integration constant. By setting $C = 1/2$, we get Eq. (7.19). Eq. (7.20) can be obtained by the same approach.” [75]

Appendix E

Expansions

“The generating function of Gegenbauer polynomial is expressed as

$$\frac{1}{(1 - 2h\mu + h^2)^{1/2}} = \sum_{n=0}^{\infty} h^n C_n^{1/2}(\mu).$$

Setting $h = e^{-\alpha}$ and paying attention to the properties of Gegenbauer polynomial

$$C_{n-1}^{1/2}(x) = -\frac{dC_n^{-1/2}(x)}{dx},$$

$$(1 - x^2)y'' - (2\alpha + 1)xy' + n(n + 2\alpha)y = 0,$$

we get

$$\frac{\sin^2 \varphi}{2(\cosh \alpha - \cos \varphi)^{1/2}} = \frac{\sqrt{2}}{2} \sum_{n=1}^{\infty} n(n+1) \left(\frac{e^{-(n-1/2)\alpha}}{2n-1} - \frac{e^{-(n+3/2)\alpha}}{2n+3} \right) C_{n+1}^{-1/2}(\cos \varphi).$$

Differentiating with respect to μ , the generating function of Gegenbauer polynomial yields

$$\frac{(1 - \mu^2)}{(1 - 2h\mu + h^2)^{3/2}} = \sum_{n=0}^{\infty} h^n (n+1)(n+2) C_{n+2}^{-1/2}(\mu). \quad (\text{E.1})$$

Setting $h = e^{-|\varrho|}$ and multiplication with $\cosh \varrho$ gives

$$\frac{\cosh \varrho \sin^2 \varphi}{4(\cosh \varrho - \cos \varphi)^{3/2}} = \frac{\sqrt{2}}{4} \sum_{n=1}^{\infty} n(n+1) \left(e^{-(n-1/2)|\varrho|} + e^{-(n+3/2)|\varrho|} \right) C_{n+1}^{-1/2}(\cos \varphi).$$

and Eq. (E.1) becomes

$$\frac{1 - \mu^2}{(\cosh \varrho - \mu)^{3/2}} = 2\sqrt{2} \sum_{n=0}^{\infty} e^{-(n+3/2)|\varrho|} (n+1)(n+2) C_{n+2}^{-1/2}(\mu).$$

Differentiating with respect to ϱ yields

$$\frac{3(1-\mu^2)\sinh\varrho}{2(\cosh\varrho-\mu)^{5/2}} = 2\sqrt{2}\sum_{n=0}^{\infty}\left(n+\frac{3}{2}\right)e^{-(n+3/2)|\varrho|}(n+1)(n+2)C_{n+2}^{-1/2}(\mu). \quad (\text{E.2})$$

Setting $\varrho = \alpha$ and multiplication with $\sinh\alpha$, Eq. (E.2) becomes

$$\begin{aligned} \frac{3(1-\mu^2)\sinh^2\alpha}{8(\cosh\alpha-\mu)^{5/2}} &= \frac{1}{2}\sqrt{2}\sum_{n=0}^{\infty}\left(n+\frac{3}{2}\right)\sinh\alpha e^{-(n+3/2)\alpha}(n+1)(n+2)C_{n+2}^{-1/2}(\mu) \\ &= \frac{1}{2}\sqrt{2}\sum_{n=1}^{\infty}\left(n+\frac{1}{2}\right)\sinh\alpha e^{-(n+1/2)\alpha}n(n+1)C_{n+1}^{-1/2}(\mu) \\ &= \frac{1}{8}\sqrt{2}\sum_{n=1}^{\infty}(2n+1)\left(e^{-(n-1/2)\alpha}-e^{-(n+3/2)\alpha}\right)n(n+1)C_{n+1}^{-1/2}(\mu). \end{aligned}$$

”[75]

Appendix F

Matrices

“

$$\Xi_n = \begin{pmatrix} 0 & 0 & 0 & 0 & e_\alpha^- & e_\alpha^+ & 0 & 0 \\ 0 & 0 & 0 & 0 & 0 & 0 & e_\beta^- & e_\beta^+ \\ c_\alpha^- & s_\alpha^- & c_\alpha^+ & s_\alpha^+ & 0 & 0 & 0 & 0 \\ c_\beta^- & -s_\beta^- & c_\beta^+ & -s_\beta^+ & 0 & 0 & 0 & 0 \\ n_- s_\alpha^- & n_- c_\alpha^- & n_+ s_\alpha^+ & n_+ c_\alpha^+ & n_- e_\alpha^- & n_+ e_\alpha^+ & 0 & 0 \\ -n_- s_\beta^- & n_- c_\beta^- & -n_+ s_\beta^+ & n_+ c_\beta^+ & 0 & 0 & -n_- e_\beta^- & -n_+ e_\beta^+ \\ n_-^2 c_\alpha^- & n_-^2 s_\alpha^- & n_+^2 c_\alpha^+ & n_+^2 s_\alpha^+ & -n_-^2 e_\alpha^- & -n_+^2 e_\alpha^+ & 0 & 0 \\ n_-^2 c_\beta^- & -n_-^2 s_\beta^- & n_+^2 c_\beta^+ & -n_+^2 s_\beta^+ & 0 & 0 & -n_-^2 e_\beta^- & -n_+^2 e_\beta^+ \end{pmatrix}$$

with $n_- = n - \frac{1}{2}$, $n_+ = n + \frac{3}{2}$, $c_\alpha^\pm = \cosh n_\pm \alpha$, $s_\alpha^\pm = \sinh n_\pm \alpha$, $e_\alpha^\pm = e^{-n_\pm \alpha}$.

$$\mathbf{t}_n^{(\alpha)} = (0, 0, 0, 0, 0, 0, \tau_n^{(\alpha)}, 0)^T,$$

$$\mathbf{t}_n^{(\beta)} = (0, 0, 0, 0, 0, 0, -\tau_n^{(\beta)}, 0)^T,$$

$$\mathbf{v}_n^{(\alpha)} = (w^{(\alpha)}, 0, w^{(\alpha)}, 0, 0, 0, (1 - \eta)v^{(\alpha)}, 0)^T,$$

$$\mathbf{v}_n^{(\beta)} = (0, w^{(\beta)}, 0, w^{(\beta)}, 0, 0, 0, (1 - \eta)v^{(\beta)})^T,$$

where

$$\begin{aligned} \tau_n^{(\alpha)} &= \sqrt{2}bn(n+1) \left[\frac{e^{-(n-1/2)\alpha}}{2n-1} - \frac{e^{-(n+3/2)\alpha}}{2n+3} \right] \\ &\quad + \sqrt{2}a \left[\frac{n(n-1)e^{-(n-3/2)\alpha}}{(2n-1)(2n-3)} - \frac{(n+1)(n+2)e^{-(n+5/2)\alpha}}{(2n+3)(2n+5)} \right], \\ w^{(\alpha)} &= \frac{1}{\sqrt{2}}n(n+1) \left[\frac{e^{-(n-1/2)\alpha}}{2n-1} - \frac{e^{-(n+3/2)\alpha}}{2n+3} \right], \\ v^{(\alpha)} &= \frac{1}{4\sqrt{2}}n(n+1) \left[(2n-1)e^{-(n-1/2)\alpha} - (2n+3)e^{-(n+3/2)\alpha} \right]. \end{aligned}$$

$\tau_n^{(\beta)}$, $w_n^{(\beta)}$ and $v_n^{(\beta)}$ and is obtained by replacing α with β .” [75]

Appendix G

Recursion

“With the aid of Eq. (7.35), the second term in Eq. (7.29) can be simplified to

$$\begin{aligned}
 q^2 \frac{\sin^2 \varphi}{(\cosh \alpha - \cos \varphi)^{1/2}} \frac{\partial c}{\partial \cos \varphi} &= (a\mu + b)q^2 \sqrt{2} \sum_{n=1}^{\infty} n(n+1) \left(\frac{e^{-(n-1/2)\alpha}}{2n-1} - \frac{e^{-(n+3/2)\alpha}}{2n+3} \right) C_{n+1}^{-1/2}(\cos \varphi) \\
 &= bq^2 \sqrt{2} \sum_{n=1}^{\infty} n(n+1) \left(\frac{e^{-(n-1/2)\alpha}}{2n-1} - \frac{e^{-(n+3/2)\alpha}}{2n+3} \right) C_{n+1}^{-1/2}(\cos \varphi) \\
 &\quad + aq^2 \sqrt{2} \sum_{n=1}^{\infty} n(n+1) \left(\frac{e^{-(n-1/2)\alpha}}{2n-1} - \frac{e^{-(n+3/2)\alpha}}{2n+3} \right) \cos \varphi C_{n+1}^{-1/2}(\cos \varphi).
 \end{aligned} \tag{G.1}$$

Using the recursion relation

$$2(n+1/2) \cos \varphi C_{n+1}^{-1/2}(\cos \varphi) = (n+2)C_{n+2}^{-1/2}(\cos \varphi) + (n-1)C_n^{-1/2}(\cos \varphi),$$

the last term at the right hand side of Eq. (G.1) becomes

$$\begin{aligned}
 &aq^2 \sqrt{2} \sum_{n=1}^{\infty} n(n+1) \left(\frac{e^{-(n-1/2)\alpha}}{2n-1} - \frac{e^{-(n+3/2)\alpha}}{2n+3} \right) \cos \varphi C_{n+1}^{-1/2}(\cos \varphi) \\
 &= aq^2 \sqrt{2} \sum_{n=1}^{\infty} \frac{n(n+1)}{2n+1} \frac{e^{-(n-1/2)\alpha}}{2n-1} C_{n+2}^{-1/2}(\cos \varphi) \\
 &\quad - aq^2 \sqrt{2} \sum_{n=1}^{\infty} \frac{n(n+1)}{2n+1} \frac{e^{-(n+3/2)\alpha}}{2n+3} C_n^{-1/2}(\cos \varphi) \\
 &= aq^2 \sqrt{2} \sum_{n=2}^{\infty} \frac{n(n-1)}{2n-1} \frac{e^{-(n-3/2)\alpha}}{2n-3} C_{n+1}^{-1/2}(\cos \varphi) \\
 &\quad - aq^2 \sqrt{2} \sum_{n=0}^{\infty} \frac{(n+1)(n+2)}{2n+3} \frac{e^{-(n+5/2)\alpha}}{2n+5} C_{n+1}^{-1/2}(\cos \varphi).
 \end{aligned}$$

”[75]

Appendix H

List of Symbols

Symbol	Description	Units
a	Perturbation amplitude	m
c	Mole concentration	[-]
d	Separation distance	m
d_0	Capillary length	m
f	Bulk free energy density	J/m ³
g	Free energy density	J/m ³
g_0	Free energy density	J/m ³
k	Wavenumber	m ⁻¹
p	Pressure	Pa
t	Time	s
v_m	Molar volume	m ³ /mol
A	Amplitude with time	m
C	Capillary number	[-]
D	Bulk mass diffusivity	m ² /s
D_s	Surface mass diffusivity	m ² /s
E_p	Surface energy	J
E_0	Surface energy	J
\mathcal{F}	Free energy functional	J
G	Gibbs free energy	J
M	Dimensionless number	[-]
R_0	Radius of cylinder	m
R_1	Principal radius of curvature	m ⁻¹
R_2	Principal radius of curvature	m ⁻¹
R_u	Average radius of cylinder	m
R_g	Universal gas constant	JK ⁻¹ mol ⁻¹
S	Surface area	m ²

Symbol	Description	Units
T	Temperature	K
U	Velocity	m/s
V	Volume	m ³
Re	Reynolds number	[-]
\mathbf{J}	Flux	m/s
\mathbf{J}_s	Surface Flux	m/s
\mathbf{n}	Normal vector	[-]
\mathbf{t}	Tangential vector	[-]
\mathbf{u}	Velocity	m/s
\mathcal{L}	Lagrange energy density	J/m ³
α	Ratio of amplitude to radius	[-]
β	Ratio of amplitude to wavelength	[-]
γ	Surface energy parameter	J/m ²
ϵ	Interfacial width parameter	m
ε	Length ratio	[-]
η	Dynamic viscosity	kg s ⁻¹ m ⁻¹
θ	Contact angle	°
κ	Mean curvature	m ⁻¹
$\kappa_c, \kappa_1, \kappa_2$	Gradient energy coefficients	J/m ²
λ	Wavelength	m
λ^{crit}	Critical wavelength	m
μ	Chemical potential	J/m ³
ρ	Density	kg/m ³
σ	Surface tension	J/m ²
τ	Relaxation coefficient	J/m ⁴
ϕ	Order parameter	[-]
ω	Growth rate	s ⁻¹
Ω_i	Interaction coefficient	J/m ³
Ω	Atomic volume	m ³
Λ	Mobility	m ⁵ /(Js)

Appendix I

List of Abbreviations

AC	Allen-Cahn
CF	Capillary-Flow
CHNS	Cahn-Hilliard-Navier-Stokes
LSW	Lifshitz-Slyozov-Wagner
PR	Plateau-Rayleigh
SOR	Successive Over Relation

Bibliography

- [1] L. Rayleigh, On the instability of jets, *Proc. R. Soc. Lond.* **10**, 4–13 (1878).
- [2] L. Rayleigh, On the capillary phenomena of jets, *Proc. R. Soc. A* **29**, 71–97 (1879).
- [3] F.A. Nichols and W.W. Mullins, Surface- and volume-diffusion contributions to morphological changes driven by capillarity, *Trans. AIME* **233**, 1840–1848 (1965).
- [4] W.C. Carter and A.M. Glaeser, The effect of finite amplitude perturbations on the stability of continuous phases, *Mater. Sci. Eng.* **89**, L41–L45 (1987).
- [5] A.H. Nayfeh, Nonlinear stability of a liquid jet, *Phys. Fluids* **13**, 841 (1970).
- [6] D.L. Hu and J.W.M. Bush, Meniscus-climbing insects, *Nature* **437**, 733–736 (2005).
- [7] J. Plateau, *Statique Expérimentale et Théorique des Liquides soumis aux seules Forces Moléculaires* (Paris, 1873).
- [8] R. Bar-Ziv and E. Moses, Instability and “pearling” states produced in tubular membranes by competition of curvature and tension, *Phys. Rev. Lett.* **73**, 1392 (1994).
- [9] H. Gau, S. Herminghaus, P. Lenz, and R. Lipowsky, Liquid morphologies on structured surfaces: from microchannels to microchips, *Science* **283**, 46 (1999).
- [10] D.R. Link, S.L. Anna, D.A. Weitz, and H.A. Stone, Geometrically mediated breakup of drops in microfluidic devices, *Phys. Rev. Lett.* **92**, 054503 (2004).
- [11] V. Cardoso and O.J.C. Dias, Rayleigh-Plateau and Gregory-Laflamme instabilities of black strings, *Phys. Rev. Lett.* **96**, 181601 (2006).
- [12] F. Blanchette and T.P. Bigioni, Partial coalescence of drops at liquid interfaces, *Nat. Phys.* **2**, 254 (2006)
- [13] O. Bäümchen, L. Marquant, R. Blossey, A. Münch, B. Wagner, and K. Jacobs, Influence of slip on the Rayleigh-Plateau rim instability in dewetting viscous films, *Phys. Rev. Lett.* **113**, 014501 (2014).

- [14] T. Azuma, T. Morita, and S. Takeuchi, Hagedorn instability in dimensionally reduced large-N gauge theories as Gregory-Laflamme and Rayleigh-Plateau instabilities, *Phys. Rev. Lett.* **113**, 091603 (2014).
- [15] G. Prado, Y. Amarouchene, and H. Kellay, Experimental evidence of a Rayleigh-Plateau instability in free falling granular jets, *Phys. Rev. Lett.* **106**, 198001 (2011).
- [16] A. Tuniz, K.J. Kaltenecker, B.M. Fischer, M. Walther, S.C. Fleming, A. Argyros, and B.T. Kuhlmeier, Metamaterial fibres for subdiffraction imaging and focusing at terahertz frequencies over optically long distances, *Nat. Commun.* **4**, 2706 (2013).
- [17] A. Passian and T. Thundat, Materials science: The abilities of instabilities, *Nature* **487**, 440 (2012)
- [18] S. Haefner, M. Benzaquen, O. Bäümchen, T. Salez, R. Peters, J.D. McGraw, K. Jacobs, E. Raphaël, and K. Dalnoki-Veress, Influence of slip on the Plateau-Rayleigh instability on a fibre, *Nat. Commun.* **6**, 7409 (2015).
- [19] S. Mora, T. Phou, J.M. Fromental, L.M. Pismen, and Y. Pomeau, Capillarity driven instability of a soft solid, *Phys. Rev. Lett.* **105**, 214301 (2010).
- [20] A. Javadi, J. Eggers, D. Bonn, M. Habibi, and N.M. Ribe, Delayed capillary breakup of falling viscous jets, *Phys. Rev. Lett.* **110**, 144501 (2013).
- [21] M. Athanassenas, Volume-preserving mean curvature flow of rotationally symmetric surfaces, *Comment. Math. Helv.* **72**, 52 (1997).
- [22] Q. Ma, S. Harada, and B. Liu, On the critical instability wavelengths of rod morphologies containing an arbitrary sinusoidal perturbation, *Mater. Sci. Eng. A* **221**, 192 (1996).
- [23] Z. Suo, Lecture notes: Evolving Small Structures, Harvard University, 2004.
- [24] A.P.S. Wheeler, Physics on tap, *Phys. Educ.* **47**, 403–408 (2012).
- [25] https://en.wikipedia.org/wiki/Plateau-Rayleigh_instability.
- [26] J.J. Kaufman, G. Tao, S. Shabahang, E.H. Banaei, D.S. Deng, X. Liang, S.G. Johnson, Y. Fink, and A.F. Abouraddy, Structured spheres generated by an in-fibre fluid instability, *Nature* **487**, 463–467 (2012).
- [27] Y.C. Huang, P.W. Fan, C.W. Lee, C.W. Chu, C.C. Tsai, and J.T. Chen, Transformation of polymer nanofibers to nanospheres driven by the Rayleigh instability, *ACS Appl. Mater. Interfaces* **5**, 3134–3142 (2013).

- [28] S. Mei, X. Feng, and Z. Jin, Fabrication of polymer nanospheres based on Rayleigh instability in capillary channels, *Macromolecules* **44**, 1615–1620 (2011).
- [29] S. Shabahang, J.J. Kaufman, D.S. Deng, and A.F. Abouraddy, Observation of the Plateau-Rayleigh capillary instability in multi-material optical fibers, *Appl. Phys. Lett.* **99**, 161909 (2011).
- [30] B.J. Haupt, T.J. Senden, and E.M. Sevick, AFM evidence of Rayleigh instability in single polymer chains, *Langmuir* **18**, 2174–2182 (2002).
- [31] S. Karim, M.E. Toimil-Molares, A.G. Balogh, W. Ensinger, T.W. Cornelius, E.U. Khan, and R. Neumann, Morphological evolution of Au nanowires controlled by Rayleigh instability, *Nanotechnology* **17**, 5954 (2006).
- [32] Y. Qin, S.M. Lee, A. Pan, U. Gösele, and M. Knez, Rayleigh-instability-induced metal nanoparticle chains encapsulated in nanotubes produced by atomic layer deposition, *Nano Lett.* **8**, 114–118 (2008).
- [33] M. Rauber, F. Muench, M.E. Toimil-Molares, and W. Ensinger, Thermal stability of electrodeposited platinum nanowires and morphological transformations at elevated temperatures, *Nanotechnology* **23**, 475710 (2012).
- [34] R.B. Edwards, Joint tolerances in capillary copper piping joints, *Weld. J. Res. Suppl.* **6**, 321 (1972).
- [35] Y. Men, X. Zhang, and W. Wang, Capillary liquid bridges in atomic force microscopy: Formation, rupture, and hysteresis, *J. Phys.: Condens. Matter.* **131**, 184702 (2009).
- [36] B.N.J. Persson, Wet adhesion with application to tree frog adhesive toe pads and tires, *J. Chem. Phys.* **19**, 376110 (2007).
- [37] P.V. Petkov and B.P. Radoev, Statics and dynamics of capillary bridges, *Colloids Surf., A* **460**, 18 (2014).
- [38] P.L. Schaffer, R.H. Mathiesen, L. Arnberg, M. Di Sabatino, and A. Snigirev, In situ investigation of spinodal decomposition in hypermonotectic Al–Bi and Al–Bi–Zn alloys, *New J. Phys.* **10**, 053001 (2008).
- [39] E.D. Siggia, Late stages of spinodal decomposition in binary mixtures, *Phys. Rev. A* **20**, 595 (1979).
- [40] R. Shimizu and H. Tanaka, A novel coarsening mechanism of droplets in immiscible fluid mixtures, *Nat. Commun.* **6**, 7407 (2015).

- [41] M. Stimson and G.B. Jeffery, The motion of two spheres in a viscous fluid, *Proc. R. Soc. A* **111**, 110–116 (1926).
- [42] G.B. Jeffery, On a form of the solution of Laplace’s equation suitable for problems relating to two spheres, *Proc. R. Soc. A* **87**, 109–120 (1912).
- [43] A.A. Golovin, A. Nir, and L.M. Pismen, Spontaneous motion of two droplets caused by mass transfer, *Ind. Eng. Chem. Res.* **34**, 3278–3288 (1995).
- [44] S. Haber, G. Hetsroni, and A. Solan, On the low Reynolds number motion of two droplets, *Int. J. Multiph. Flow* **1**, 57–71 (1973).
- [45] M. Meyyappan, W. R. Wilcox, and R.S. Subramanian, The slow axisymmetric motion of two bubbles in a thermal gradient, *J. Colloid Interface Sci.* **94**, 243–257 (1983).
- [46] H.J. Keh and S.H. Chen, The axisymmetric thermocapillary motion of two fluid droplets, *Int. J. Multiphase Flow* **16**, 515–527 (1990).
- [47] P.C. Hohenberg and B.I. Halperin, Theory of dynamic critical phenomena, *Rev. Mod. Phys.* **49**, 435 (1977).
- [48] F. Wang, A. Choudhury, M. Selzer, R. Mukherjee, and B. Nestler, Effect of solutal Marangoni convection on motion, coarsening, and coalescence of droplets in a monotectic system, *Phys. Rev. E* **86**, 066318 (2012).
- [49] A.A. Wheeler, Cahn–Hoffman ξ -Vector and its relation to diffuse interface models of phase transitions, *J. Stat. Phys.* **95**, 1245 (1999).
- [50] E. Noether and M.A. Tavel, Invariant variational problems, arXiv:physics/0503066v1, 2005.
- [51] B. Nestler, H. Garcke, and B. Stinner, Multicomponent alloy solidification: Phase-field modeling and simulations, *Phys. Rev. E* **71**, 041609 (2005).
- [52] J.W.M. Bush, Surface tension module, Cambridge, 2004.
- [53] H. Liu, A.J. Valocchi, Y. Zhang, and Q. Kang, Phase-field-based lattice Boltzmann finite-difference model for simulating thermocapillary flows, *Phys. Rev. E* **87**, 013010 (2013).
- [54] J.S. Langer, Instabilities and pattern formation in crystal growth, *Rev. Mod. Phys.* **52**, 1-28 (1980).
- [55] B. Derby and J.J. Favier, A criterion for the determination of monotectic structure, *Acta Metall.* **31**, 1123–1130 (1983).

- [56] M. Selzer, Parallele Algorithmen zur numerischen Loesung von Phasenfeldmodellen mit Stroemung, Master thesis-Hochschule Karlsruhe, 2007.
- [57] P. Moin, *Fundamentals of engineering numerical analysis* (Cambridge University Press, 2010).
- [58] M. Griebel, T. Dornseifer, and T. Neunhoeffler, *Numerical simulation in fluid dynamics: A practical introduction* (Siam, 1997).
- [59] B. Nestler, F. Wendler, M. Selzer, B. Stinner, and H. Garcke, Phase-field model for multiphase systems with preserved volume fractions, *Phys. Rev. E* **78**, 011604 (2008).
- [60] F. Wang, R. Mukherjee, M. Selzer, and B. Nestler, Numerical study on solutal Marangoni instability in finite systems with a miscibility gap, *Phys. Fluids* **26**, 124102 (2014).
- [61] W.C. Carter, J.E. Taylor, and J.W. Cahn, Variational methods for microstructural-evolution theories, *JOM* **49**, 30 (1997).
- [62] F. Wang, and B. Nestler, Detachment of nanowires driven by capillarity, *Scr. Mater.* **113**, 167 (2016).
- [63] , M.C. Yuen, Non-linear capillary instability of a liquid jet, *J. Fluid Mech.* **33**, 151 (1968).
- [64] W.W. Mullins, Theory of thermal grooving, *J. Appl. Phys.* **28**, 333 (1957).
- [65] R.W. Balluffi, S. Allen, and W.C. Carter, *Kinetics of Materials* (John Wiley & Sons, 2005).
- [66] J.W. Cahn, C.M. Elliott, and A. Novick-Cohen, The Cahn–Hilliard equation with a concentration dependent mobility: motion by minus the Laplacian of the mean curvature, *Eur. J. Appl. Math.* **7**, 287 (1996).
- [67] R. Oloff, *Geometrie der Raumzeit* (Vieweg Verlag, 1999).
- [68] F. Wang, M. Ben Said, M. Selzer, and B. Nestler, Underdamped capillary wave caused by solutal Marangoni convection in immiscible liquids, *J. Mater. Sci.* **51**, 1820 (2016).
- [69] J.S. Langer, Instabilities and pattern formation in crystal growth, *Rev. Mod. Phys.* **52**, 1 (1980).
- [70] M.I. Mendeleev and Y. Mishin, Molecular dynamics study of self-diffusion in bcc Fe, *Phys. Rev. B* **80**, 144111 (2008).

- [71] M.J. Assael, A.E. Kalyva, K. D. Antoniadis, R. M. Banish, I. Egry, J. Wu, E. Kaschnitz, and W. A. Wakeham, Reference data for the density and viscosity of liquid copper and liquid tin, *J. Phys. Chem. Ref. Data* **39**, 033105 (2010).
- [72] H. Linde, M.G. Velarde, W. Waldhelm, and A. Wierschem, Interfacial wave motions due to marangoni instability: III. Solitary waves and (periodic) wave trains and their collisions and reflections leading to dynamic network (cellular) patterns in large containers, *J. Colloid. Interface Sci.* **236**, 214 (2001).
- [73] J. Reichenbach and H. Linde, Linear perturbation analysis of surface-tension-driven convection at a plane interface (Marangoni instability), *J. Colloid. Interface Sci.* **84**, 433 (1981).
- [74] C.V. Sternling and L.E. Scriven, Interfacial turbulence: hydrodynamic instability and the Marangoni effect, *AIChE J.* **5**, 514 (1959).
- [75] F. Wang, M. Selzer, and B. Nestler, On the motion of droplets driven by solutal Marangoni convection in alloy systems with a miscibility gap, *Physica D* **307**, 82 (2015).
- [76] H.A. Stone, Dynamics of drop deformation and breakup in viscous fluids, *Ann. Rev. Fluid Mech.* **26**, 65–102 (1994).
- [77] J. Happel and H. Brenner, *Low Reynolds number hydrodynamics: with special applications to particulate media* (Springer, 2012).
- [78] L.M. Witkowski and J.S. Walker, Solutocapillary instabilities in liquid bridges, *Phys. Fluids* **14**, 2647–2656 (2002).
- [79] A.E. Rednikov and Yu.S. Ryazantsev, Effect of internal heat release on the capillary force acting on a droplet and on the interaction of droplets with each other and with a wall, *Fluid Dyn.* **25**, 753–760 (1990).
- [80] J.J. Hoyt, M. Asta, and B. Sadigh, Test of the universal scaling law for the diffusion coefficient in liquid metals, *Phys. Rev. Lett.* **85**, 594 (2000).
- [81] J.S. Langer, Statistical methods in the theory of spinodal decomposition, *Acta Metall.* **21**, 1649–1659 (1973).
- [82] I.M. Lifshitz and V.V. Slyozov, The kinetics of precipitation from supersaturated solid solutions, *J. Phys. Chem. Solids* **19**, 35–50 (1961).
- [83] H.J. Diepers, C. Beckermann, and I. Steinbach, Simulation of convection and ripening in a binary alloy mush using the phase-field method, *Acta Mater.* **47**, 3663–3678 (1999).

- [84] C. Wagner, Theorie der alterung von niederschlägen durch umlösen (Ostwald-reifung), *Z. Elektrochem.* **65**, 581–591 (1961).
- [85] G. Tegze, T. Pusztai, and L. Gránásy, Phase field simulation of liquid phase separation with fluid flow, *Mater. Sci. Eng. A* **413**, 418–422 (2005).
- [86] S.P. Marsh and M.E. Glicksman, Kinetics of phase coarsening in dense systems, *Acta Mater.* **44**, 3761–3771 (1996).
- [87] W. Bender and L. Ratke, Ostwald ripening of liquid phase sintered Cu–Co dispersions at high volume fractions, *Acta Mater.* **46**, 1125–1133 (1998).
- [88] D.J. Rowenhorst, J.P. Kuang, K. Thornton, and P.W. Voorhees, Three-dimensional analysis of particle coarsening in high volume fraction solid–liquid mixtures, *Acta Mater.* **54**, 2027–2039 (2006).
- [89] L. Ratke and W.K. Thieringer, The influence of particle motion on Ostwald ripening in liquids, *Acta Metall.* **33**, 1793–1802 (1985).
- [90] M. Schwarz, A. Karma, K. Eckler, and D.M. Herlach, Physical mechanism of grain refinement in solidification of undercooled melts, *Phys. Rev. Lett.* **73**, 1380 (1994).
- [91] W.J. Boettinger, S.R. Coriell, A.L. Greer, A. Karma, W. Kurz, M. Rappaz, and R. Trivedi, Solidification microstructures: recent developments, future directions, *Acta Mater.* **48**, 43 (2000).
- [92] L. Ratke and A. Müller, On the destabilisation of fibrous growth in monotectic alloys, *Scripta Mater.* **54**, 1217 (2006).
- [93] W. Zhai, B. Wang, L. Hu, and B. Wei, Liquid phase separation of ternary Al–In–Sn/Ge monotectic type alloys investigated with calorimetric method, *Philos. Mag. Lett.* **95**, 187 (2015).
- [94] D.F. Urban and H. Grabert, Interplay of Rayleigh and Peierls instabilities in metallic nanowires, *Phys. Rev. Lett.* **91**, 256803 (2003).
- [95] M.P. Cecchini, V.A. Turek, J. Paget, A.A. Kornyshev, and J.B. Edel, Self-assembled nanoparticle arrays for multiphase trace analyte detection, *Nat. Mater.* **12**, 165 (2013).
- [96] E.C. Garnett, W. Cai, J.J. Cha, F. Mahmood, S.T. Connor, M.G. Christoforo, Y. Cui, M.D. McGehee, and M.L. Brongersma, Self-limited plasmonic welding of silver nanowire junctions, *Nat. Mater.* **11**, 241 (2012).

- [97] H. Suzuki, T. Kaneko, Y. Shibuta, M. Ohno, Y. Maekawa, and T. Kato, Wafer-scale fabrication and growth dynamics of suspended graphene nanoribbon arrays, *Nat. Commun.* **7**, 7409 (2016).
- [98] A. Parmigiani, S. Faroughi, C. Huber, O. Bachmann, and Y. Su, Bubble accumulation and its role in the evolution of magma reservoirs in the upper crust, *Nature* **532**, 492 (2016).
- [99] D. Lohse and D. van der Meer, Granular media: Structures in sand streams, *Nature* **459**, 1064 (2009).
- [100] J.R. Royer, D.J. Evans, L. Oyarte, Q. Guo, E. Kapit, M.E. Möbius, S.R. Waitukaitis, and M.H. Jaeger, High-speed tracking of rupture and clustering in freely falling granular streams, *Nature* **459**, 1110 (2009).
- [101] J.C. Bird, R. De Ruiter, L. Courbin, and H.A. Stone, Daughter bubble cascades produced by folding of ruptured thin films, *Nature* **465**, 759 (2010).
- [102] A.A. Castrejón-Pita, J.R. Castrejon-Pita, and I.M. Hutchings, Breakup of liquid filaments, *Phys. Rev. Lett.* **108**, 074506 (2012).
- [103] J.C. Burton, R. Waldrep, and P. Taborek, Scaling and instabilities in bubble pinch-off, *Phys. Rev. Lett.* **94**, 184502 (2005).
- [104] P.J. Zimoch, G.H. McKinley, and A.E. Hosoi, Capillary breakup of discontinuously rate thickening suspensions, *Phys. Rev. Lett.* **111**, 036001 (2013).
- [105] A.S. Utada, A. Fernandez-Nieves, J.M. Gordillo, and D.A. Weitz, Absolute instability of a liquid jet in a coflowing stream, *Phys. Rev. Lett.* **100**, 014502 (2008).
- [106] J. Eggers and E. Villiermaux, Physics of liquid jets, *Rep. Prog. Phys.* **71**, 036601 (2008).
- [107] A. Kumar, Phase-field modeling of microstructural pattern formation in alloys and geological veins, KIT scientific publishing, 2016.
- [108] M. Ben Said, M. Selzer, B. Nestler, D. Braun, C. Greiner, and H. Garcke, A phase-field approach for wetting phenomena of multiphase droplets on solid surfaces, *Langmuir* **30**, 4033 (2014).
- [109] F. Wang and B. Nestler, A phase-field study on the formation of the intermetallic Al₂Au phase in the Al-Au system, *Acta Mater.* **95**, 65 (2015).